Coherent Synchrotron Radiation Diagnostics for Investigating the Longitudinal Microbunching Instability at Diamond Light Source

William Shields

Department of Physics
Royal Holloway, University of London

A thesis submitted to the University of London for the degree of Doctor of Philosophy

February 2016

Declaration

I confirm that the work presented in this thesis is my own. Where information has been derived from other sources, I confirm that this has been indicated in the document.

Signed:

Date:

For my parents, Sue and Geoff, and my sister, Joanna.

Abstract

A setup for measurements of Coherent Synchrotron Radiation (CSR) to investigate the longitudinal Microbunching Instability has been designed and installed in the storage ring of Diamond Light Source (DLS). Third generation light sources such as DLS are known to be susceptible to a phenomenon called the Microbunching Instability, where bursts of CSR are observed above a threshold bunch current, the wavelengths of which are of the order of the bunch length and smaller. Above threshold, these bursts appear quasi-periodic, however at high bunch currents the emissions appear chaotically. Diamond Light Source can operate with bunches as short as a few picoseconds, making bunch profile measurements particularly challenging. Ultra-fast room temperature Schottky Barrier Diodes were employed to measure the emitted CSR spectrum in a Michelson Interferometer. The measured CSR spectrum can then be used to reconstruct the longitudinal bunch profile. Studies were conducted to measure the CSR spectrum for an increasing bunch current to investigate how the emitted spectrum varies as the instability is triggered and evolves into the chaotic bursting regime.

Acknowledgements

Firstly, I would like to thank my supervisor, Dr Pavel Karataev, for his help and guidance over the past four years. Without him, this thesis and my PhD would not have been possible.

I would like to thank all my colleagues at Royal Holloway for their help and support. Thanks go to Dr Alexey Lyapin, Prof Stewart Boogert, Gary Boorman and Dr Laurie Nevay for all the useful discussions and advice they've given me during my time here.

Thanks go to Dr. Francis Cullinan, Dr. Robert Ainsworth, Dr Nirav Joshi, Dr Konstantin Lekomtsev, Dr. Tom Aumeyr, Dr Jochem Snuverink, and Gabriela Druitt, not only for their support and making the office a pleasant environment, but also for making my time more enjoyable with many lunches, coffees, and beers.

I would also like to thank Royal Holloway and Diamond Light Source for providing the funding necessary for me to complete this research, and for providing the facilities which have enabled me to do so.

I would like to thank my supervisor at Diamond Light Source, Dr Guenther Rehm, without whom the work in this thesis would not have been possible. His help, insight and guidance have been invaluable. Thanks must also go to Professor Riccardo Bartolini, Dr. Ian Martin, Dr. Alun Morgan, Graham Cook, Lorraine Bobb, and Aiveen Finn for all their help at Diamond.

Finally, the biggest thanks go to my sister and my parents for their endless support. They have always been there for me, not only throughout my PhD, but since the day I was born. To them, I am eternally grateful.

Contents

List of Figures

List of Tables

Chapter 1

Introduction

1.1 High Energy Physics

One of the most successful theories of the 20th century is the Standard Model of particle physics, which describes all electromagnetic, weak, and strong nuclear force interactions, and details every subatomic particle known to exist in our universe. To have achieved such a knowledge of the elementary constituents of the Standard Model, scientists have continuously needed to probe particle interactions at increasingly higher energies, an achievement which has thus far been made possible through the of use of particle accelerators. Invented in the 1930's [1, 2], the first basic particle accelerators achieved modest energies of around 1 MeV through electrostatic acceleration. Their creation demonstrated the potential of particle accelerators, opening the door to a new field of research which has continued to grow to the present day.

At the forefront of modern particle and accelerator physics is the Large Hadron Collider (LHC), a 27 km long circular accelerator designed to collide protons at an energy of 14 TeV. The LHC, described as the largest scientific experiment ever conducted, has already made several discoveries including the renowned Higgs Boson [3,4], a particle which generated a global interest and the discovery of which gained worldwide fame. Despite the LHC and particle accelerators of the past continuing to reaffirm the success of the Standard Model, some of the most fundamental questions in particle physics remain unanswered, such as an explanation of dark matter, the cause of matter/anti-matter asymmetry, an explanation of quantum gravity, etc. The ongoing quest, not only to answer these questions but to improve the accuracy of existing measurements, is driving the development of the next generation of particle accelerators such as two proposed electron-positron colliders;

the International Linear Collider (ILC) [5], and the Compact Linear Collider (CLIC) [6], designed to achieve collision energies of up to 1 TeV and up to 3 TeV respectively.

The acceleration of beams to the TeV scale is only possible thus far through two established methods, a linear accelerator (linac) or a circular accelerator in the form of a synchrotron, of which the aforementioned LHC is an example. Whilst particle physics now provides motivation for research on the energy frontier, lower energy particle accelerators have also been developed as an incredibly useful tools for other areas of scientific research. An increasingly more prevalent application is particle therapy, in particular with hadrons, where particle accelerators are used to provide treatments for various oncological conditions. One of the most common applications for particle accelerators, however, is once again in the form of a synchrotron: light sources.

1.2 Synchrotron Light Sources

Early synchrotrons arose as part of the effort to achieve higher beam energy, as other types of accelerators suffered from practical limitations, particularly physical size. It was proposed in 1945 [7, 8] that a particle beam of increasing energy could be kept at a constant orbital radius by varying the magnetic field that steered the beam, whilst an radio-frequency (RF) resonator provided the acceleration. Sure enough, the principle of the synchrotron was proven the following year [9]. With higher energy beams achievable, the machines had to consequently become larger; the orbital radius, ρ, increases with beam energy, E, according to:

$$\rho = \frac{E}{ecB}, \tag{1.1}$$

where e is the electron charge and c is the speed of light. As synchrotrons varied the magnetic field, to keep ρ constant, the field must be synchronised with increasing beam energy. As higher and higher beam energies were being achieved, the limits of magnet technology at the time meant that the radius must be increased.

At this stage, research into both electron and proton synchrotrons was growing, and the first proton synchrotrons were soon developed [10, 11]. With electron synchrotrons, however, there was the additional discovery of synchrotron radiation, first observed as visible radiation in 1947 [9]. The radiation was only observed in electron synchrotrons due to the electron's light mass in comparison to the proton. To understand why, we need to

use the equation for the instantaneous power emitted by a relativistic charged particle as it undergoes a transverse acceleration:

$$P_\gamma = \frac{1}{6\pi\epsilon_0}\frac{e^2 c}{\rho^2}\cdot\gamma^4, \tag{1.2}$$

where γ is the Lorentz factor and ϵ_0 is the vacuum permittivity. The origin of this equation is discussed further in section 2.1. It is the dependence on γ^4 that results in the large difference of emitted power. For an electron and a proton of the same energy, given the ratio between the rest mass of the two particles, then the power radiated by the electron is 1.13×10^{13} greater than that from the proton. The emissions from protons only become significant at very high energies (around 10^2 GeV and above), hence for the purposes of synchrotron radiation experiments, electrons are significantly more efficient.

Investigations into the radiation emitted from electron synchrotrons revealed that they were also very intense sources of x-rays [12]. Further advances in accelerator physics saw creation of the first storage rings, which had the benefit of providing a very stable beam [13]. These machines formed the early basis of modern synchrotrons by incorporating focussing and corrective magnets, and consequently became known as first generation synchrotrons. For the first generation though, any synchrotron radiation experiments were still a parasitical investigation on machines whose primary purpose was predominantly high energy physics.

1.2.1 Second Generation Light Sources

As synchrotron radiation was becoming highly sought after as a tool for solid state physics research, user facilities dedicated entirely to the production of synchrotron radiation were developed, known as second generation light sources. Rather than just the photon flux being the defining parameter of these facilities, the use of monochromators in the beamlines consequently meant that brilliance was seen as more useful characteristic by users of the machine [12]. Brilliance is a measure of the quality of the photon beam, the formula for which is given in equation 1.3 [14, 15], where B_r is the brilliance, $\sigma_{x/y}$ are the transverse beam sizes, $\sigma'_{x/y}$ are the transverse divergences, and F is the photon flux.

$$B_r = \frac{F}{4\pi^2\sigma_x\sigma'_x\sigma_y\sigma'_y}\left(\frac{\text{photons}}{\text{s mm}^2\ \text{mrad}^2\ 0.1\%\ \text{BW}}\right) \tag{1.3}$$

The photon beam size and divergence is determined from a combination of the electron beam size and divergence, and the photon emission from a single electron [16]. The brilliance of a beam often cannot be improved by increasing flux alone, but it can be improved by decreasing the electron beam emittance. This measure of emittance is often used as the defining characteristic of light source's beam in the accelerator physics community. The desire to minimise the emittance is therefore an ever-present goal of synchrotron light sources.

1.2.2 Third Generation Light Sources

Despite the success of second generation light sources, the need arose for higher energy photons, particularly in the hard X-ray region. This, in addition to the push for lower emittance machines, led to the development of light sources which are optimised for brilliance, known as third generation light sources.

Research into the development of third generation light sources grew with the introduction of insertion devices (IDs) known as wigglers and undulators. These devices consist of a periodic array of dipoles, alternating in polarity in the vertical direction which introduces a horizontal oscillation to the trajectory of the electron beam through the device. The two types of ID differ primarily in field strength, magnet periodicity, and number of dipoles, with the wiggler having a higher peak magnetic field but fewer poles and shorter magnet period. This results in a differing angular deflection of the electron bunch, and consequently a different power spectrum being produced [17], an example of which is shown in figure 1.1 for the IDs in Diamond Light Source.

Typically, wigglers emit a similar spectrum to that of a conventional dipole [22], albeit ~ 2 orders of magnitude higher brilliance and extending to higher energy photons. Undulators, however, produce spatially coherent components in the spectrum from the constructive interference of the radiation leading to a quasi-monochromatic spectrum [14], as shown by the series of lines in figure 1.1. The peak brilliance is notably several orders of magnitude higher than that from a dipole, depending on undulator configuration.

To host insertion devices, accelerators must have long straight drift spaces, which were not readily available in second generation storage rings [15]. This was overcome using the same solution to decrease the beam emittance; the implementation of either a double-bend achromat (DBA) lattice or a triple-bend achromat (TBA) lattice. Both DBA and TBA lattices are designed to have zero dispersion at both ends of the dipole doublet

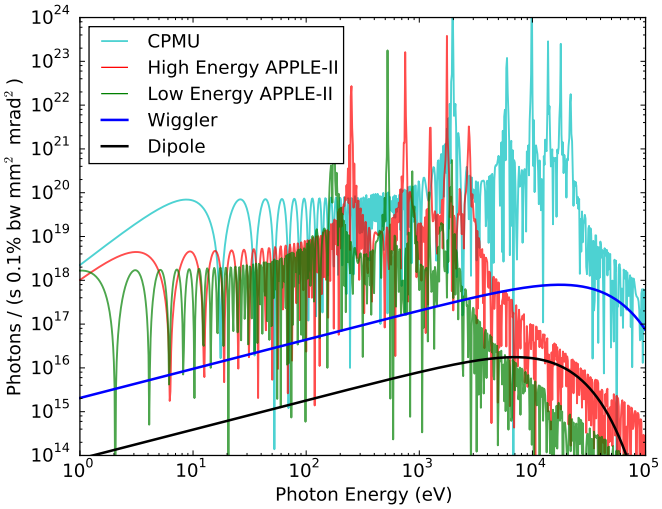

Figure 1.1: Power spectra produced from dipoles, wigglers and undulators at Diamond Light Source based upon magnet parameters in [18–21].

or triplet respectively which reduces the beam emittance [23]. The straight sections are located before and after the dipole regions, thus the IDs can be readily accommodated. The zero dispersion in the straight sections additionally minimises any effect the IDs may have on the beam emittance [24].

The majority of synchrotron light source storage rings employ DBA or TBA lattices, however future 3rd generation light sources such as MAX-IV [25] are designed to use multi-bend achromats which offer additional dipole and straight sections for insertion devices.

The optimisation of storage rings and inclusion of IDs have led to the creation of nearly 50 third generation light sources across the globe at the time of writing, either in operation, construction or commissioning stages [26]. They are an invaluable tool for scientists, with each light source offering unique facilities to users, in terms of beamlines and instrumentation, and their producible spectra ranging from infrared to hard x-rays.

1.2.3 State of the Art and Future Generations of Light Sources

Give the increased brilliance provided by insertion devices, development has begun on 4th generation light sources based upon the principle of long undulators. The electron bunch propagating through the long undulator will emit a photon beam which interacts with the electron bunch, the interaction causing an increase in coherent emissions, initiated either by laser seeding or though SASE (self-amplified spontaneous emission). The undulator must be sufficiently long to allow sufficient time for this process to occur, often over

hundreds of metres depending on the desired spectrum [27]. An obvious impracticality for a storage ring, these types of light sources use a linac to achieve the required beam energy, and are known as free electron lasers (FEL). With the first FEL successfully demonstrated at FLASH and subsequently opened to the user community in 2005 [28], at least 14 FELs either are operational such as the LCLS in 2009 [29], or under construction or at the planning/proposal stage [26] such as the United Kingdom based FEL Test Facility known as CLARA [30].

Despite the operation of FELs being in it infancy, development of the fifth generation of light sources has already commenced. The motivation for this is to combat the increasing size of FELs, not only the undulator length but additionally the linac length required to achieve the necessary beam energy [31]. Research is currently ongoing into both miniaturisation of current methods using microelectromechanical systems [32], and new acceleration techniques such as plasma-wakefield acceleration [33] and dielectric laser acceleration [34]. These methods aim to achieve a table-top sized accelerator not only to reduce costs, but provide increased accessibility to the user community.

1.3 Diamond Light Source

Whilst future generation light sources are being developed, substantial research is still ongoing in the 3rd generation of light sources in a bid to further optimise the machines. Once such example is Diamond Light Source, the United Kingdom's national synchrotron facility which opened in 2006. It is a 3 GeV synchrotron radiation source, located at the Harwell Science and Innovation Campus in Oxfordshire. The research presented in this thesis was performed at this facility. A more detailed description of Diamond will be given in section 4.1. A total of 18 beamlines are currently in operation at Diamond, providing a broad spectrum of synchrotron radiation used for multidisciplinary research including structural biology, energy, engineering, nanoscience and environmental sciences [18].

Diamond follows the same layout that many third generation synchrotrons use, as shown in figure 1.2. The electrons for the beam are provided by an electron gun, whereafter a linac then accelerates the electrons to 100 MeV. The bunches are then injected into a booster ring, and are then accelerated up to 3 GeV, where they are injected into the main storage ring. The storage ring typically holds 900 bunches at 3 GeV in a top-up mode, where the beam is kept at 300 mA by injecting every 10 minutes [35].

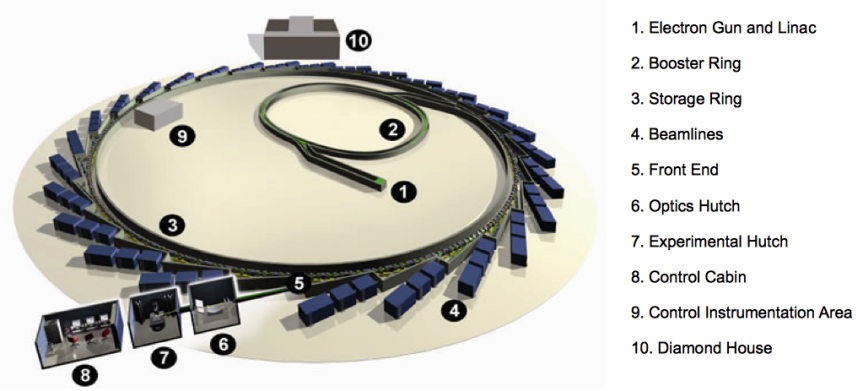

Figure 1.2: A 3D overview model of Diamond Light Source [18]

Although successfully operational, research is still ongoing into decreasing the emittance to further increase the machine's brilliance. Diamond's nominal emittance is 2.74 nm rad horizontally and 0.03 nm rad vertically [36], however efforts have already decreased the vertical emittance down to 8 pm rad [37]. A recent investigation has led to the testing of a single lattice cell upgrade to a multi-bend achromat, aiming to increase the number of straight sections per cell from 2 to 3 to provide additional beamlines to users, with simulations additionally showing a horizontal emittance reduction by a factor of 10 if every cell were to be upgraded [38].

Other than the decreased emittance, efforts are still ongoing to improve other operational aspects of the machine. The electron beam at Diamond, like any accelerator driven high energy particle beam, is susceptible to instabilities. Studies of collective effects on the beam for both single and multi-bunch operation have been conducted [39], with the implementation of a transverse feedback system already shown to damp multi-bunch instabilities [40], however work is still continuing.

1.4 The Microbunching Instability

In addition to the aforementioned transverse instabilities, interesting observations in 2009 at Diamond have shown the presence of a longitudinal phenomenon, known as the microbunching instability [41, 42]. Not exclusive to Diamond, the first evidence of the instability was recorded during the initial pursuit of observing coherent synchrotron radiation (CSR), it was seen as both steady-state and bursting (due to the then unknown microbunching instability) at several facilities including Synchrotron Ultraviolet Radiation

Facility SURF II [43], SURF III [43], SuperACO [44], VUV at BNL [45, 46], Max-I [47], BESSY-II [48], UVSOR-II [49], and the Advanced Light Source [50].

Radiation emitted during operation with a stable bunch would usually be coherent for wavelengths of the order of the bunch length σ_z and longer. The microbunching instability however, produces bursts of coherent radiation with wavelengths shorter than the bunch length. The instability is only present above a threshold current, at which point the bursts appear quasi-periodic. A localised density fluctuation is believed to occur at the instability onset due to the coherent nature of the emissions, and subsequent increases in bunch current causes a chain effect leading to the bursting [51]. At high current, the bursting then appears to be emitted at random.

The density fluctuation at the origin of the instability is believed to be based on beam impedances as a result of collective effects with subsequent motion inside the bunch affecting the longitudinal charge distribution. This prevents steady-state coherent emissions with wavelengths $< \sigma_z$, resulting in the observed bursting behaviour. Although extensive investigations have been conducted into the microbunching instability, a full model explaining all the observed behaviour of the phenomenon remains to be found. Details of current theories of the instability are discussed further in section 2.3.

Many of the experimental investigations into the instability have focussed on understanding the beam conditions necessary to trigger its onset, particularly lattices which operate with a low momentum compaction factor. This mode of operation, more commonly known as low alpha mode, is discussed further in section 2.4. An advantage of low alpha mode is a reduced bunch length, which consequently produces a broader coherent spectrum with emissions up to the THz and possibly far infrared regions. The bunch, however, is more susceptible to longitudinal density fluctuations being driven by the increase in coherent emissions. As a result, the threshold current of the microbunching instability is lower.

The microbunching instability has also been observed and studied at Diamond Light Source [52]. The low alpha lattice was designed and initially implemented at Diamond Light Source in 2008 which can now provide a bunch length as low as ~ 1 ps [53]. Since then, dedicated short runs are periodically operated where low alpha mode is made available to users [54]. The instability's presence, however, limits the bunch current to about two orders of magnitude lower in comparison to normal operation [52]. Beam size measurements both transversely and longitudinally are typically performed using diagnostic

instrumentation based on optical techniques, however bunches of the size accelerated in low alpha mode are challenging to measure experimentally.

The short bunches produced in machines such as third generation light sources and FELs makes longitudinal profile measurements an active field of research. Several techniques that currently exist are briefly described below

1.5 Longitudinal Profile Measurement Techniques

Methods for measuring the longitudinal profile can be broadly grouped into two categories of measurement; time domain and frequency domain [55]. Both domains include multiple techniques, however their applicability varies significantly, either in temporal resolution or in physical viability.

1.5.1 Time Domain Techniques

1.5.1.1 Streak Camera

A streak camera performs time domain measurements typically using radiation in the visible region of the electromagnetic spectrum. The principle of operation for a typical streak camera is shown in figure 1.3. It uses a photo cathode to convert the incident photons to electrons, whereupon a streak tube then accelerates the electrons longitudinally. Two pairs of sweep electrodes deflect the electrons transversely with a time dependant electric field, thus rotating a longitudinal temporal profile into a transverse spatial distribution. The electrons then hit a fluorescent screen which is imaged by a charge coupled device (CCD).

Several factors determine a streak cameras resolution, including the optics in the radiation transfer line, the electrode sweep speeds, the resolution of the CCD, etc. A streak camera is presently installed at Diamond which measures bunch lengths using visible radiation emitted from bunches in a dipole field. The streak camera typically has a resolution of 1 ps, however its performance is severely inhibited when bursting from the microbunching instability is occurring, especially in low alpha operation. This occurs as several sweeps are needed to build a temporal profile, whilst variations in the pulse shape courtesy of the changing bunch substructure result in a blurred image and any sub-structure cannot determined. A description of the streak camera and other diagnostic instrumentation is given in sections 4.1.2 and 4.1.2.1.

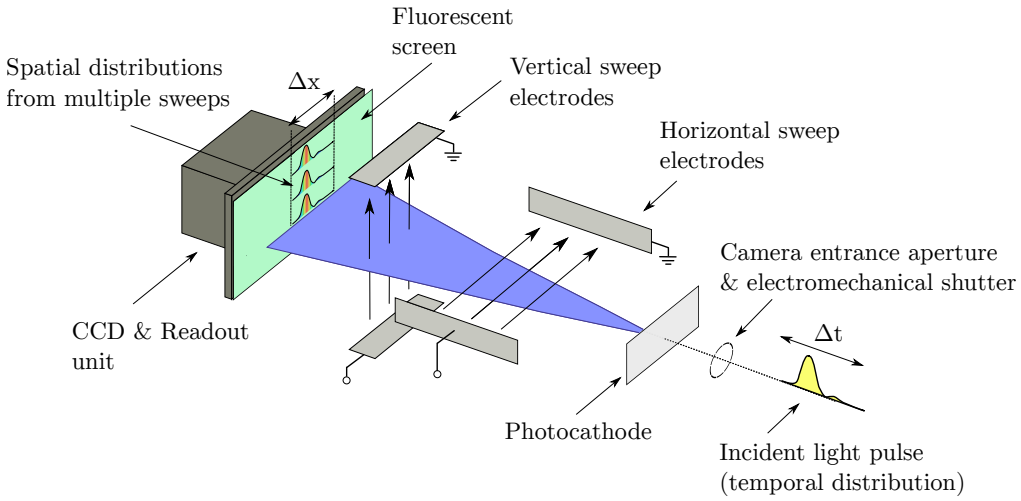

Figure 1.3: Example showing the principle of operation of a streak camera.

1.5.1.2 Transverse Deflecting Cavities

A deflecting cavity operates using a similar principle to a streak camera by converting the longitudinal profile into a transverse profile, however deflecting cavities apply the rotation to the original particle bunch. This is achieved using a transverse RF cavity, the electric field provides a small kick to the bunch with the deflecting cavity phase set such that the head and tail of the bunch are deflected in opposite directions, with the mean bunch position being unaffected. The bunch is then imaged using optical techniques, however this is a destructive measurement causing severe beam losses [56–58].

A deflecting cavity offers a very high resolution, recent results from the LCLS at SLAC have achieved a resolution of the order of 1 femtosecond [59]. The deflecting cavities, however, are costly, they are typically a few metres in length thus need a significant space in the beam line and additionally require the installation of the accompanying RF system. As such, deflecting cavities are not installed in storage rings.

1.5.1.3 Electro-Optic Techniques

Electro-optical bunch measurements are based upon the change in birefringence of an electro-optical crystal. A linearly polarised laser beam passes through the crystal, followed by an arrangement of polarisers. The electric field of a passing particle bunch induces a change in birefringence of the crystal, which is seen as a change in intensity in the detector system. In addition to bunch length measurements, the electro-optical technique can be

used as a beam position monitor [60, 61].

Similar to deflecting cavities, the electro-optical system offers good resolution down to 90 femtoseconds [56], however they are another costly technique to light sources as it requires the installation of both an in-vacuum system in the beam line where the crystal is positioned, and the necessary laser system. The proximity of the crystal to the beam creates the additional problem of the wakefield interfering with the bunch, an effect that is generally avoided in storage rings.

1.5.1.4 Summary

Both the transverse deflecting cavities and electro-optic technique pose significant impracticalities for installation in an operational third generation light source. For a storage ring such as Diamond Light Source where space along the accelerator is a premium, and a high current stable beam must be provided for users, most time domain methods are not plausible.

1.5.2 Frequency Domain Techniques

A more viable technique for Diamond Light Source is by spectral measurement using optical systems. The basis of this method is to measure the emitted coherent radiation and then reconstruct the longitudinal distribution. The coherent spectrum can either be naturally generated by charged particles propagating through a magnetic field, as is the case with CSR, or induced from processes such as Transition Radiation (TR) [62] or Diffraction Radiation (DR) [63]. The induction method is based upon charged particles propagating into (TR) or in the vicinity of (DR) a medium with different dielectric constant to that in which the beam propagates. In the case of TR, the beam strikes a target whereupon the beam is scattered and lost. As TR is an inherently destructive technique, it is generally unviable for use in a storage ring.

For DR, the beam passes through an aperture positioned such that the DR is emitted at an angle relative to the electron beam's direction of propagation. Whilst being non-destructive to the beam, it requires the installation of a vacuum chamber and apparatus to hold or move the aperture, as well as optical components to transport the radiation to a viewport window. The most feasible method is to use the naturally emitted CSR, it is a non-destructive technique which does not require any installation of apparatus directly in the beam pipe.

The spectral information can be obtained by Fourier transform spectroscopy, typically performed by either a grating spectrometer or an interferometer. This technique has the capability to only measure the power spectrum, any information regarding the phase of the radiation is lost. This can be compensated for by approximating a minimum phase, using techniques such Kramers-Kronig analysis. This frequency domain technique is discussed further in chapter 3. Given the potentially large bandwidth of coherent radiation from a short bunch, the choice of detector in the spectroscopic technique is important. Several types of detector are commercially available, however their suitability and performance must be considered. The detectors are discussed further in section 4.5.

1.6 Motivation

Whilst the majority of the electromagnetic spectrum is well known and used, the band of frequencies between 0.1 to 10 THz known as the THz gap is currently deficient in cheap technologies for generation and detection. In recent years, this region has become scientifically accessible from light sources with short bunches. The high intensity in this band has provided the opportunity to investigate a wide array of applications such as spectroscopy, time resolved experiments, imaging, etc.

The microbunching instability is a phenomenon known to produce bursts of coherent THz radiation in this frequency range, however the lack of stability presently prevents its use as a viable THz source. Its presence has been observed at multiple facilities including those which have the ability of low alpha operation such as Diamond Light Source. Of significant interest is the example of the low alpha mode of operation at BESSY-II; rather than the quasi-optical bursting as one would expect from the instability, steady-state coherent emissions in the THz region were observed [48, 64]. If such conditions were achievable at Diamond, the steady-state emission permits the possibility of dedicated THz beamlines, however the onset of the instability currently prohibits the generation of the desired steady high intensity coherent radiation. In addition, the instability jeopardises the performance of the storage ring in its present condition where users require stable steady flux of the incoherent radiation.

The mechanism that drives the instability is not well understood, therefore either its damping or exploitation into a bunch of very high charge with steady THz emission has yet to be demonstrated. To understand the instability at Diamond, a characterisation of

its behaviour with varying beam conditions is required. Diamond is presently in its third phase of development, with beamlines currently under construction. The majority of these beamlines use radiation produced from insertion devices, therefore the radiation emitted from some of the lattice dipoles is available for beam diagnostics. Most of the techniques for measuring the longitudinal profile described in the previous section are unfeasible due to their cost and the high beam losses that they incur, however the radiation which is naturally abundant in a third generation light source can be used, as evidenced by the prior installation and use of a streak camera.

The potential of high intensity THz production led to the installation of a viewport dedicated to mm-wave diagnostics during the investigation described in this thesis. Following the initial observations of the instability and the development of a low-alpha lattice, this viewport provided an excellent opportunity to study the instability further. The CSR from the viewport can be measured experimentally using the frequency domain method, requiring the development and installation of a spectroscopic instrument. A technology that has recently become commercially available is room temperature Schottky Barrier Diode (SBD) detectors, which provide high sensitivity and an ultra-fast response time. One particular model of SBD detector operates between 100 and 1000 GHz, the region of interest for coherent radiation for short bunches. A detector with this bandwidth is ideal for use in an interferometer, whereupon the coherent spectrum can be measured and the longitudinal bunch distribution can be reconstructed.

Chapter 2

Theory

This chapter provides an overview of the theory of the emitted radiation. It will describe the power spectrum emitted from a single electron and the origins of coherent spectrum as a result of multiple electrons in a bunch. An overview to the existing theory of the microbunching instability is given, focussing on the instability threshold current for known beam conditions. The instability's applicability to Diamond Light Source is briefly discussed, including an overview of the low-alpha operation which is particularly susceptible to the instability.

2.1 Synchrotron Radiation

One of the well known fundamental rules of physics is that any charged particle that is undergoing acceleration will emit electromagnetic radiation. The term *bremsstrahlung*, translated as braking radiation, is usually considered for radiation emission when charged particles interact with other matter and decelerate. The term, however, is also accurate for synchrotrons, the difference being that the applied acceleration is perpendicular to the particle's trajectory rather than opposite or parallel. The magnetic dipoles used in synchrotrons are one of the primary sources of the perpendicular acceleration, designed for steering the beam whilst additionally generating large amounts of radiation.

To calculate the power of the radiation emitted from a relativistic electron of energy E undergoing an acceleration, we can use the Larmor formula [15]:

$$P_\gamma = \frac{1}{6\pi\epsilon_0}\frac{e^2}{m_0^2c^3}\left[\left(\frac{d\vec{p}}{d\tau}\right)^2 - \frac{1}{c^2}\left(\frac{dE}{d\tau}\right)^2\right], \tag{2.1}$$

where e is the electron charge, c is the speed of light in a vacuum, m_0 is the electron rest mass, ϵ_0 is the vacuum permittivity, and $\vec{p}$ is the electron's momentum. For the perpendicular case, we can ignore the second term in equation 2.1 as the energy loss is negligible in comparison to the electron's energy. Including the Lorentz transformation $dt = \gamma d\tau$ such that the power emitted is observed in the laboratory frame, we can write,

$$P_\gamma = \frac{e^2 c}{6\pi\epsilon_0} \frac{\gamma^2}{m_0^2 c^4} \left(\frac{dp}{dt}\right)^2, \tag{2.2}$$

where γ is the Lorentz factor,

$$\gamma = \frac{E}{E_0} = \frac{E}{m_0 c^2}. \tag{2.3}$$

The centripetal force that the electron experiences through the dipoles during a complete revolution of a storage ring is simply:

$$\left(\frac{dp}{dt}\right) = \frac{mc^2}{\rho} = \frac{\gamma m_0 c^2}{\rho}, \tag{2.4}$$

where ρ is the dipole bending radius. Substituting this into equation 2.2, we obtain the formula for power in equation 1.2. This expression can be reduced further by introducing the fine structure constant,

$$\alpha = \frac{e^2}{4\pi\epsilon_0 c\hbar}, \tag{2.5}$$

where $\hbar$ is the reduced Planck constant. This gives us a final expression for the total power emitted from a single electron travelling in a circular trajectory at a given energy,

$$P_\gamma = \frac{2}{3} \frac{c^2 \gamma^4}{\rho^2} \hbar\alpha. \tag{2.6}$$

The dipoles at Diamond Light Source have a bending radius of 7.13 m, so for an electron at 3 GeV, equation 2.6 give an emitted power of ~ 1.1 μW. Whilst this tells us the total instantaneous power emitted, in reality this power will be emitted across a broad spectrum of wavelengths. If we are to investigate emissions in a finite bandwidth, the complete power spectrum must be known.

2.2 Coherent Synchrotron Radiation

To calculate the power spectrum from electrons in a storage ring, we must consider the case of a bunch consisting of many particles. The length of the bunch is a key factor in whether radiation of a given frequency will be emitted coherently or incoherently. Consider a 1 dimensional bunch distribution of length σ_z. For a radiation wavelength $\lambda \ll \sigma_z$, the phases of the emissions are distributed randomly, so the radiation from multiple electrons would appear incoherent due to the multiple radiation phases, as shown in figure 2.1 [65] for two electrons. For the case of $\lambda \leq \sigma_z$, a fraction of the bunch will radiate in phase and be coherent, and a part of the bunch will still radiate incoherently, thus a regime with both coherent and incoherent emission exists. When $\lambda > \sigma_z$, coherent radiation dominates; figure 2.2 [65] shows this for the case where the distance between two electrons is small in comparison to the wavelength being observed, resulting in the radiation being emitted in phase.

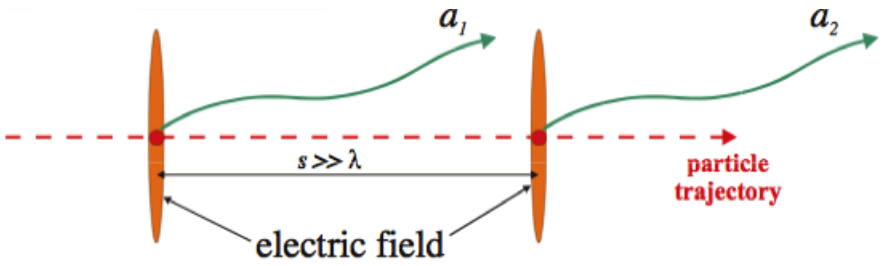

Figure 2.1: Two electrons generating incoherent radiation.

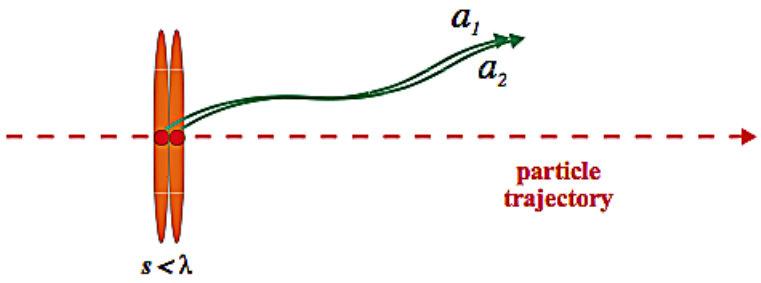

Figure 2.2: Two electrons generating coherent radiation.

The intensity of the emitted radiation is noticeably different for the two different cases. We can derive the result for the intensity of the coherent emissions as follows [66]. Let's define the distance from the centre of the bunch to the j^{th} electron as $\vec{r}_j$. We can then write the total radiation field from N electrons at a frequency of ω as

$$\vec{E}_{total}(\omega) = \sum_{j=1}^{N} \vec{E}_j(\omega) e^{i(\omega t - \vec{k}_j \cdot \vec{r}_j)}, \tag{2.7}$$

where $\vec{k}_j = k\vec{n}_j = \frac{\omega}{c}\vec{n}_j$ which is the wavenumber of the j^{th} electron, with a unit vector direction of $\vec{n}_j$ to the observer. In the far-field approximation where the whole bunch can be thought of as a point source, then we write $\vec{n}_j = \vec{n}$ and $\vec{E}_j(\omega) = |E_j(\omega)|\,\vec{n}$. The radiation intensity can therefore be written as

$$\begin{aligned} I(\omega) &\propto \left|\vec{E}_{total}(\omega)\right|^2 \\ &\propto \left|\sum_{j=1}^{N} E_j(\omega) e^{ik\vec{n}\cdot\vec{r}_j}\right|^2 \\ &= \sum_{j=1}^{N} E_j(\omega) e^{ik\vec{n}\cdot\vec{r}_j} \sum_{m=1}^{N} {E_m}^*(\omega) e^{-ik\vec{n}\cdot\vec{r}_m} \\ &= \sum_{j=m}^{N} |E_j(\omega)|^2 + \sum_{j=1}^{N} \sum_{m=1, m\neq j}^{N} E_j(\omega) {E_m}^*(\omega) e^{ik\vec{n}\cdot(\vec{r}_j - \vec{r}_m)}. \end{aligned} \tag{2.8}$$

In the case where $m = j$, then the intensity from a single electron, denoted by $I_e(\omega)$, can be written as $I_e(\omega) = E_j(\omega){E_j}^*(\omega) = |E_e(\omega)|^2$ where $E_e(\omega)$ is the field from the electron. Therefore

$$\sum_{j=m}^{N} |E_j(\omega)|^2 = N I_e(\omega). \tag{2.9}$$

In the case where $m \neq j$, then a form factor for the fields must be considered. If we assume the radiation field generated by every individual electron in the bunch is the same, then the radiation from the whole bunch can be written as

$$E_j(\omega){E_m}^*(\omega) = I_e(\omega) s(\vec{r}_j) s(\vec{r}_m), \tag{2.10}$$

where $s(\vec{r})$ is the bunch distribution. Equation 2.8 can then be written as

$$I(\omega) = N I_e(\omega) + \sum_{j=1}^{N} \sum_{m=1, m\neq j}^{N} E_j(\omega) {E_m}^*(\omega) e^{ik\vec{n}\cdot(\vec{r}_j - \vec{r}_m)}$$
$$= N I_e(\omega) + N(N-1) I_e(\omega) \sum_{j=1}^{N} \sum_{m=1, m\neq j}^{N} e^{ik\vec{n}\cdot(\vec{r}_j - \vec{r}_m)} s(\vec{r}_j) s(\vec{r}_m). \quad (2.11)$$

As the right hand side of equation 2.11 is now only dependant on the $\vec{r}_j$ and $\vec{r}_m$ distances, then we can convert the summations to integrals:

$$I(\omega) = N I_e(\omega) + N(N-1) I_e(\omega) \int_{-\infty}^{\infty} s(\vec{r}_j) e^{ik\vec{n}\cdot(\vec{r}_j)} d\vec{r}_j \int_{-\infty}^{\infty} s(\vec{r}_m) e^{-ik\vec{n}\cdot(\vec{r}_m)} d\vec{r}_m$$
$$= N I_e(\omega) + N(N-1) I_e(\omega) \left| \int_{-\infty}^{\infty} s(\vec{r}) e^{ik\vec{n}\cdot(\vec{r})} d\vec{r} \right|^2 . \quad (2.12)$$

We must now consider the integral in equation 2.12. As we are considering relativistic electrons, usually the transverse electric field is substantially larger than the longitudinal field. Practically, however, the transverse beam dimensions in most accelerators are much smaller than the longitudinal dimensions. Therefore, as the longitudinal form factor approaches unity, the transverse form factor is already unity, and thus can be omitted. We can therefore write our form factor as dependant only on the longitudinal distribution z, thus the direction $\vec{n}$ reduces to unity, and substituting $k = \frac{\omega}{c}$, we get

$$F(\omega) = \left| \int_{-\infty}^{\infty} s(z) e^{i\frac{\omega}{c} z} dz \right|^2 . \quad (2.13)$$

This longitudinal form factor here is the square of the modulus of a Fourier transform of a longitudinal charge distribution, $s(z)$ [67]. The final equation for the emitted spectrum from a bunch of N electrons therefore becomes

$$I_{total}(\omega) = I_e(\omega)[N + N(N-1)F(\omega)]. \quad (2.14)$$

The first term in equation 2.14, proportional to N, corresponds to the incoherent emissions, whereas the second term, proportional to N^2, corresponds to the coherent

emissions. As the spectrum from a single electron is well defined, the bunch spectrum now becomes highly dependant on the form factor, and subsequently the charge distribution. If we consider a normalised 1 dimensional Gaussian distribution for the longitudinal charge distribution,

$$s(z) = \frac{1}{\sqrt{2\pi}\sigma_z} e^{\left(-\frac{z^2}{2\sigma_z^2}\right)}, \tag{2.15}$$

then the form factor can be calculated from

$$F(\omega) = \left| \int_{-\infty}^{\infty} \frac{1}{\sqrt{2\pi}\sigma_z} e^{\left(-\frac{z^2}{2\sigma_z^2}\right)} e^{\left(i\frac{\omega}{c}z\right)} dz \right|^2. \tag{2.16}$$

This can be solved using the following standard integral,

$$g(x) = \int_{-\infty}^{\infty} e^{-ax^2} e^{bx} dx = \sqrt{\frac{\pi}{a}} e^{\left(\frac{b^2}{4a}\right)}, \tag{2.17}$$

where $a = \frac{1}{2\sigma_z^2}$ and $b = i\frac{\omega}{c}$ [68]. This therefore makes the form factor

$$F(\omega) = \left| \frac{1}{\sqrt{2\pi}\sigma_z} \sqrt{2\pi\sigma_z^2} e^{\left(-\frac{\omega^2}{c^2}\frac{\sigma_z^2}{2}\right)} \right|^2. \tag{2.18}$$

This can be simplified down to:

$$F(\omega) = e^{\left(-\left(\frac{\omega\sigma_z}{c}\right)^2\right)}. \tag{2.19}$$

As the second term in equation 2.14 is proportional to N^2, then the form factor must be greater than $1/N$ to be of significance. Thus, from equation 2.19, it can be shown that coherent emissions occur for wavelengths given in the relation in equation 2.20.

$$\lambda < \frac{2\pi\sigma_z}{\sqrt{ln(N)}} \tag{2.20}$$

Figure 2.3 shows the coherent spectrum calculated using equation 2.14 based upon a Gaussian form factor for three bunch lengths of 0.5 mm, 1 mm, and 2 mm. The number of particles in the bunch was chosen to be 10^{10}, which given the bunch revolution rate of 533.820 kHz at Diamond corresponds to a current of $\approx 0.9\ mA$. This is a reasonable value for a single bunch during standard operation.

Whilst we now have an estimated form factor for a bunch of electrons, to calculate

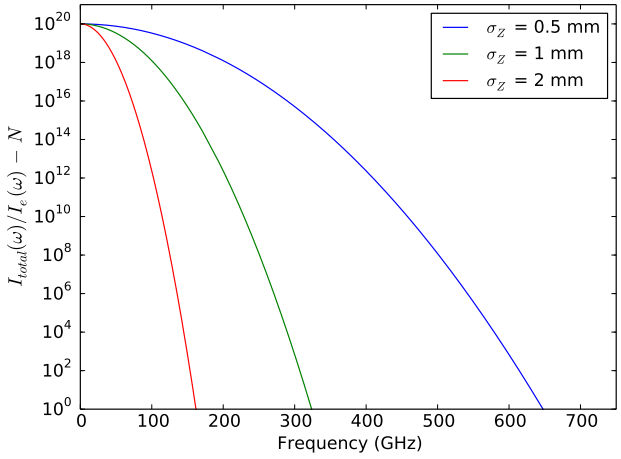

Figure 2.3: Amplitudes of the coherent spectrum from a bunch of $N = 10^{10}$ electrons in a Gaussian distribution with lengths of 0.5 mm, 1 mm, and 2 mm.

the complete power spectrum we need the spectrum emitted from a single electron, I_e, which is given in equation 2.21 [22].

$$I_e = \left(\frac{d^2I}{d\theta d\omega}\right)_e = \left(\frac{q^2}{4\pi\epsilon_0 c}\right)\frac{\sqrt{3}\gamma}{2\pi}\left(\frac{\omega}{\omega_c}\right)\int_{\omega/\omega_c}^{\infty} K_{5/3}(y)dy \tag{2.21}$$

This is the emitted spectrum integrated over all vertical angles, for the sum of both the horizontal and vertical polarisation states, where K is a modified Bessel function, and ω_c is the critical frequency, given by

$$\omega_c = \frac{3c\gamma^3}{2\rho}, \tag{2.22}$$

where ρ is the dipole bending radius. A concise derivation of equation 2.21 can be found in appendix A. The graphical representation of equation 2.21 is shown in figure 2.4, along with the critical frequency from equation 2.22 as $f_c = \frac{\omega_c}{2\pi}$.

Additionally, by integrating equation 2.21 over 2π radians and over all frequencies, we can get the total energy emitted by an electron in one revolution of the storage ring:

$$I_e = \left(\frac{q^2}{4\pi\epsilon_0 c}\right)\frac{\sqrt{3}\gamma}{2\pi}\int_0^{2\pi}\left(\frac{\omega}{\omega_c}\right)\left[\int_{\omega/\omega_c}^{\infty} K_{5/3}(y)dy.\right]d\theta \tag{2.23}$$

The numerical value of the integral in equation 2.23 is calculated in [22] to be $8\pi\omega_c/9\sqrt{3}$, and using the definition of ω_c from equation 2.22 and the fine structure constant

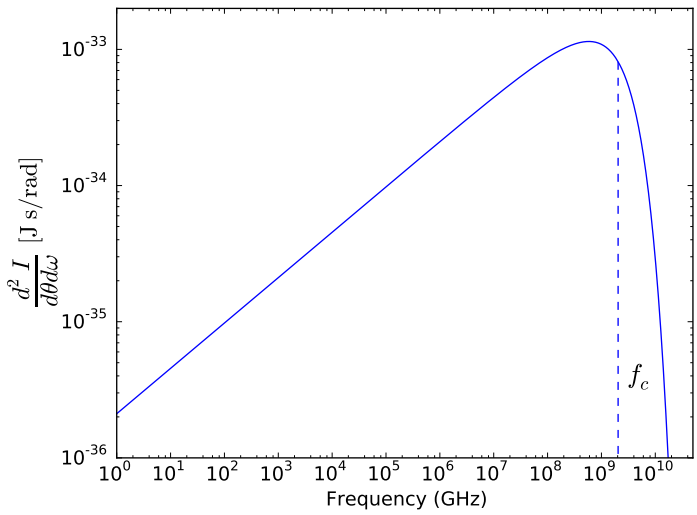

Figure 2.4: Single electron spectrum as a function of emission frequency for Diamond Light Source.

in equation 2.5 gives:

$$I_e = \left(\frac{q^2}{4\pi\epsilon_0 c}\right)\frac{8\pi}{9}\frac{3\gamma^3 c}{2\rho} = \alpha\hbar\frac{\gamma^4 c}{\rho}\frac{4\pi}{3}. \tag{2.24}$$

To get the power emitted per turn, we divide by the time the electrons are radiating in the dipole fields in one revolution, $2\pi\rho/c$, to give:

$$I_e = \alpha\hbar\frac{2}{3}\frac{\gamma^4 c^2}{\rho^2}. \tag{2.25}$$

This is identical to the expression for Larmor's formula in equation 2.6. By using the expressions in equations 2.19 and 2.21, we can now calculate the total bunch spectrum. Figure 2.5 shows the spectrum from a 0.5 mm long Gaussian bunch of 10^{10} electrons, from equation 2.14 .The coherent part of the spectrum is notably a factor N higher in intensity compared to the incoherent part at the same wavelengths, as indicated by the dashed line.

2.3 The Microbunching Instability

Thus far, we have worked under the assumption that the longitudinal charge distribution is Gaussian. A distortion to the bunch charge density leading to the formation of non-Gaussian distributions will therefore inevitably effect the coherent spectrum. It is

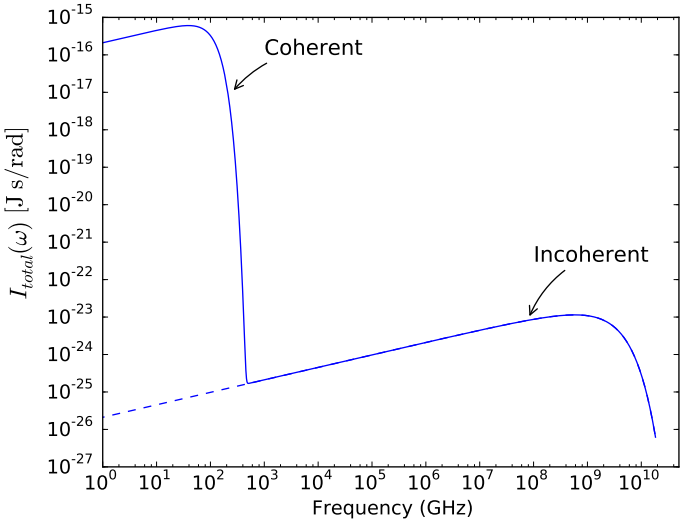

Figure 2.5: Emitted spectrum from a bunch of $N = 10^{10}$ electrons with a 0.5 mm long Gaussian longitudinal charge distribution.

known that the emission of coherent radiation with wavelengths much shorter than the bunch length must be a result of sub-structure in the bunch. This sub-structure is generally believed to be a result of the appearance of an initial small density fluctuation, with a characteristic wavelength shorter than the bunch length, however the mechanism which triggers this density fluctuation is not well understood. This fluctuation then grows leading to further small sub-structures inside the bunch, i.e. micro-bunches, however the emission of coherent short wavelengths in bursts indicates that the bunch structure varies significantly over time. Several publications have described the same behaviour of bursts of coherent emissions which are initially emitted quasi-periodically, with high current bunches emitting in an apparent random manner [43–50, 69].

Thus far, two approaches have been developed to model the instability. Both models are based upon the same technique, however, their applicability differs depending on machine parameters, primarily the bunch length. The leading cause of the instability is believed to be collective effects, especially wakefields [51], which triggers the initial onset of the density fluctuation. A common method of modelling particle accelerators is tracking of macro-particles, however, another method has been developed based upon solutions to the Vlasov-Fokker-Planck (VFP) equation in 1 dimension, incorporating the forces experienced by a particle from the collective effects [70]. This method has the advantage of allowing small scale sub-structure without granulating phase space as in the

macro-particle tracking method.

Both models are described in further detail in [51, 70, 71], however for the purposes of this thesis, a concise overview of these sources will be given.

2.3.1 Coasting Beam Theory

The first model is based only on the Vlasov part of the VFP equation, which describes the bunch dynamics on short time scales [72]. The linearization of the Vlasov equation (LV) is performed for a longitudinal distribution function f that is the sum of an equilibrium distribution f_0 with a perturbation f_1, with $f_1 \ll f_0$ [73]. The perturbation is typically chosen to be a small amplitude sinusoid, with the equilibrium distribution chosen to be a standard Gaussian. The RF focussing term in the LV equation is then dropped such that the beam is unbunched, more commonly referred to as coasting, thus giving rise to its name of the coasting beam theory (CBT).

The term describing the collective effects however, still remains. The CBT collective effects focuses primarily on the CSR wakefield. The CSR wakefield arises from the emitted photons, which given that the emission is tangential to the electron's path, the CSR wakefield is therefore located in front of the particle in contrast to a conventional trailing wake. For a relativistic electron in a dipole with bending radius ρ, the one dimensional longitudinal wake for free space is given (as an approximation) by equation 2.26 [24,51,74]. As the wake is only found in front of a particle, equation 2.26 is only valid in free space for $z > 0$ where z is the longitudinal position.

$$W_{csr}(z) = -\frac{2}{\rho^{2/3}(3z)^{4/3}} \tag{2.26}$$

As the wakefield arises from CSR, which we know from section 2.2 can extend over a large bandwidth for short bunches, then the impedance from the wake will vary with wavelength. The impedance as a result of the wakefield can be calculated through the Fourier transform of the wakefield, as calculated in [75] as,

$$\begin{aligned} Z(k) &= \frac{1}{c}\int_0^\infty W(z)e^{-ikz} \\ &= -\frac{2\pi}{c}\frac{\Gamma\left(\frac{2}{3}\right)\left(\sqrt{3}+i\right)}{3^{1/3}}\left(\rho k\right)^{1/3}, \end{aligned} \tag{2.27}$$

where k is the wavenumber, $i = \sqrt{-1}$, and Γ is the gamma function [76] defined as

$$\Gamma(x) = \int_0^\infty t^{x-1} e^{-t} dt = (x-1)!. \tag{2.28}$$

Using the impedance in equation 2.27, the analysis in [73] show that the beam becomes unstable for a bunch of current I if

$$k\rho < 2 \left(\frac{I}{\alpha \gamma \sigma_E^2 I_A} \right)^{\frac{3}{2}}, \tag{2.29}$$

where σ_E is the bunch energy spread, α is the momentum compaction factor, and I_A is the Alfven Current, defined as

$$I_A = 4\pi\epsilon_0 mc^3/e \approx 19kA. \tag{2.30}$$

It should be noted that this result states that there is always an unstable wavelength which causes the initial microbunching effect. By defining the current as

$$I = \frac{\sqrt{2\pi}\rho I_b}{\sigma_z}, \tag{2.31}$$

where I_b is the bunch current, then we can write the bunch threshold current as [50, 71]

$$I_b > \frac{\pi^{1/6}}{\sqrt{2}} \frac{ec}{r_e} \frac{\gamma}{\rho^{1/3}} \alpha \sigma_E^2 \frac{\sigma_z}{\lambda^{2/3}}, \tag{2.32}$$

where r_e is the classical electron radius. This relation however, was shown to only be valid for longer wavelengths where $\sigma_z > \lambda/2\pi$ [50]. In addition to the CSR wakefield, the impedance due to the shielding from the vacuum beam pipe must be taken into consideration as the low frequency region of the spectrum is particularly affected by the shielding. The effect of the shielding at synchrotron light sources has previously been studied based upon a parallel plate model [67], with the model describing a suppression of frequencies. Between two plates of separation g, particles moving on a circular trajectory of radius ρ will only emit frequencies above a cutoff given by the relation in equation 2.33 [67, 70]. More elaborate models have been investigated, but all have similar cutoffs to that shown in equation 2.33 [70].

$$\lambda_{\text{cutoff}} = 2g \left(\frac{g}{\rho} \right)^{\frac{1}{2}} \tag{2.33}$$

Therefore, from this cutoff and from the upper limit from equation 2.20, we get the frequency range in which the emissions radiate coherently for N electrons as

$$\frac{2\pi\sigma_z}{\sqrt{ln(N)}} > \lambda > 2g\left(\frac{g}{\rho}\right)^{\frac{1}{2}}. \tag{2.34}$$

Diamond Light Source has a vacuum chamber with vertical aperture of 38 mm, and a dipole bending radius of 7.13 m, therefore the low frequency cutoff is estimated to be 54 GHz ($\sim 5.5\ mm$) [41,77]. It should also be noted that a criterion for where the shielding effect becomes negligible [78, 79] was derived:

$$\frac{\sigma_z}{h}\left(\frac{2\rho}{h}\right)^{\frac{1}{2}} \leq 0.2, \tag{2.35}$$

where $h = \frac{g}{2}$. From equation 2.35 and using parameters in the above paragraph, then the shielding only becomes negligible at Diamond for bunches shorter than 0.139 mm (0.46 ps). The generation of bunches this short is very difficult to verify given the current diagnostic equipment. As bunches may be affected by the shielding, its effect on the impedance must be considered. The wakefield for the parallel plates case is derived in [75] along with its corresponding impedance, however the impedance is given in [71] in terms of the more familiar Airy functions Ai and Bi as:

$$\begin{aligned}\frac{\rho}{h}\frac{Z(k)}{k\rho} = & \frac{16\pi^3 2^{\frac{1}{3}}}{c}\left[k\rho\left(\frac{h}{\rho}\right)^{\frac{3}{2}}\right]^{-\frac{4}{3}} \\ & \times \sum_{j=1,3,5\ldots}\left[Ai'(u)Ci'(u) + uAi(u)Ci(u)\right],\end{aligned} \tag{2.36}$$

where $Ci = Ai - iBi$ and

$$u = \frac{\pi^2 j^2}{2^{\frac{2}{3}}}\left[k\rho\left(\frac{h}{\rho}\right)^{\frac{3}{2}}\right]^{-\frac{4}{3}}, \tag{2.37}$$

where j is the index of summation in equation 2.36. Figure 2.6 shows a plot of both the CSR impedance in free space from 2.27 and the CSR impedance between parallel plates from 2.36 as shown in [71]. Clearly for shorter wavelengths the impedance asymptotically matches the free space model. The criterion for the effect of the parallel plates becoming a negligible impedance from 2.35 for $f \approx 2.15$ THz is also observed (assuming the impedance

wavelength is equal to the bunch length).

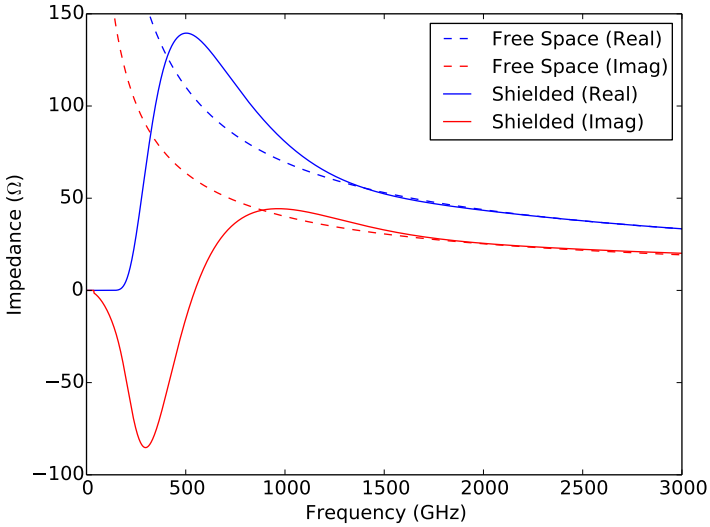

Figure 2.6: Scaled Impedances for the CSR wake in free space and parallel plates from [71].

With the parallel plates impedance, the analysis in [71] of the LV equation revealed that the condition for the beam becoming unstable changed to

$$\frac{Ih}{\alpha\gamma\sigma_E^2 I_A \rho} < \frac{\pi}{6}, \tag{2.38}$$

which is valid for all wavelengths shorter than the shielding cutoff. From this inequality, and using equations 2.38 and 2.31, the bunch threshold current can be written as

$$I_b > \frac{3\sqrt{2}\alpha\gamma\sigma_E^2 I_A \sigma_z}{\pi^{\frac{3}{2}} h}. \tag{2.39}$$

Notably different to the expression for free space (equation 2.32), the presence of shielding clearly has an impact of the predicted threshold current. Beyond the threshold, the LV method breaks down as the instability reaches a non-linear regime. An analysis in [70] for a solution of the non-linear Vlasov equation shows that beyond the growth of the perturbation into microbunching, a saturation point is reached, whereupon the perturbation relaxes and the bunch reaches an equilibrium distribution. This process of initial density fluctuation leading to growth and microbunch formation followed by relaxation into a smooth distribution can therefore be considered a burst.

2.3.2 Bunched Beam Theory

Whilst the CBT has provided a testable inequality for the instability threshold, the physical reality is that most accelerators, including light sources, have bunched beams. Following on from the analysis in [72], the RF focussing term was included in their calculations thus giving rise to the bunched beam theory (BBT).

As the wakefields interact with the particles, the effect of the wakefield on the whole bunch must be considered. To do this, an equilibrium longitudinal distribution is needed which accounts for wakefield interactions, such as the aforementioned CSR wake and vacuum chamber shielding wake from section 2.3.1. This is achieved using the Haissinski equation as shown in appendix C.1 [51, 79]. For the case of the CSR wake, the resulting distribution remains a Gaussian for low current, however for higher currents the bunch distribution leans either forward or backward depending of the sign of the momentum compaction factor. For the case when the bunch leans forward, it exhibits a sharper leading edge with the bunch tail consequently becoming less steep, thus the centre of the bunch shifts towards the head of the bunch and is therefore seen as a shift in synchronous phase. The Haissinski distribution has been calculated for the case of a resistive wall wake as most storage rings operate with a normal conducting vacuum chamber, however, it was shown to have a negligible effect compared to the wake from parallel plate shielding [78].

The investigation into the instability once again begins with the application of a small perturbation to the longitudinal distribution. Following the solutions to the non-linear Vlasov equation for the CBT as mentioned at the end of section 2.3.1, similar calculations were performed in [70] for the BBT. The results showed similar behaviour to the CBT over a short time scale, however, they differ over a longer time period.

The instability begins at the centre of the bunch where the charge density is highest, and a ripple forms consisting of the microbunches. As the CSR wake is localised in front of a particle, only the head of the bunch is initially affected. The RF focussing is applied at a later point in time whereupon the bunch naturally rotates in phase space, therefore the instability moves to the back of the bunch. The CSR wakefield then affects the front of the bunch and the whole bunch displays the perturbation. As no damping terms are considered in the model, the energy spread and bunch length increases, moving the bunch away from the instability conditions over the course of a few synchrotron periods, however, the bunch does not return to its original higher density distribution. The full VFP equation can be analysed by including the effects of radiation damping and quantum fluctuations [24].

The analysis in [72] shows that the damping reduces the bunch length and energy spread, restoring the instability conditions, and thus repeating the bursts. Their results however, are qualitative for a specific machine (Brookhaven NSLS VUV Storage Ring) and they do not provide an inequality applicable to other machines.

Another method of the BBT in [71, 80] however, does produce an expression for the instability threshold using the LV approach for the equilibrium Haissinski distribution plus a small perturbation. For the case of the CSR wakefield in free space, the instability threshold was shown in terms of a scaled current ξ to be

$$\xi^{th} = I_n \frac{\rho^{\frac{1}{3}}}{\sigma_z{}^{\frac{4}{3}}} = 0.5, \tag{2.40}$$

where,

$$I_n = \frac{\sigma_z I_b}{\alpha \gamma \sigma_E^2 I_A}. \tag{2.41}$$

For the case of shielding from parallel plates, then the resulting threshold becomes [71]:

$$\xi^{th} = I_n \frac{\rho^{\frac{1}{3}}}{\sigma_z{}^{\frac{4}{3}}} = 0.5 + 0.34\chi, \tag{2.42}$$

where $\chi = \frac{\sigma_z \rho^{\frac{1}{2}}}{h^{\frac{3}{2}}}$. Good agreement is shown between this LV method and the aforementioned VFP method [71]. From the scaled current ξ and bunch current expression in equation 2.41, an expression relating the instability threshold, bunch current, and bunch length was derived in [71] to be:

$$\sigma_z{}^{\frac{7}{3}} = \frac{c^2 Z_0}{8\pi^2 \xi^{th}} \frac{I_b^{th} \rho^{\frac{1}{3}}}{V_{RF} \cos\phi_s f_{RF} f_{rev}}, \tag{2.43}$$

where Z_0 is the free space impedance, V_{RF} is the RF cavity voltage, f_{RF} is the RF frequency, ϕ_s is the RF synchronous phase, and f_{rev} is the bunch revolution frequency.

2.3.3 Instability Theory Comparison

Whilst it appears that the two competing theories produce different outcomes, they can be shown to produce very similar results. A similar expression to that in 2.43 can be derived for the coasting beam case in free space. The expression was derived initially in [75] and shown in [71, 78, 81] to be:

$$\sigma_z^{\frac{7}{3}} = \frac{c^2 Z_0}{2\pi F 3^{\frac{1}{3}}} \frac{I_b^{th} \rho^{\frac{1}{3}}}{V_{RF} f_{RF} f_{rev}}, \tag{2.44}$$

where F is a numerical factor which is the integral of a dimensionless form of the Haissinski distribution. A summary of this derivation as well as that of equation 2.43 can be found in appendix C. By equating this to the instability threshold expression for a coasting beam from equation 2.32 and rearranging, we find that for the case of free space:

$$F \leq \frac{{\sigma_z}^{\frac{2}{3}}}{\lambda^{\frac{2}{3}}} \left(\frac{\pi^{\frac{1}{6}} e^2 Z_0}{2^{\frac{1}{2}} c r_e 3^{\frac{1}{3}} m_e} \right) = 7.462 \frac{{\sigma_z}^{\frac{2}{3}}}{\lambda^{\frac{2}{3}}}. \tag{2.45}$$

This expression for F is often quoted assuming $\sigma_z = \lambda$, and therefore F becomes constant. For the case with shielding, equating the expressions in 2.43 and 2.44, using the the expression for ξ from equation 2.42 and assuming $\cos(\phi_s) = 1$ gives:

$$F = \frac{4\pi \xi^{th}}{3^{\frac{1}{3}}} = \frac{2\pi}{3^{\frac{1}{3}}} + 0.24\pi \left(\frac{\chi}{3^{\frac{1}{3}}} \right). \tag{2.46}$$

Clearly F is not constant when taking into account the shielding. As the factor χ is important in determining the threshold with shielding, care must be taken when applying a model. In [71], the two models are shown only to agree well when χ is greater than two. As such, it is recommended in [71] that for long bunches where $\chi > 2$, the coasting beam method via equation 2.39 should be used, and for short bunches where $\chi < 2$, the bunched beam method from equation 2.43 should be used.

2.4 Applicability at Diamond Light Source

Following the criteria for the instability threshold model selection, for Diamond Light Source, $\chi = 2$ when the bunch is 5.6 mm long ($\sim$ 18 ps). For standard operation of Diamond, the bunch is typically around 18 ps [82], therefore both models are applicable. As the low alpha operation at Diamond produces bunches of lengths around 2 ps, the bunched beam method should definitely be applied. The theoretical predictions are compared to the experimental data in section 5.2.

Following the commissioning of a low alpha lattice at Diamond [52], the microbunching instability has already been observed [41, 42]. A low alpha lattice is used to produce short x-ray pulses by shortening the longitudinal bunch length σ_z, which is achieved by lowering the momentum compaction factor, α. The reduction in bunch length is desirable

for some beam lines that require a shorter pulse duration, providing opportunities for experiments requiring a high temporal resolution [52]. The shorter bunch lengths, however, mean a shorter beam lifetime, and the onset of the microbunching instability limits the beam to a low bunch current. This results in a reduced photon flux, something undesired by the majority of the user community, hence why Diamond and other synchrotron light sources are looking to prevent the instability from developing. This would then permit a low alpha lattice with a high bunch current.

As the low alpha operation is important in the investigation of the microbunching instability, the principles of such a setup are as follows. The momentum compaction factor itself is defined as a measure of the change in path length during one revolution of the storage ring with respect to the deviation in particle momentum. Mathematically, it is written as:

$$\alpha = \frac{\Delta L/L_0}{\delta}, \tag{2.47}$$

where L_0 is the length of the ideal orbit, and δ is defined as:

$$\delta = \frac{\Delta P}{P_0}. \tag{2.48}$$

Here, P_0 is the nominal momentum. The major contributor to a change in path length are dipoles, therefore from simple geometry, we can write a particle's trajectory, ds', as:

$$ds' = \frac{\rho + x}{\rho} ds, \tag{2.49}$$

where ds is the "ideal" orbit, x is the "off-orbit" distance, and ρ is the dipole bending radius. The "off-orbit" distance is related to the momentum variations by the dispersion function $D(s)$, such that:

$$x(s) = D(s)\frac{\Delta P}{P_0}. \tag{2.50}$$

Throughout a closed orbit, the total path difference can be written as:

$$L = L_0 + \Delta L = \oint ds' = \oint \frac{\rho + x}{\rho} ds = \oint ds + \oint \frac{x(s)}{\rho(s)} ds = L_0 + \frac{\Delta P}{P_0} \oint \frac{D(s)}{\rho(s)} ds \tag{2.51}$$

Using equation 2.47 and rearranging, we get:

$$\alpha = \frac{1}{L_0} \oint \frac{D(s)}{\rho(s)} ds. \tag{2.52}$$

Alpha can be expanded as a power series to be a function of delta:

$$\alpha(\delta) = \alpha_1 + \alpha_2 \delta + \alpha_3 \delta^2 + ..., \tag{2.53}$$

where the leading order terms are:

$$\begin{aligned} \alpha_1 &= \frac{1}{L_0} \oint_{L_0} \frac{D_1(s)}{\rho} ds \\ \alpha_2 &= \frac{1}{L_0} \int_{L_0} \frac{{D_1}'(s)^2}{\rho} + \frac{D_2(s)}{\rho} ds. \end{aligned} \tag{2.54}$$

Here, D and D' are the dispersion function and its spatial derivative respectively, with the 1 and 2 subscripts referring to the order in the expansion [52]. The low alpha lattice at Diamond is achieved by introducing negative dispersion in the centre of the dipoles. By doing this, the dispersion within the dipoles retain their quadratic dependence, and consequently α_1 and the emittance are minimised. The dependence of the emittance on the dispersion can be shown by equation 2.55:

$$\epsilon = \frac{55}{32\sqrt{3}} \frac{\hbar \gamma^2}{m_e c} \frac{I_5}{I_2 - I_4}, \tag{2.55}$$

where I_5, I_2, and I_4 are radiation integrals which can be found in appendix B. The effect of implementing the dipole changes results in an increased horizontal tune, and consequently an increased chromaticity. The problem of higher chromaticity is additionally compounded when correcting the second order momentum compaction factor, α_2. From equation 2.54, the first term is only dependant on the derivative of the linear dispersion ${D'}_1$, which is fixed. The second term depends on the second order dispersion D_2, therefore α_2 can be minimised by adjusting the sextupoles to offset the first term. The combination of these two factors requires an notable increase in sextupole strength. The resulting beam parameters are shown in section 4.1.

2.5 Summary

In this chapter, the physics behind coherent synchrotron generation has been discussed. The total radiation spectrum emitted from a Gaussian electron bunch within a bending magnet has been produced, with the coherent component shown to be highly dependant on the longitudinal charge distribution. The microbunching instability, a phenomenon known to affect the charge distribution, has been described including two leading theories which provide testable predictions for the instability's threshold current. Its applicability to Diamond Light source has also been discussed, including a description of a low momentum compaction factor lattice which is particularly susceptible to the microbunching instability.

Chapter 3

Fourier Transform Spectroscopy as a Longitudinal Diagnostic Technique

Following the previous chapters introduction of coherent synchrotron radiation, this chapter will discuss the theory of measuring the coherent spectrum using a frequency domain technique, for the purpose of measuring the bunch's longitudinal profile. A description of Fourier transform spectroscopy is given, followed by the principles of interferometry, and the methodology in calculating the corresponding spectrum. Finally, reconstruction of the longitudinal profile from the Kramers Kronig technique is outlined.

3.1 Principles of Fourier Transform Spectroscopy using a Michelson Interferometer

Fourier transform spectroscopy is a measurement technique for determining the coherent spectrum emitted by a source. The spectrum is obtained from time domain measurements of either spatial or temporal interference, after which the spectrum is obtained by a Fourier transform. This method has been shown to successfully measure coherent spectrum from short bunches, such as the scheme in [83] at the VUV-FEL at DESY which employed a Martin-Puplett interferometer.

A more basic version of a two beam interference system is the well known Michelson interferometer. A typical Michelson interferometer configuration is shown in figure 3.1. For the experiment undertaken in this thesis, the source is the CSR from a dipole. A beamsplitter then divides the incident beam into two components. The first of these is

reflected towards a fixed mirror, with the second transmitted towards a movable mirror. The two beams reflect off their respective mirrors back to the splitter, whereupon both beams are once again divided into two components. A component from each interferometer arm recombines at the splitter and propagates towards a detector, however the other components recombine and propagate back towards the source and are undetected.

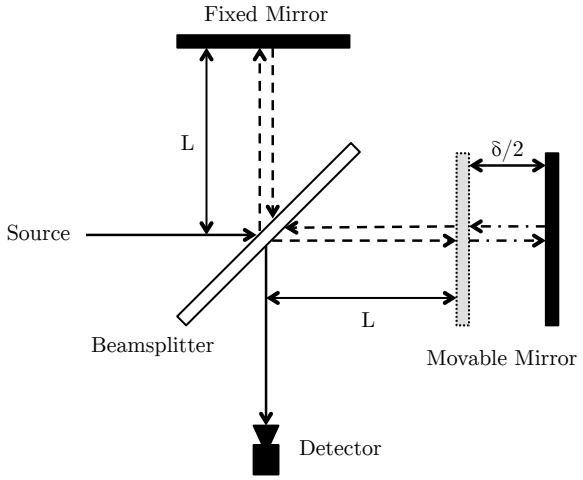

Figure 3.1: Typical setup of a Michelson Interferometer

To describe the system mathematically, we must first consider the source to be an incident monochromatic electromagnetic wave, which can be written as

$$E(\omega, z) = E_0(\omega)e^{i(\frac{\omega}{c}z)}, \tag{3.1}$$

where $E_0(\omega)$ is the amplitude of the wave, ω is the wave's angular frequency, and z is the position along the optical path. In the case of the Michelson interferometer, assuming the beamsplitter has a transmission T and a reflection R, then an incident beam is split into two beams, with the optical path difference δ resulting in one beam having an effective phase shift. The two beams can be written as,

$$E_1(\omega, z) = T \cdot RE_0(\omega)e^{i\frac{\omega}{c}z}, \tag{3.2}$$

$$E_2(\omega, z) = R \cdot TE_0(\omega)e^{i\frac{\omega}{c}(z-\delta)}. \tag{3.3}$$

After the recombination at the splitter, the resulting wave is simply written as the sum of the two waves,

$$\begin{aligned} E_r(\omega, z) &= RT\left[E_0(\omega)e^{i\frac{\omega}{c}z} + E_0(\omega)e^{i\frac{\omega}{c}(z-\delta)}\right] \\ &= RTE_0(\omega)e^{i\frac{\omega}{c}z}\left(1 + e^{-i\frac{\omega}{c}\delta}\right). \end{aligned} \tag{3.4}$$

When at the point of zero path difference, then equation 3.4 reduces to a fraction of the equation for the initial incident beam, 3.1, courtesy only of the transmission and reflection of the splitter. The intensity of the beam is calculated from $I = c\epsilon_0|E_r(\omega, z)|^2$ as follows

$$\begin{aligned} I(\omega, \delta) &= |R|^2|T|^2 c\epsilon_0 E_r^*(\omega, z)E_r(\omega, z) \\ &= c\epsilon_0|R|^2|T|^2\left(E_0(\omega)e^{-i\frac{\omega}{c}z}\left(1 + e^{i\frac{\omega}{c}\delta}\right)\right)\left(E_0(\omega)e^{i\frac{\omega}{c}z}\left(1 + e^{-i\frac{\omega}{c}\delta}\right)\right) \\ &= c\epsilon_0|R|^2|T|^2E_0^2(\omega)\left(1 + e^{i\frac{\omega}{c}\delta}\right)\left(1 + e^{-i\frac{\omega}{c}\delta}\right) \\ &= 2c\epsilon_0|R|^2|T|^2E_0^2(\omega)\left(1 + \cos\left(\frac{\omega}{c}\delta\right)\right). \end{aligned} \tag{3.5}$$

It is important to note that this expression no longer contains the phase of the incident beam, only the phase difference as a result of the path difference. Any measurement of the intensity will therefore be a recording of the beam's amplitude only. Whilst the above expression tells us the intensity for the superposition of two monochromatic waves, the coherent synchrotron radiation spectrum is shown in section 2.2 to be polychromatic. To measure this spectrum, we must integrate equation 3.5 over all frequencies:

$$\begin{aligned} I(\delta) &= \int_0^\infty 2c\epsilon_0|R|^2|T|^2E_0^2(\omega)\left(1 + \cos\left(\frac{\omega}{c}\delta\right)\right)d\omega \\ &= \int_0^\infty 2c\epsilon_0|R|^2|T|^2E_0^2(\omega)d\omega + \int_0^\infty 2c\epsilon_0|R|^2|T|^2E_0^2(\omega)\cos\left(\frac{\omega}{c}\delta\right)d\omega. \end{aligned} \tag{3.6}$$

For the case of no path difference (i.e. $\delta = 0$), all wavelengths interfere constructively and equation 3.6 reduces to 2 times its first term,

$$I(0) = 2\int_0^\infty |R|^2|T|^2 2c\epsilon_0 E_0^2(\omega)d\omega. \tag{3.7}$$

For the case of $\delta = \infty$, the cosine term varies rapidly and thus averages to 0, therefore $I(\infty) = \frac{I(0)}{2}$. Substituting this and equation 3.7 into equation 3.5 then gives us an expression for the interferogram

$$I(\delta) - \frac{1}{2}I(0) = \int_0^\infty |R|^2|T|^2 4c\epsilon_0 E_0(\omega)\cos\Big(\frac{\omega}{c}\delta\Big)d\omega. \tag{3.8}$$

Defining the spectrum to be $B(\omega) = |R|^2|T|^2 4c\epsilon_0 E_0^2(\omega)$, then equation 3.8 becomes one of a Fourier cosine transform pair:

$$I(\delta) - \frac{1}{2}I(0) = \int_0^\infty B(\omega)\cos\Big(\frac{\omega}{c}\delta\Big)d\omega, \tag{3.9}$$

$$B(\omega) = \int_0^\infty \Big[I(\delta) - \frac{1}{2}I(0)\Big]\cos\Big(\frac{\omega}{c}\delta\Big)d\delta. \tag{3.10}$$

Equation 3.10 shows us that the emitted spectrum can be calculated by a Fourier transform of a known interference pattern as a function of optical path difference.

3.2 The Interferogram and Corresponding Spectra

To successfully measure an interferogram, we must consider the physical limitations of the Michelson interferometer system. In any practical scenario, the spectrum $B(\omega)$ will be affected by many components of the measurement system, such as mirror reflection properties, variations in beamsplitter reflection and transmission with frequency, atmospheric absorption, detector response etc. These effects will be discussed in chapter 4 either in general or when the specific components in the system are introduced. For now, we shall only introduce some of the detector effects. Realistically, no system is able to measure the spectrum over all frequencies, therefore finite limits should be used based upon the expected spectral content, the frequency response of the detector, and the resolution and extent of any measurements.

When recording the interferogram, the intensity must be sampled at discrete positions of the movable mirror. Sampling can be limited to a smaller region around the point of zero path difference as the photon pulse is of finite length. The frequency resolution is

twice the time of the longest optical path, τ_{max}:

$$\Delta\omega = \frac{2\pi}{2\tau_{max}} \tag{3.11}$$

The highest measurable frequency is the reciprocal of twice the interferogram sampling rate (i.e. four times the absolute mirror position resolution), and can be written as:

$$\omega_{max} = \frac{2\pi}{2\Delta\tau} \tag{3.12}$$

Therefore for an example of a mirror measuring incrementally in steps of $\Delta\tau = 0.1\,\text{mm}$, the resolution in path difference is 0.2 mm, therefore the highest resolvable frequency is 750 GHz.

As mentioned in chapter 1, a quasi-optical detector is available for use in measuring these coherent spectral emissions, discussed further in section 4.5. The detector operates between 100 and 1000 GHz, however it may be responsive beyond its stated limits. As such, the lower limit of the integration in equation 3.8 will be the theoretical beam-pipe cutoff frequency from equation 2.33. At this stage, it should be noted that Schottky barrier diode detectors typically do not exhibit a flat response across their stated frequency band, the response of the detector is actually a function of frequency. This will therefore affect any spectral measurement. As the detector response with frequency is not known, we shall assume for the purposes of this proof of principle that the response is flat.

For the upper limit of the integral, we must consider the extent of the coherent spectrum. From the coherent synchrotron radiation spectrum described in section 2.2, the generation of bunches shorter than 0.5 mm would begin to emit coherent radiation beyond 1 THz. The power of the shorter wavelengths, however, is up to the number of particles times smaller than the peak power as shown in figure 2.5. As the quasi-optical detector cannot operate over such a large dynamic range, we can justifiably set the limit to the be the 1000 GHz limit of the detector.

In equation 3.8, a symmetric interferogram is obtained by a Fourier cosine transform of the amplitude of the initial pulse. The form of the interference pattern is highly dependant on the initial wave amplitude, $E_0(f)$. Figure 3.2 shows two simulated interferograms, one with an amplitude set to be the Fourier transform of the Gaussian longitudinal charge distribution in equation 2.15, and the other with an amplitude of unity for all frequencies.

It was assumed that the reflection and transmission were $R = \frac{1}{2}$ and $T = \frac{1}{2}$ respectively.

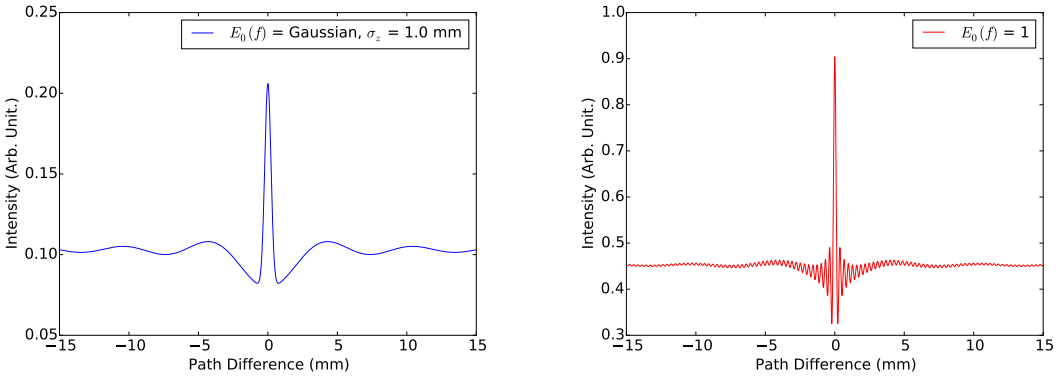

(a) (b)

Figure 3.2: The interferogram of a polychromatic source between 50 and 1000 GHz for a Gaussian longitudinal charge distribution (left), and for unity for all frequencies (right).

For the unity pattern, the interference from the shorter wavelengths is more evident as seen by the rapid oscillations due to their spectral power relative to the Gaussian spectrum. This higher intensity also contributes to a larger central peak as all frequencies constructively interfere as the point of zero path difference. The final amplitude spectrum is obtained from the Fourier transform of the patterns in figure 3.2, the results of which are displayed in figure 3.3 along with the form factor as calculated by equation 2.13.

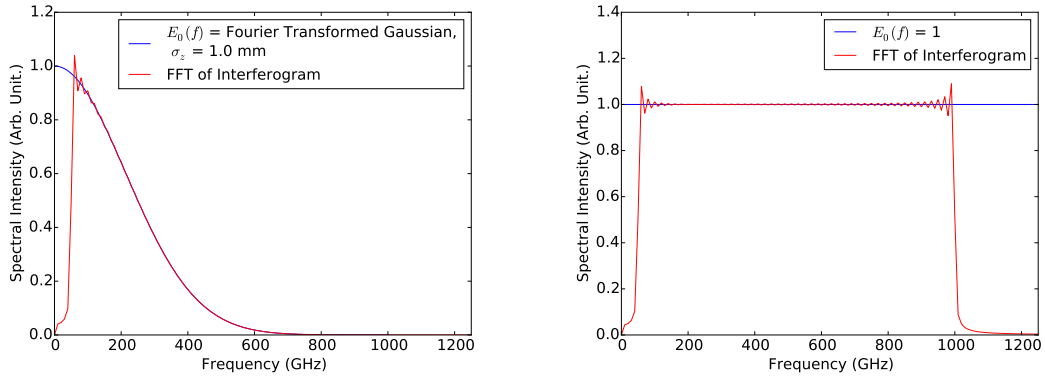

(a) (b)

Figure 3.3: The amplitude spectrum obtained by Fourier Transform of the interferograms in figure 3.2 for a Gaussian bunch (left), and for unity for all frequencies (right).

The spectra as calculated from the interferograms are identical to that of the form factor within the integral limits, thus showing that the Michelson interferometer is suitable for measuring the coherent amplitude spectrum.

3.3 Kramers-Kronig Analysis

Thus far, the interferometric calculations have only yielded the emitted spectra within specified limits. To attempt a reconstruction of the longitudinal bunch profile, a bunch form factor must be extracted from the measured spectrum. If the measurement covers a sufficient spectral range, the bunch profile can be reconstructed using the Kramers-Kronig relation, which when applied to the form factor, will find the minimal phase, after which the bunch distribution can then be reconstructed by taking the Fourier transform of the form factor amplitude [84, 85]. It is particularly useful for cases where the bunch distribution is asymmetric. The relation itself is a mathematical technique used to relate the real and imaginary components of a complex function.

As shown previously in equation 2.13, the bunch's form factor $F(\omega)$ is the modulus squared of the Fourier transform of the longitudinal charge distribution, $s(z)$. The distribution cannot be simply obtained by calculating the inverse Fourier transform of the form factor, as the recorded spectra only contains information on the spectral amplitude, and not the phase. As the Kramers-Kronig relation connects real and imaginary components, the form factor can be written as a complex function that is the product of the amplitude and phase terms,

$$\widehat{F}(\omega) = \int_0^\infty s(z) e^{\left(i\frac{\omega}{c}z\right)} dz \equiv \sqrt{F(\omega)} e^{(i\varphi(\omega))}. \tag{3.13}$$

Note that the product of the complex form factor and its complex conjugate yields the original real form factor:

$$\widehat{F}\widehat{F}^* = \sqrt{F(\omega)} e^{(i\varphi(\omega))} \sqrt{F(\omega)} e^{(-i\varphi(\omega))} = F(\omega). \tag{3.14}$$

By knowing the form factor over all frequencies, then the minimal phase term over all frequencies can be calculated using equation 3.15 [84].

$$\varphi_m(\omega) = -\frac{2\omega}{\pi} \int_0^\infty \frac{ln\left(\sqrt{F(x)}/\sqrt{F(\omega)}\right)}{x^2 - \omega^2} dx. \tag{3.15}$$

With the minimum phase calculated, the longitudinal charge distribution can then be calculated by taking the inverse Fourier transform of equation 3.13, the result of which is shown in equation 3.16.

$$s(z) = \frac{1}{\pi c}\int_0^\infty \sqrt{F(\omega)}\cos\left(\varphi_m(\omega) - \frac{\omega}{c}z\right)d\omega. \tag{3.16}$$

Only the cosine term appears in equation 3.16 as the charge distribution is a real quantity.

Up to this point, it has been assumed the form factor is known over all frequencies. In practice, however, any experiment will only measure part of the spectrum, thus only a part of the form factor will be known. If the known region covers a significant portion of the coherent spectrum, it is possible to extrapolate the spectrum both to 0 and to higher frequencies. An additional consequence of any experiment is that the measured spectrum will be discrete, and the recording of a continuous spectrum is impractical. Thus the above equations must be discretised to make them applicable for calculating the reconstructed bunch distribution.

Let's suppose that a spectrum is measured in the frequency range $\omega_{n_0} \to \omega_N$, which is a subset of a larger frequency range, $\omega_0 \to \omega_M$. This larger frequency range should cover all features of the coherent spectrum. To successfully apply a fit to the spectrum and obtain a form factor, the measured data must be interpolated, and subsequently extrapolated to cover the unknown regions of the spectrum, $\omega_0 \to \omega_{n_0}$, and $\omega_N \to \omega_M$.

To interpolate the measured region, the function shown in equation 3.17 is applied [86], where $F(\omega)$ is the form factor data, σ is a smoothing parameter, ω_n are the frequency points where the form factor data is measured, and ω_m is the frequency point in the interpolation.

$$F_{int}(\omega_m) = \frac{\sum_{n=n_0}^{N} F(\omega_n)e^{\left(-\frac{(\omega_n-\omega_m)^2}{2\sigma^2}\right)}}{\sum_{n=n_0}^{N} e^{\left(-\frac{(\omega_n-\omega_m)^2}{2\sigma^2}\right)}}. \tag{3.17}$$

The smoothing parameter was chosen to be $\sigma = \frac{\Delta\omega_n}{3} = \frac{\omega_n-\omega_{n-1}}{3}$, which has been shown to be effective in a similar analysis [86]. For the extrapolation, we have to consider the cases for low and high frequencies separately. For the high frequencies, the detector bandwidth should be sufficient so to as not require extrapolation. For the small frequencies, the extrapolation should match the data at ω_{n_0}, and should tend to unity as the frequency tends to 0. Previous literature has suggested an extrapolation of the following form [87].

$$F_{small}(\omega_m) = e^{(-\alpha\omega_m^2)}. \tag{3.18}$$

Therefore, the function that will be fitted to the data is:

$$F_{fit}(\omega_m) = \begin{cases} F_{small}(\omega_m) & m < n_0 \\ F_{int}(\omega_m) & n_0 \leq m \leq N. \end{cases} \tag{3.19}$$

With the form factor now known over the coherent spectrum, the minimal phase can be written in its discretised form as [88]

$$\varphi(\omega_\tau) = -\frac{2\omega_\tau}{\pi} \sum_{m=0}^{M} \frac{ln\left(\sqrt{F_{fit}(\omega_m)}/\sqrt{F_{fit}(\omega_\tau)}\right)}{\omega_m^2 - \omega_\tau^2}. \tag{3.20}$$

As there is a discontinuity in the denominator of equation 3.20 when $\omega_m = \omega_\tau$, then the summation variable must be shifted with respect to ω_m; as such it was chosen that the shift is equal to $\Delta\omega_m/2$.

The final step is the bunch charge distribution reconstruction, which in its discrete form can be written as [88]:

$$\rho(z) = \frac{1}{\pi} = \sum_{\tau=0}^{T} \sqrt{F_{fit}(\omega_\tau)} \cos\left(\varphi(\omega_\tau) - z\omega_\tau\right) \Delta\omega_\tau. \tag{3.21}$$

To verify the discretisation of the relation, let's consider an asymmetric longitudinal charge distribution, for example a sum of two Gaussians of different amplitudes,

$$s(z) = \frac{1}{4\sqrt{2\pi}\sigma_1} e^{\left(-\frac{z^2}{2\sigma_1^2}\right)} + \frac{3}{4\sqrt{2\pi}\sigma_2} e^{\left(-\frac{(z-z_0)^2}{2\sigma_2^2}\right)}, \tag{3.22}$$

where arbitrarily, $z_0 = 2.0$ mm, $\sigma_1 = 0.5$ mm, and $\sigma_2 = 0.75$ mm. The corresponding form factor can be written as [88]

$$F(\omega) = \frac{1}{16}\left(e^{(-\sigma_1^2\omega^2)} + 9e^{(-\sigma_2^2\omega^2)} + 6e^{\left(-\frac{\omega^2(\sigma_1^2+\sigma_2^2)}{2}\right)}\right). \tag{3.23}$$

The longitudinal distribution from equation 3.22 and its corresponding form factor from equation 3.23 are shown in figure 3.4. Whilst a simple Gaussian distribution will produce a half Gaussian form factor (a Gaussian centred at zero, but only valid for positive frequencies), the introduction of the second Gaussian as a summation in the distribution has an impact as seen by the appearance of higher frequencies in the form factor.

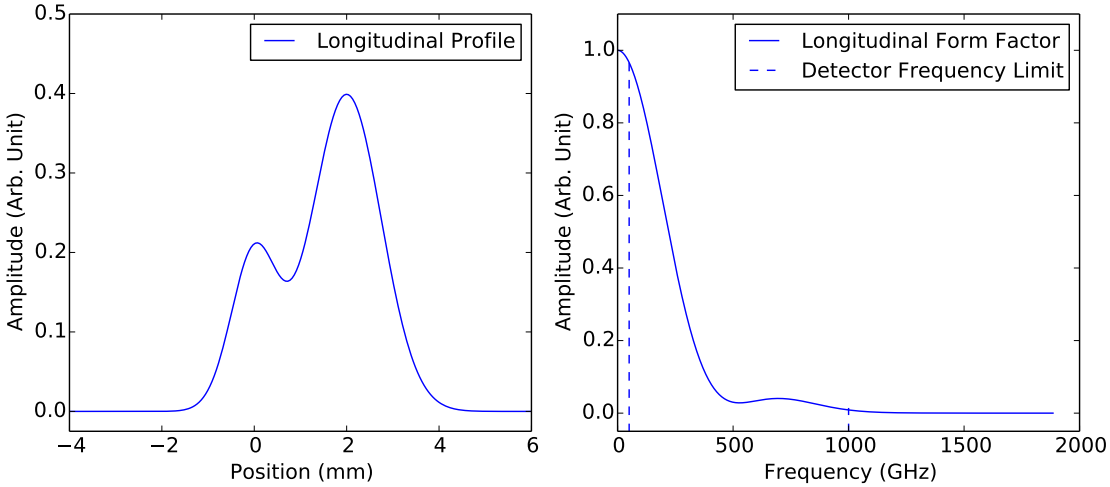

Figure 3.4: The longitudinal charge distribution (left), and the corresponding form factor (right).

As it is unfeasible to measure the form factor over all frequencies, included with the form factor plot are example frequency limits for the quasi-optical detector. The limits of this detector are sufficient to measure the spectrum in the region where these high frequency effects may occur, however as this example is for a specific case, care must be taken with the experimental data with any potential extrapolation. As the full form factor is not covered by the bandwidth of the detector, extrapolation to both high and low frequencies is necessary. As such, figure 3.5 shows the resulting form factor from the interpolation and extrapolation process using equation 3.18, along with the calculated

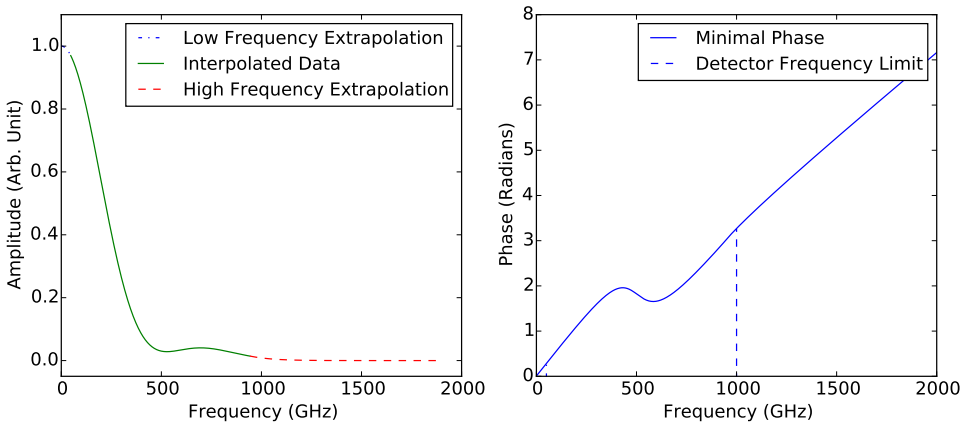

Figure 3.5: The form factor (left) interpolated over the data range and extrapolated to both high and low frequencies, and the calculated minimal phase (right).

minimal phase from the form factor. Once again, the detector limits are shown on the phase plot.

With the phase calculated, the bunch profile can be reconstructed, as shown in figure 3.6, along with the original bunch profile. Whilst the calculated and original distributions agree well, there are clear mismatches from either the incomplete measured form factor, thus suggesting that the reconstructed profile is highly sensitive to the extrapolation procedure; or that we have only calculated the minimum phase and that larger phases have an effect that are not accounted for; or a combination of the two effects.

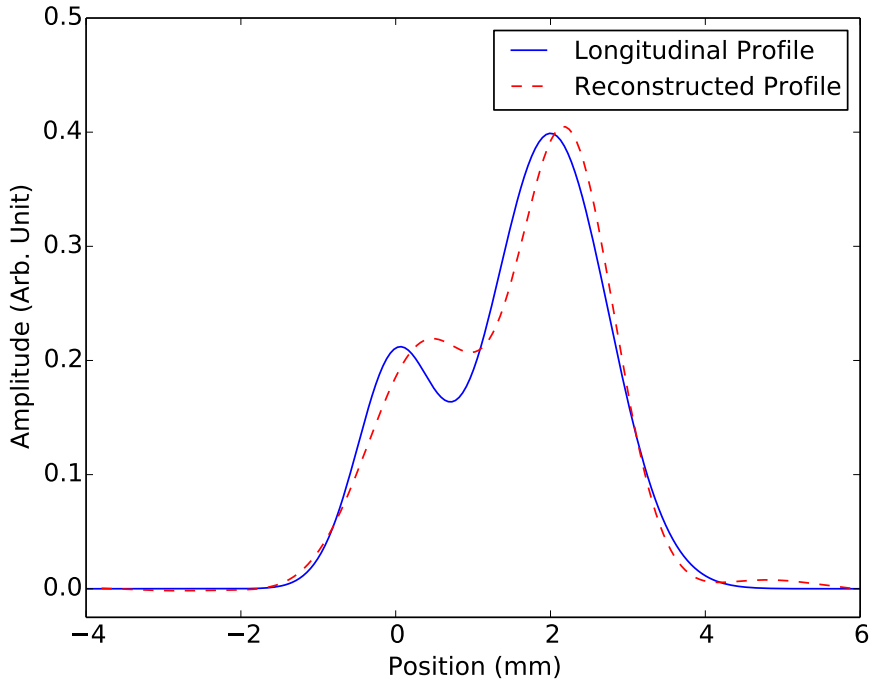

Figure 3.6: The reconstructed longitudinal profile and original profile for comparison.

3.4 Summary

It has been shown in this chapter that reconstruction of the longitudinal charge distribution of an electron bunch is possible from measurements of the bunch's coherent emissions using Fourier transform spectroscopy. An application of the technique in the form of an Michelson Interferometer can measure the interference of an incident beam, from which the coherent amplitude spectrum can be calculated via Fourier transform. In doing so, however, the phase information of the beam is lost. The longitudinal charge distribution is

calculated using the Kramers-Kronig technique by calculating a minimum phase and fitting a continuous function form factor to a known spectrum. Although difficult to measure in its entirety, a significant portion of the coherent spectrum can be measured using a single quasi-optical detector, with the remaining unknown spectral regions obtained by extrapolation. A discretisation of the Kramers-Kronig technique has yielded the possibility of computationally reconstructing asymmetric charge distributions, however, they remain sensitive to the extrapolation procedure.

Chapter 4

Experimental Setup

As the principles of Fourier transform spectroscopy using a Michelson interferometer are now known, this chapter will explain its physical application by the experimental setup developed for this thesis. This includes an overview of Diamond Light Source along with existing diagnostic instrumentation, the dedicated mm-wave viewport and its characterisation system plus optical transfer line, and the interferometer and its key components including the detectors. Finally the data acquisition system and experimental methodology are described, followed by viewport characterisation measurements and the corresponding systematic effects on any measureable spectra.

4.1 Diamond Light Source

Diamond Light Source is a 3rd generation synchrotron machine, providing high intensity synchrotron radiation to 22 operational beamlines as of 2014 [18], with more under construction. The main storage ring is a 561.6 metre circumference, 24 cell double bend achromat lattice. The whole ring consists of 48 dipoles (with a bending radius of 7.16 m), 248 quadrupoles and 168 sextupoles, along with 22 straight sections for insertion devices, 1 straight for injection, and 1 straight for the RF system [82, 89]. There are several insertion devices (4 wigglers and 23 undulators at the time of writing) in the ring to provide the high brightness radiation for beamline users. There are currently two superconducting RF cavities in the storage ring, both of which operate at 499.655 MHz, up to voltages of around 2 MV each. The revolution frequency of Diamond Light Source is 533.820 kHz, resulting therefore in 936 RF buckets with a bunch spacing of $\sim$ 2 ns.

4.1.1 Diamond Storage Ring Operation

As previously mentioned, Diamond can operate in different modes, notably operation with a low momentum compaction factor, α. Consequently, the beam and lattice parameters vary significantly depending on the mode of operation. The operation of any synchrotron light source is typically chosen as to be optimal for users, providing as large a brilliance as possible. Of significant importance to the brilliance, as defined in section 1.2.1, is the photon flux, $F = \frac{d^2N}{d\theta d\psi}$ which is defined in equation A.13 (appendix A). The photon flux is directly proportional to the number of electrons passing per second, therefore a large beam current is additionally desired. This is primarily achieved by populating multiple RF buckets.

The storage ring at Diamond Light Source has the ability to operate in numerous fill patterns, with typical standard operation running with 900 RF buckets occupied. The storage ring operates at around 300 mA, corresponding to around 3×10^9 particles per bunch. Limitations of the RF system prevent a greater current being accelerated. Other fill patterns include hybrid mode, where 686 bunches are accompanied with a single high charge bunch in a bucket in the empty region of the fill pattern. It can also operate with a single bunch only, used primarily for diagnostics where single bunch monitoring can be advantageous for data acquisition rates and ensured monitoring of the same bunch, (also eliminating any bunch-bunch interaction effects).

Low alpha operation typically runs with other fill patterns, normally 100 or 200 bunches, depending on which low alpha lattice is being used. The implementation of two low alpha lattices at Diamond arises from the need of the user community. Initially, the development of the low alpha lattice was for the generation of short pulses, the shortened bunch length providing that solution. Beyond this, the need grew for THz radiation in one of Diamond's beam lines which specialises in infrared spectroscopy. The second low alpha mode further reduces α resulting in a shorter bunch length (despite the decrease in synchrotron frequency f_{sync}) and thus extending the CSR spectrum to shorter wavelengths. Many of the design parameters of the two low alpha lattice are the same, the key difference being the reduction in α_1. This and some of the beam and lattice parameters are shown in table 4.1 for three modes of operation; standard mode and two low alpha modes.

Whilst a low emittance is achieved for the low alpha modes, the stored current is significantly lower for stable operation, mainly limited by the onset of the microbunching instability (at different threshold currents). The current in a single bunch is typically tens

Mode of Operation	**Standard**	**Low α (Short Pulse)**	**Low α (THz)**
ϵ_x (nm rad)	2.7	4.4	3.9
α_1	1.7×10^{-4}	-1×10^{-5}	-4.5×10^{-6}
α_2	1.9×10^{-3}	-2.2×10^{-5}	-2.3×10^{-5}
Q_x/Q_y	27.22 / 12.36	29.39 / 8.284	29.39 / 8.284
ξ_x/ξ_y	-85 / -39	-62 / -48	-62 / -48
β_x/β_y (at ID) (m)	4.7 / 1.5	1.12 / 5.64	1.11 / 5.64
D_x (Max) (m)	0.35	0.28	0.029
σ_z (Zero Current) (ps)	9.4	2.4	1.63
$f_{sync.}$ (Hz)	2.6×10^3	632	425

Table 4.1: Lattice and beam parameters for standard operation, and for two low alpha operations [52, 54, 90–94].

of μA [52], 2 orders of magnitude lower that that of the standard operation. For low alpha user operation however, this bunch current is generally kept above the threshold in the quasi-periodic regime but before the bursting region as the beam line's data quality is not appreciably affected [54]. For the low alpha THz lattice, the stored current is limited to 10 mA over all bunches due to an increase in transverse motion upon injection which trips an orbit interlock.

During the early experiments, the short pulse low alpha mode was more readily available. For consistency, all experiments which investigated the instability during dedicated beam time used the same mode of operation of $\alpha_1 = -1 \times 10^{-5}$. The THz mode was described here because it was used when it became available to users. Parasitical measurements were taken for the purpose of characterising the viewport and moving the mechanical optical components for alignment, as these tasks did not depend on the mode of operation.

In addition to the beam parameters, figure 4.1(a) shows the super period of 4 cells of the lattice for the standard optics mode. The β_x and β_y values in table 4.1 correspond to the minima in the straight sections at $s \approx 23, 47$ and 70 m. For comparison, the super period of 4 cells of the short pulse low alpha lattice is shown in figure 4.1(b).

The immediately obvious difference between the two lattice in figures 4.1(a) and 4.1(b) is the amplitude of the three functions. Although difficult to distinguish, the dispersion can be seen to cross from positive to negative in the dipoles. The implementation of the low alpha lattice is discussed in section 2.4, with the emittance being shown to be related to the dispersion (via the radiation integrals from appendix B) in section 2.4.

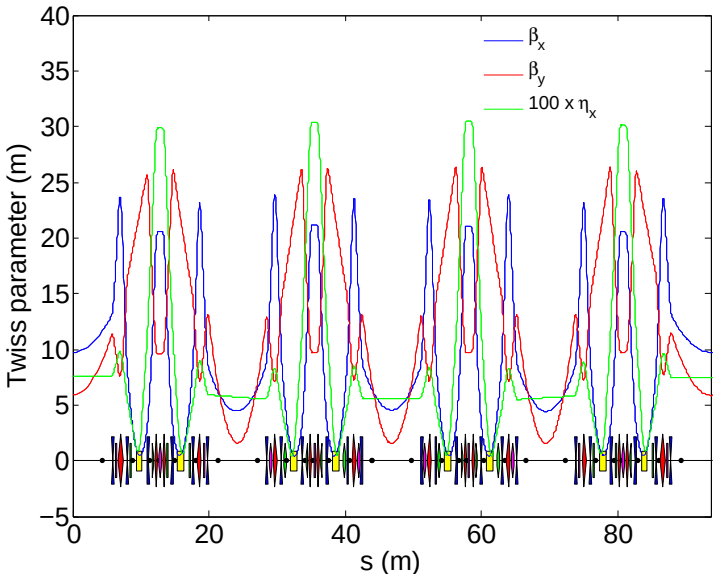

(a)

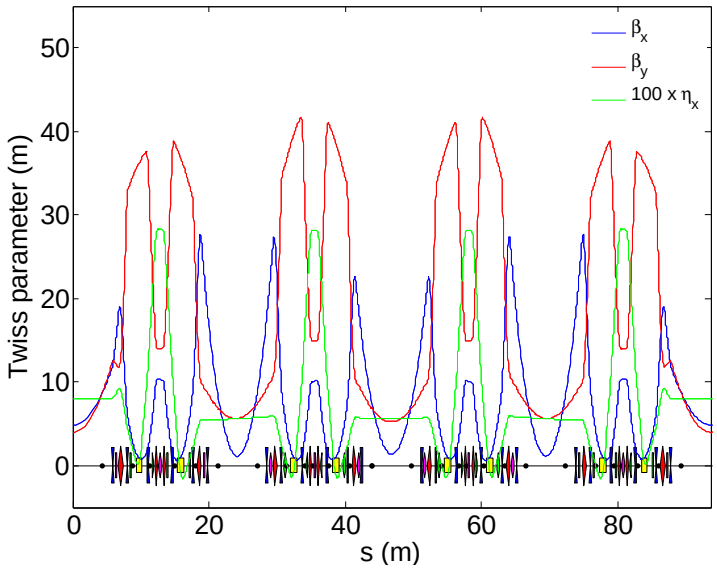

(b)

Figure 4.1: Optical functions of four cells of the storage ring lattice for standard operation (a), and for low alpha ($\alpha_1 = -1 \times 10^{-5}$) operation (b) at Diamond Light Source [95].

4.1.2 Instrumentation

During operation, various diagnostic apparatus are needed both to provide beam measurements, but also to acts as part of feedback systems for maintaining the stability of the beam below the microbunching threshold. Any diagnostics within the storage ring

are connected to instrumentation racks in the Control Instrumentation Area (CIA) for that cell of the ring, which can be remotely accessed from the control room. To ensure any experimental observations are or can be correlated to a change in environment or beam conditions, several parameters are recorded during every experiment. Here, we shall briefly describe some of the instrumentation used for recording beam parameters.

As the emittance is the most commonly used factor for comparing synchrotron light source facilities, its measurement must be as precise as possible. To measure the emittance, two x-ray pinhole cameras are employed at Diamond that measure the beam size, $\sigma_{x,y}$ [96,97]. By measuring the beam size at points of known betatron amplitude and dispersion, ($\beta_{x,y}$ and $D_{x,y}$ respectively), the horizontal and vertical emittances (ϵ_x and ϵ_y) and energy spread (σ_E) can be calculated according to [97],

$$\sigma_{x,y}^2 = \beta_{x,y}\epsilon_{x,y} + (D_{x,y}\sigma_E)^2. \tag{4.1}$$

For measurements of the beam current, two techniques are used; electron Beam Position Monitors (BPM) and DC Current Transformers (DCCT). 168 BPM are installed around the storage ring at Diamond, in addition to several others in the booster ring and injection lines [98]. The BPMs have multiple purposes, the primary function being to measure the position of the beam, however, the beam current can be additionally calculated. The BPM itself is an in-vacuum button block with 4 electrodes around the beam. The signal from each button is fed to a BPM processor, whereupon the position and current are calculated, however the current is calibrated against the solitary DCCT current monitor in the storage ring [98]. Whilst the BPMs have lower noise and are therefore sensitive to lower beam currents, they are less reliable in terms of absolute numbers [82], hence why the more reliable DCCT is used for calibration. Two of the BPMs are also configured to record the amplitude and phase of the voltages in the RF cavities [99], in addition to a probe in each RF cavity.

The measurement of the fill pattern is another useful parameter to be recorded, to ensure that post experimental analysis normalises to the correct number of occupied RF buckets. Typical measured fill patterns for nominal low-alpha operation and a single bunch in standard optics are shown in figure 4.2. The bucket numbers which are populated can be selected during experiments. The ratio between populated / unpopulated buckets that Diamond requires is $10^6 : 1$. For the measurement of this bunch purity, Diamond uses a time-correlated single photon counting method [100]. As environmental factors have the

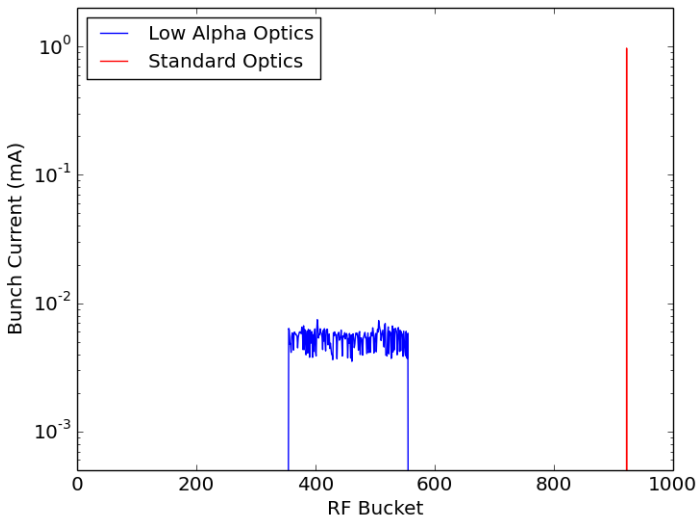

Figure 4.2: Typical fill pattern for nominal low alpha conditions and a single bunch in standard optics.

potential to impact upon experiments, the air temperature, pressure and relative humidity were additionally recorded.

4.1.2.1 Streak Camera

Longitudinal diagnostics for measuring the bunch lengths at Diamond are performed by a streak camera [90, 101]. The synchrotron radiation from a bending magnet is spectrally filtered by optics in the transfer line such that only the visible region of the spectrum remains (from 200 to 800 nm). The principle of operation of the streak camera is discussed in section 1.5.1.1.

The streak camera at Diamond is from Optronis GmbH. The two pairs of sweep electrodes can be separated into a 'slow' and 'fast' sweep. One pair corresponds to the fast sweep from which the bunch distribution data can be measured. It is quoted to have a resolution of 2 ps [101] although this figure originates from the manufacturers specifications where their definition of resolution is the Rayleigh Criterion. This resolution can only be achieved when a few electrons are deflected per incident photon pulse, therefore it requires several pulses stacked on top of one another to record a profile, and an accurate profile can only be achieved if the pulses are reproducible. The stacking effect comes from the slow sweep, which can operate between 660 ps/mm and 5ms/mm. This sweeps in a perpendicular direction to the fast sweep, such that each successive fast sweep is at a

different position on the CCD. The 660 ps/mm sweep speed corresponds to 8 fast sweeps per pixel row, thus appearing as a stack of 8 pulses.

The streak camera's resolution is ultimately a performance limit contributed to by many effects, such as the finite size of the beam spot, generation of a larger spot on the phosphor screen, further blur through the image intensifier and output optics etc [82]. Furthermore, higher intensity bunches also generate more electrons in the streak tube, whereupon space charge effects will also blur the image.

Given the difficultly in quantifying these effects, for the purpose of this thesis and maintaining consistency with streak camera measurements at Diamond, the best method of probing the resolution is to measure the Point Spread Function (PSF), which can be recorded by measuring a focused beam without a sweep [101]. The 'actual' bunch length, σ_z, can then be calculated from the recorded bunch length, $\sigma_{Meas.}$, and the width of the PSF, σ_{PSF}, from

$$\sigma_z = \sqrt{(\sigma^2_{Meas.} - \sigma^2_{PSF})}. \tag{4.2}$$

The short bunches produced from low alpha optics which can nominally be smaller than the streak camera resolution when incorporating all the aforementioned effects, are subsequently difficult to measure. The resolution also inhibits any measurements of substructure within the bunch. Despite the limitations of the streak camera, it can provide a useful comparison to any measurements from the setup described in subsequent sections.

4.1.2.2 Streak Camera Measurements

Streak camera images were recorded as a complimentary measurement to the results presented in section 5.4.2 for the low alpha, short pulse mode with 200 bunches over a range of bunch currents. Unfortunately during this experiment where streak camera data were obtained, a feedback problem during injection meant the beam would not inject higher than the 27 μA per bunch, which is somewhat frustratingly below the predicted microbunching instability threshold. The data can be used however, to ascertain the bunch profile for comparison to the interferometer measurements.

At each bunch current, 5 images were captured with the streak camera, with each image consisting of 1024 slow sweep scans. The left plot in figure 4.3 shows the r.m.s. bunch lengths for increasing bunch current. The values are taken from a Gaussian fit

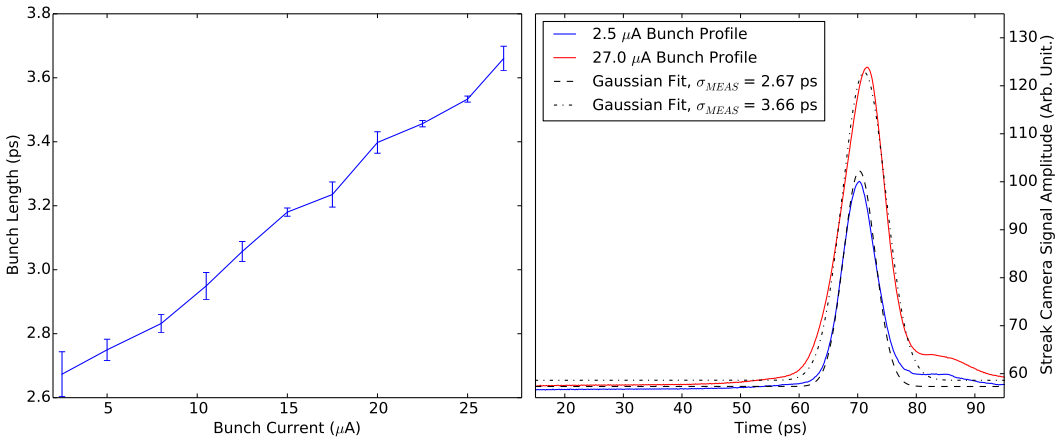

Figure 4.3: R.m.s. bunch length as a function of bunch current (left), and two example bunch profiles (right) from 200 bunches in low alpha operation.

to each of the 1024 slow sweep scans recorded in each streak camera image, with the average bunch length of the 5×1024 profiles being shown here. The errors are the r.m.s of the bunch length errors from each fit. The right plot in figure 4.3 contains two example profiles from lowest and highest bunch currents (2.5 μA and 27 μA respectively) with their corresponding Gaussian fits.

The bunch lengths are of similar magnitude to those observed in [102], including the behaviour of the bunch length with current, except for the small increase in bunch length at very low currents. The RF voltage is higher than the measurements in [102], therefore it is possible this effect may not appear until below 2.5 μA bunch current. Lower currents were not explored as at the time of measurement we were interested in the instability rather than low current bunch lengths.

The time domain profiles here from both bunch currents clearly indicate that they are of similar form to that of the sum of two Gaussians, with their form factors being the same type of distribution as suggested in section 3.3. The bunch length measurements from the fits only incorporate the larger of the two Gaussians, therefore any bunch length calculated from fitting will be an underestimate of the true bunch length.

4.2 Instability Characterisation Viewports

The initial instability detection experiments were conducted at a shared diagnostics viewport, with the radiation source provided from bunches propagating through bending magnet B01. Small wavelength emissions are removed from the beam line, leaving only wave-

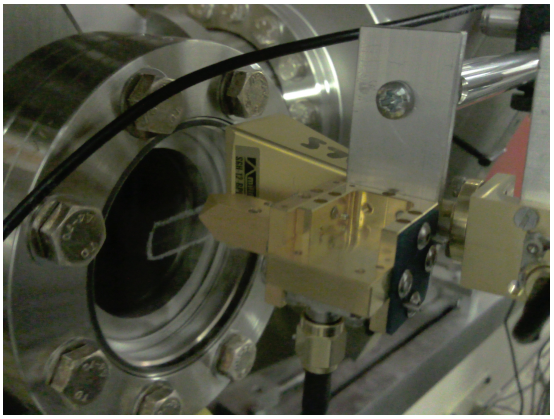

Figure 4.4: Two Schottky barrier diode detectors at a diagnostics viewport for preliminary instability detection experiments.

lengths of visible light and longer, which propagate through a fused silica viewport. As the viewport is primarily for the purpose of optical diagnostics, the two detectors were mounted in front of the window as seen in figure 4.4, positioned so as to not affect the optical diagnostics. One amplified detector operated between 60-90 GHz, the other unamplified between 220-330 GHz. The detectors, discussed further in section 4.5, were connected to a signal analyser, discussed further with the amplifiers and other DAQ hardware in section 4.6. No additional apparatus were installed at this stage of the microbunching instability investigation.

4.2.1 Diagnostic Viewport for Instability Detection

The viewport dedicated to mm-wave diagnostics is approximately 4 m downstream of bending magnet B06. This section will describe the beamline used in the experiments, comprising of components that are required before the measurement systems. The first key component is the viewport, shown in figure 4.5(a). The in-vacuum port transports the emitted radiation into a plane that is lower but parallel to the beam pipe plane by a periscope, a diagram of which is shown in figure 4.5(b). Firstly, a water cooled copper mirror reflects the mm and sub-mm wavelengths at an angle whilst simultaneously absorbing high intensity x-ray radiation. A second mirror then reflects the remaining mm wave radiation into the parallel plane. The path length from the dipole to the viewport is approximately 4 m.

Whilst severely reducing the flux of radiation in the x-ray region, radiation was still found to affect components during experimental testing. As a result, some of the sensitive

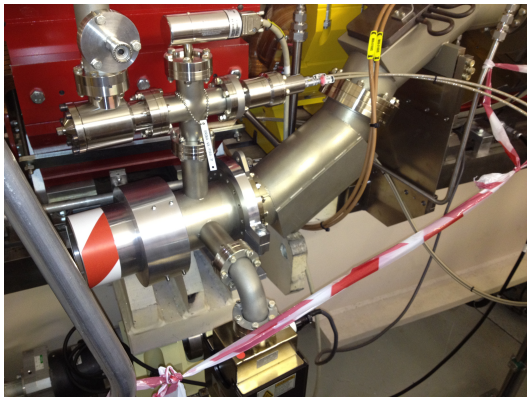

(a)

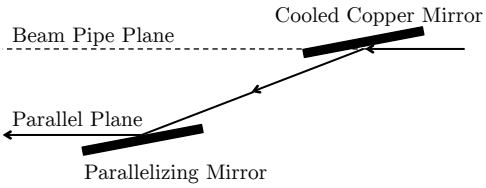

(b)

Figure 4.5: A photo of the dedicated mm-wave diagnostics viewport, with a diagram showing the in-vacuum mirror scheme used.

electronic components were surrounded in lead shielding to further reduce any potential ionising radiation. The vast amount of metallic components in both the experimental setup and the storage ring itself prevented any firm conclusions as to the origin of any scattered X-rays.

4.2.2 Viewport Window

The viewport window is an 89 mm diameter fused silica, zero length window from Torr Scientific Ltd [103]. The thickness of the window is specified as 6 mm, however, the specified tolerance results in an uncertainty in the exact thickness. Any interface between two media of different refractive indices will result in any incident electromagnetic wave being partially reflected from and partially transmitted into the medium, as shown in diagram 4.6 by vectors r_1 and t_1. For a material of finite thickness, any waves transmitted

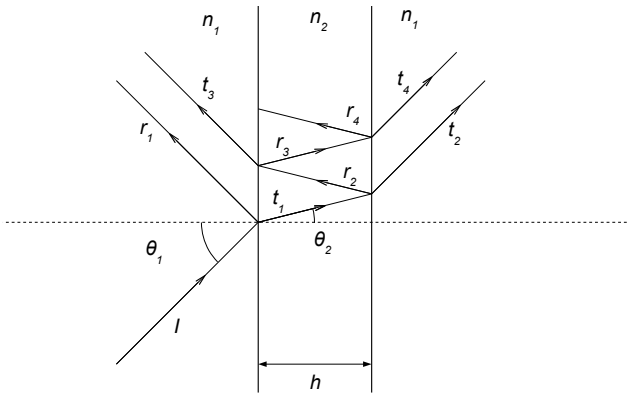

Figure 4.6: Diagram showing the reflection and transmission of an incident beam at a boundary between two media of different refractive indices.

at the boundary into the material will undergo another partial reflection and transmission at the second interface, labelled as r_2 and t_2. For certain wavelengths, the series of internal reflections will destructively interfere, resulting in an efficiency drop, of which the distance h between the two surfaces of the window is of great significance.

The reflectance and transmittance can be calculated from equations 4.3 and 4.4 respectively [104], where $\delta = 4\pi n_2 h\sigma \cos\theta_1$ and $A = exp(-Kh/\cos\theta_1)$, where n_2 is the refractive index of the material, h is the material thickness, $\sigma = \frac{1}{\lambda}$ is the wavenumber, K is the absorption coefficient, and θ_2 is the angle of refraction, which can be calculated from the angle of incidence via Snell's law: $\cos\theta_1 = n_2 \cos\theta_2$. As the viewport is under vacuum, the first refractive index $n_1 = 1$.

$$R_0 = \frac{r\left(1 + A^2 - 2A\cos\delta\right)}{(1 + r^2A^2 - 2rA\cos\delta)} \tag{4.3}$$

$$T_0 = \frac{A(1-r)^2}{(1 + r^2A^2 - 2rA\cos\delta)} \tag{4.4}$$

The reflection coefficients of the material, r, can be found using the Fresnel equations, which describe the cases where the electric field of the incident wave is either parallel or perpendicular to the plane of incidence, given by in equations 4.5 and 4.6 respectively.

$$r_\perp = \left| \frac{n_1\cos\theta_i - n_2\sqrt{1 - (\frac{n_1}{n_2}\sin\theta_i)^2}}{n_1\cos\theta_i - n_2\sqrt{1 - (\frac{n_1}{n_2}\sin\theta_i)^2}} \right|^2 \tag{4.5}$$

$$r_\parallel = \left| \frac{n_1\sqrt{1 - (\frac{n_1}{n_2}\sin\theta_i)^2} - n_2\cos\theta_i}{n_1\sqrt{1 - (\frac{n_1}{n_2}\sin\theta_i)^2} + n_2\cos\theta_i} \right|^2 \tag{4.6}$$

Figure 4.7 shows the calculated transmission coefficient for the fused silica window. The refractive index and absorption coefficient data were obtained from [105–107] with the refractive index typically being 1.95 in this region. In addition to the transmission coefficient, the plot includes the form factor for a 0.5 mm long Gaussian bunch for full transmission and window modulated transmission, showing that the silica window has a significant impact on any potential spectrum. Changing the window thickness (to within its tolerance) causes a noticeable change in periodicity, therefore the effect of the window on the spectrum must be fitted to the recorded data.

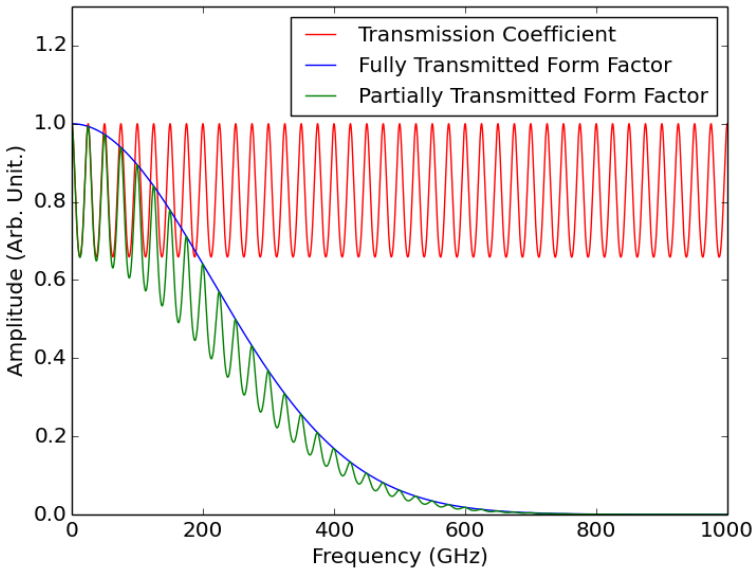

Figure 4.7: Transmission coefficient (red) of a 6 mm thick fused silica viewport at 0° angle of incidence, with a normalised theoretical form factor for a 0.5 mm long Gaussian electron bunch at both full (blue) and partial (green) transmission.

4.2.3 Modulation Chopper

Two different detectors were used in the interferometer at separate times, one of which was a pyroelectric detector. Further details of the detector can be found in section 4.5.1, however at this stage, it must be noted that operation of the pyroelectric detector required an external modulation of any radiation that may be detected. To provide the modulation, an optical chopper wheel (340 CD from Scitec Instruments) was installed, which provided control of the modulation frequency. Although the signal is naturally modulated as the revolution frequency, the pyroelectric detector requires a much smaller modulation frequency (of the order of 10 Hz). The chopper was connected to and controllable via a lock-in amplifier, as discussed in section 4.6.3. Severe vibrations were observed in the detection system during experiments that were from the chopper, therefore the modulation frequency was limited to $\lesssim$ 40 Hz.

4.2.4 High Frequency Filter

The large bandwidth of the pyroelectric detector allows it to detect mid-to-near infrared radiation produced from the bunch, however as the primary characteristic of the instability is the emission of wavelengths of the order of the bunch length, filtering was needed to

reduce the unwanted signal. A polystyrene sheet was inserted between the chopper and detecting systems to absorb the infra-red radiation whilst permitting mm-waves. Previous literature shows that polystyrene foam has a low refractive index of between 1.0 and 1.022 between 0.1 to 4 THz [108]. Additionally, polystyrene has an extinction coefficient of $< 1.5\ cm^{-1}$ throughout the same frequency range, the cause of which was attributed to scattering as opposed to direct absorption [108]. The use of polystyrene is therefore favourable to transmit THz waves with only small losses, whilst blocking higher frequency radiation.

4.2.5 Atmospheric Absorption

Any emission is naturally susceptible to the environmental conditions in the storage ring tunnel, and water in particular is known to affect THz frequencies by absorption. Figure 4.8(a) shows the absorption through 1 metre of air at standard atmospheric pressure, at 20°C and 50% relative humidity, with figure 4.8(b) showing the atmospheric transmission spectrum compared to the form factor from a 0.5 mm long Gaussian bunch.

The effect of absorption is small until $\sim$ 500 GHz, whereupon the transmission is significantly effected at certain frequencies. Any measured spectra exhibiting dips at these frequencies can be adjusted to take atmospheric absorption into account. It should be noted that whilst the displayed absorption spectrum is for specific atmospheric conditions, the environment in the storage ring can vary, particularly the relative humidity, however the change is sufficiently small so as to not significantly affect the absorption spectrum.

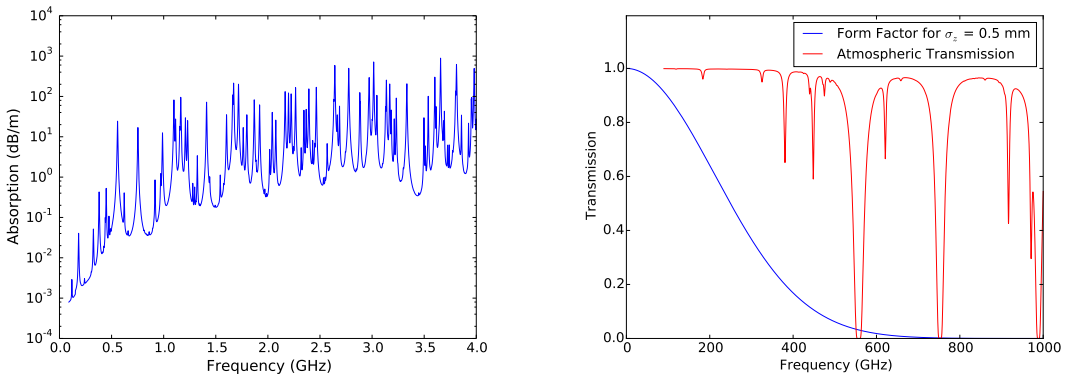

(a) (b)

Figure 4.8: Absorption and transmission of air over 1 m for standard atmospheric pressure at 20°C and 50% relative humidity.

Environmental systems ensure that the is temperature kept fairly stable.

4.3 Viewport Characterisation System

The location of the port has resulted in limited physical space for any installations, as such care had to be taken in the design size of the interferometer. The necessary inclusion of a radiation spatial distribution measurement system for characterisation of the viewport also had to be taken into account when installing the interferometer. This section will describe the experimental setup of the radiation measurement systems including the characteristics of all key components involved.

A computer aided design (CAD) model is shown in figure 4.9, showing the full setup. The yellow arrows indicate the direction of propagation of the incident radiation. The interferometer is located within an enclosure, which will be discussed in section 4.3.3.

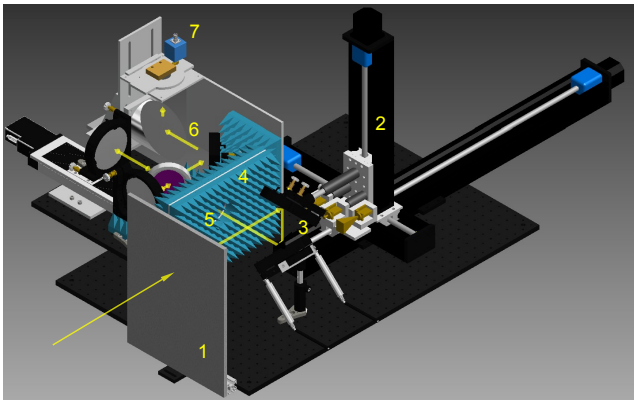

1) High Frequency Filter
2) Spatial Distribution Measurement System
3) Translation Mirrors
4) RF Absorber Foam
5) Enclosure Aperture
6) Interferometer
7) Detector

Figure 4.9: A labelled computer aided design model of the experimental setup (enclosure not shown), with yellow arrows indicating the incident radiations direction of propagation.

The large optical breadboard (M-SA2-23 600×900 mm from Newport Corp.) was installed on an aluminium frame inside the storage ring tunnel, aligned with the viewport. The spatial constraints resulted in the interferometer being constructed separately on a smaller breadboard (M-SA2-12X18 300×450 mm from Newport Corp.), secured perpendicular to the direction of propagation of the incident radiation. The interferometer construction on a separate breadboard outside of the storage ring additionally permitted an excellent opportunity to optically align the system before installation. The positioning of the interferometer, partly due to the necessary requirement of the linear stage system on the main breadboard, consequently required the inclusion of mirrors to reflect the ra-

diation into the system. The individual components within the transfer line are discussed in further detail in subsequent subsections.

4.3.1 Radiation Spatial Distribution Measurement System

To characterise the spatial distribution of the radiation from the viewport, a system was installed consisting of three linear stages. The stages are BiSlide Dovetail Slides from LG Motion [109], two of 10 inch length, the other of 40 inch length. All three stages have a screw lead accuracy of 0.075 mm [109]. The longer stage (attached to the largest breadboard) travels in the direction of propagation of the radiation, and is referred to as the longitudinal stage. The two shorter stages travel perpendicular to the radiation and are referred to as the horizontal and vertical transverse stages. All three stages are attached in positions so as to minimise any risk of collision with other components. Attached to the vertical stage is a detector holder, designed such that three detectors can be installed whilst ensuring the antennae apertures are at the same longitudinal position. The detectors are discussed further in section 4.5. In addition, a translation mirror is attached to the vertical stage via an optical post, the purpose of this mirror is discussed in the subsequent subsection. The stages are connected via cables to a controller system in the Control Instrumentation Area, which provides remote control.

4.3.2 Translation Mirrors

As mentioned at the beginning of this section, spatial constraints required the use of mirrors to reflect the beam into the interferometer. The unknown position of the beam from the port resulted in two silver coated, 4 inch diameter mirrors being installed, along with 2 mirror holders, both of which are U400-AC2K from Newport Corp. The mirrors here and those used in the Michelson interferometer are all good quality broadband reflectors in the optical range, and are therefore of excellent quality for the mm wavelength range under investigation here. Figure 4.10 shows a section of the computer aided design model previously shown in figure 4.9, in particular the path that the incident radiation takes between the high frequency filter (not shown) and the interferometer enclosure aperture. The first mirror in the transfer line (part 1 in figure 4.10) reflects the incident radiation vertically downwards, and is attached to the radiation spatial distribution measurement system so is therefore position controlled. A second mirror (part 3), which is attached to the large breadboard and is actuator controlled, reflects the radiation away from the beam

pipe in the horizontal direction. The actuators for the second mirror are both TRA25PPD from Newport Corp. As the position of both the actuators and stages affect the trajectory of the beam, care must be taken in aligning the interferometer.

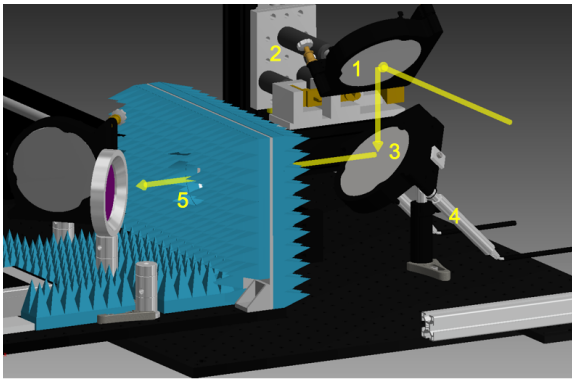

1) Vertical Reflection Mirror
2) Mirror Positioning Stages
3) Horizontal Reflection Mirror
4) Actuators
5) Interferometer Entrance Aperture

Figure 4.10: A section of the computer aided design model from figure 4.9, with yellow arrows indicating the incident radiations direction of propagation.

4.3.3 Interferometer Enclosure

To prevent any stray reflections entering the system and being detected, an enclosure was constructed around the interferometer, as shown in figure 4.9 as component 6. The enclosure frame is constructed from commercially aluminium struts from Rexroth [110], with the enclosure panels being aluminium sheets (available from mechanical workshops at Diamond Light Source). The main section of the enclosure comprises of the top and side panels, all three of which are covered on the inside of the enclosure by an RF absorber which is discussed in section 4.3.4. The front panel was chosen to be unattached from the enclosure as it contains the 70 mm diameter circular entrance aperture which needed precise positioning. The front panel was attached directly to the small breadboard by two aluminium brackets, with both sides of the panel covered in the RF absorber. The rear of the enclosure was left open due to spatial constraints and the presence of the movable arm of the interferometer; the size and location of the arm along with the lack of structure to support a larger enclosure made the inclusion of a rear panel complicated and impractical.

4.3.4 Minimisation of Unwanted Reflections

The RF absorber attached onto the metallic surfaces of interferometer enclosure (component 4 in figure 4.9), is a commercially available pyramidal carbon loaded urethane

absorber (ECCOSORB VHP-NRL-2 [111]). Pyramidal RF absorbers operate on the principal that the taper of the pyramid consequently increases the effective impedance from free space impedance at the pyramid tip, to a lossy medium at the base [112]. The increased surface area as a result of the pyramids results in greater scattering compared to a plane surface. The absorber operates efficiently provided that the pyramid height is longer than one quarter wavelength of the incident electromagnetic wave, however, the majority of research on modelling the absorber has focused around the 100-1000 MHz regime [112–115]. Modelling the absorber includes three physical processes; reflection and scattering from the absorber surface; attenuation through the lossy foam absorber; and reflection from the metallic back surface, whereupon the EM wave propagates back though the absorber and is further attenuated [112]. To model the foam, the absorber can be thought of as a lossy dielectric, whereupon the reflectivity can be trivially calculated. In this case, the relative permittivity of such a material can be written as

$$\epsilon_r = \epsilon'_r + \frac{i\sigma}{\omega\epsilon_0}, \tag{4.7}$$

where ϵ'_r is the real part of the relative permittivity (often referred to as the dielectric constant), σ is the material conductivity, ω is the frequency, and ϵ_0 is the permittivity of free space, the value of which is 8.854×10^{-12} F/m. The complex part of the relative permittivity is responsible for the attenuation within the medium.

To calculate the reflection coefficients from equations 4.5 and 4.6 , the refractive index of the absorber, n_2, can be written in terms of the relative permittivity, ϵ_r, and the relative permeability, μ_r, as

$$n_2 = \sqrt{\epsilon_r \mu_r}. \tag{4.8}$$

Assuming a relative permeability of 1, and the refractive index n_1 being vacuum, the reflection coefficients can be written as

$$r_\perp = \left| \frac{\cos\theta_i - \sqrt{\epsilon_r - \sin\theta_i{}^2}}{\cos\theta_i - \sqrt{\epsilon_r - \sin\theta_i{}^2}} \right|^2, \tag{4.9}$$

$$r_\parallel = \left| \frac{\sqrt{1 - \left(\frac{\sin\theta_i}{\sqrt{\epsilon_r}}\right)^2} - \sqrt{\epsilon_r}\cos\theta_i}{\sqrt{1 - \left(\frac{\sin\theta_i}{\sqrt{\epsilon_r}}\right)^2} + \sqrt{\epsilon_r}\cos\theta_i} \right|^2. \tag{4.10}$$

By defining the real part of the permittivity, ϵ_r', as an effective permittivity of 1, and an incident angle of 0°, then both the parallel and perpendicular cases reduce to the same result shown in equation 4.11.

$$r = \left| \frac{1 - \sqrt{1 - \left(\frac{i\sigma}{\omega\epsilon_0}\right)}}{1 + \sqrt{1 - \left(\frac{i\sigma}{\omega\epsilon_0}\right)}} \right|^2 \tag{4.11}$$

A material such as the absorber has a finite thickness, d, thus any incident wave will experience a phase delay when propagating through the material. The phase delay is given in equation 4.12 [116, 117].

$$\phi = \frac{2\pi d}{\lambda} \sqrt{\epsilon_r - \sin\theta_i{}^2} \tag{4.12}$$

To express the reflection coefficients in terms of a voltage, the final reflection coefficients are then calculated using equation 4.13 [116, 117].

$$R = \frac{r\left(1 - e^{-i2\phi}\right)}{1 - r^2 e^{-i2\phi}} \tag{4.13}$$

The reflectivity, calculated as $10\log_{10}\left(\frac{1}{|R|^2}\right)$, is plotted for two examples in figure 4.11 using the conductivity value of 0.15 $\mathrm{S/m^{-1}}$ [118]. Using the equations 4.13 and 4.11 for a foam height of 5.6 cm, the reflectivity as a function of incident wave frequency at a 0° angle of incidence is plotted in figure 4.11(a). A direct comparison with the manufacturer data sheet is difficult as the only typical values of the reflectivity provided were up to a maximum frequency of 24 GHz [111], well below the frequency region in which we are interested. In addition to this, figure 4.11(b) shows the reflectivity over a range of incidence angles for both parallel and perpendicular reflection coefficients (equations 4.10 and 4.9 respectively). Despite differences between both polarisation cases, the reflectivity is still below -35 dB for a wide angular range, suggesting that sufficient attenuation should be provided by the material at low frequencies. With an effective permittivity of $\epsilon_r' = 1$, then the brewster angle at which perpendicular waves reflect perfectly becomes 45°, as observed by the drop in reflectivity shown in figure 4.11(b).

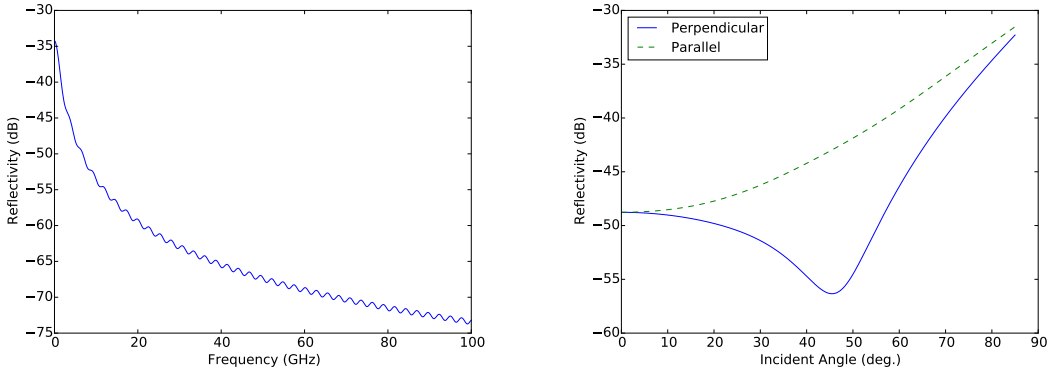

(a) (b)

Figure 4.11: Reflectivity for (a) an incident angle of 0° between 0.1 and 100 GHz and (b) for e-fields both parallel and perpendicular to the plane of incidence, at a constant wavelength equal to the pyramid height, for varying angle of incidence.

4.4 Michelson Interferometer

As discussed in chapter 3, a Michelson interferometer is a practical system for measuring the spectrum of a source using Fourier transform spectroscopy. This section will describe the individual components of the Michelson Interferometer constructed at Diamond for this purpose. Figure 4.12 shows a photograph of the installed setup with the labelled components. The RF absorber foam labelled as part 8, the principles of which is described in section 4.3.4, corresponds to the front panel with circular entrance aperture. As discussed in section 4.3.3, the enclosure roof sits on the aluminium frame. The long wavelengths being measured means that the components are larger compared to those in a more common optical interferometer, however, it also needed to be as compact as possible to minimise diffraction contributions, distortions to the beam wavefront, and the drop in signal from any beam divergence. Spatial limitations at the viewport meant components were added to the conventional setup.

4.4.1 Beamsplitter

Beamsplitters in the far-infrared region (particularly at longer wavelengths) have limited choice compared to those for optical wavelengths, therefore selection of the splitter is essential as its efficiency determines the frequency regions in which the setup can operate successfully. Typical examples of beamsplitters include dielectric films or substrate-coated splitters [119]. Dielectric films such as Mylar or Kapton have high refractive indices

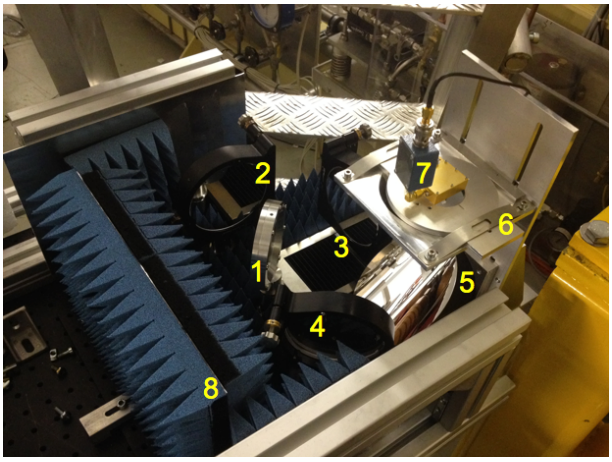

1)	Beamsplitter
2)	Fixed Interferometer Arm
3)	Movable Interferometer Arm
4)	Translation Mirror
5)	Focussing Mirror
6)	Detector Holder
7)	Detector
8)	RF Absorber Foam

Figure 4.12: A photograph of the installed Michelson interferometer with its key components labelled.

(around 1.7 - 1.9 [120]), and substrate-coated splitters are typically opaque below ≈ 5 THz [119]. Recently, crystal silicon beamsplitters have been employed showing good efficiency in the far-infrared region [119,121]. Similar to dielectric films and the viewport window as detailed in section 4.2.2, the splitter works on the principal of multiple internal reflections, and can therefore be calculated accurately. As such, the beamsplitter installed in the interferometer is a 94 ± 2 μm thick, 76.2 mm diameter polished silicon wafer from Compart Technology. A 160 ± 2 μm thick silicon beamsplitter of the same diameter was used in early experiments with the pyroelectric detector, however the splitter efficiency detrimentally affected the measured spectra and was therefore replaced by the thinner splitter. The effect of the 160 μm splitter on the spectra is discussed in section 5.4.

Similarly to the viewport window in section 4.2.2, the silicon wafer splitter can be modelled using the Fresnel reflection coefficients as shown in equations 4.5 and 4.6. Further from this, the beamsplitter efficiency can be calculated from:

$$E = 4R_0T_0 \tag{4.14}$$

Figure 4.13 shows the calculated efficiency for the silicon splitter along with calculated efficiencies of Mylar and Kapton, all for the same thickness of 94 μm. For the calculation of the beamsplitter efficiency, the refractive index n_1 was set to that of air at standard room temperature and pressure, the angle of incidence was set at 45 degrees, and the refractive index and absorption coefficient data for the splitters was taken from [105, 119, 121] for silicon, [122] for Mylar, and [123] for Kapton. The predicted efficiency is shown up to a frequency of 1000 GHz along with a comparative form factor from

a 1 mm long Gaussian bunch. The silicon splitter offers the best efficiency of the three materials, with Mylar and Kapton having efficiencies lower than ~ 0.4 over the whole frequency range. This is due to the relatively large refractive index of silicon (~ 3.41) and that the absorption of these wavelengths in silicon is negligible [121]. Despite a clear drop in efficiency at low frequencies (< 100 GHz), the effective beam pipe cutoff as calculated in equation 2.33 to be $\approx 54\ GHz$ results in the efficiency drop being of little consequence due to lack of expected signal. Further decreases in efficiency to 0 additionally appear periodically, therefore a lack of observed signal can be expected at these frequencies. Any remaining recorded spectra can be normalised to the splitter efficiency.

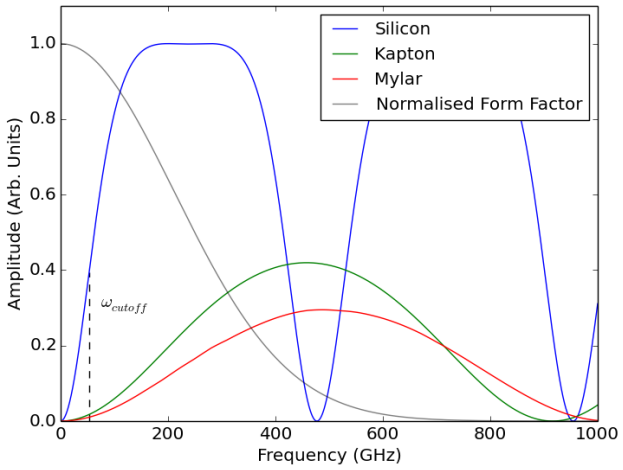

Figure 4.13: Predicted efficiency for an S polarised beam, incident at 45° onto a 94 μm thick beam splitter for multiple materials, with a normalised theoretical form factor for a 1 mm long Gaussian electron bunch.

The beamsplitter holder is a custom-made design, used in an interferometer in a previous experiment [124]. The holder comprises of two metallic rings which are screwed together, providing an internal diameter of 70 mm. The holder is attached to an optical post, via a threaded hole in one of the holder rings. This proved advantageous when aligning the system as the second ring and splitter could be removed without affecting the position and angle of the overall holder. Alignment is discussed further in section 4.8.

4.4.2 Mirrors

In both arms of the interferometer, a 4 inch diameter silver coated mirror is employed, along with the same model of mirror holder as mentioned in section 4.3.2. For the static arm (part 2 in figure 4.12), the mirror is simply fixed in place, attached to the optical

breadboard. For the movable arm (part 3 in figure 4.12), the mirror holder is attached to a UTS150CC linear stage from Newport Corp. The stage has a 150 mm long travel distance, with a minimum incremental motion of 0.3 μm and resolution of 0.1 μm [125]. All mirrors are assumed to be perfectly reflective.

After the beams in the two interferometer arms are recombined at the beam splitter, a third half silvered mirror is used to translate the beam, again 4 inches in diameter and held in an identical mirror holder. The final mirror in the system is a parabolic mirror placed such that the incident beam is reflected and focused upwards in the vertical direction. The mirror is a 90° off-axis parabolic aluminium mirror from Edmund Optics, with a 4 inch diameter and an effective focal length of 6 inches.

4.4.3 Detector Holder

To hold the detector, a custom made holder was design and constructed at Diamond Light Source. Shown as component 6 in figure 4.12, the detector holder along with the quasi-optical detector and focussing mirror are shown separately in figure 4.14 with the direction of propagation shown indicated by the yellow arrows. As the direction of propagation of the incident radiation is in the vertical direction, the detector is attached to a metallic plate (with aperture) which can be moved in the transverse plane. The plate is secured in place onto a second metal plate (with aperture) in the same plane by two metallic strips (not shown). The second plate is attached to a large vertical plate by screws through two grooves, thus providing the ability to move the plate in the vertical direction and move the detector longitudinally into the focal point of the parabolic mirror. The exacting position of the detector during system alignment is discussed in section 4.8. The detector in figure 4.14 is the quasi-optical detector, discussed further in section 4.5.2.1. Shown attached to the detector is an external box to protect the detector against electrostatic discharge.

4.5 Detectors

For the application of a Michelson interferometer in the mm wave range, the choice of detector is important for numerous reasons. A common choice of detector for these wavelengths is either a Golay cell or hot electron bolometer. Whilst the Golay cell offers excellent sensitivity and bandwidth, its response time is limited to the order of 10 ms [126]. A hot electron bolometer also offers excellent sensitivity and bandwidth, and in addi-

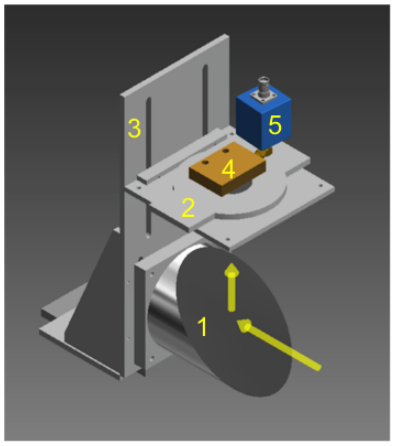

1) Focusing Mirror
2) Horizontal Plate
3) Vertical Plate
4) Detector
5) Electrostatic Discharge Protection

Figure 4.14: Detector holder used in the Michelson interferometer, shown with the focussing mirror and the quasi-optical detector.

tion operates at very low noise, however, the need to operate the detector at ~ 4 Kelvin requires a significant installation of cryogenic equipment and a supply of liquid helium, which, given the spatial constraints of the setup means the use of a bolometer is highly impractical. In recent years, Schottky Barrier Diode detectors have become commercially available which provide excellent sensitivity, low noise, and fast response whilst operating at room temperature, albeit in a modest bandwidth. Pyroelectric detectors additionally offer similar properties over a large bandwidth, however they have a slower response time and higher noise floor. The two types of detector used during experiments were Schottky Barrier Diode detectors and pyroelectric detectors, which will now be discussed.

4.5.1 Pyroelectric Detector

Pyroelectric detectors operate by utilising the change in surface charge when an asymmetric crystal in the detector head is heated. As the change in charge is measured, the detector cannot be used for a DC signal and must therefore be modulated. The modulation of this detector is discussed in section 4.2.3. For our application, the pyroelectric detector is a THZ-I-BNC from Gentec [127] that detects frequencies between 0.1-30 THz, with a noise equivalent power of 1000 pW/$\sqrt{\text{Hz}}$ and sensitivity of 70 kV/W. The signal from the detection circuitry is amplified by an in-built amplifier, therefore an external power supply is required. The detection circuit is located behind a tapered circular aperture which provides a small directional gain.

The circular aperture in the detector consequently means that any incident wave illuminating the detector will be susceptible to diffraction. The intensity of a wave that

has penetrated an aperture of radius a and is measured within a disk of radius R_0 is given by $2\pi \int_0^{R0} r \left|E(r,k,a)\right|^2 dr$ where E is the electric field, and k is the wavenumber [128]. The transmission through the aperture is the ratio of this penetrated intensity to that of the intensity of the plane wave incident on the aperture, and can be found from equation 4.15, where E_0 is the amplitude of the incident wave [128].

$$T_A = \frac{2}{a^2 E_0^2} \int_0^{R0} r \left|E(r,k,a)\right|^2 dr \tag{4.15}$$

The electric field of a cylindrically symmetric incident wave is shown in equation 4.16, where N_F is the Fresnel number, given by $N_F = \frac{a^2 k}{D}$ where D is the distance between the aperture and the plane of observation, and J_0 is the zero order Bessel function of the first kind [128, 129].

$$E(r,k,a) = i2\pi N_F e^{-i\pi N_F \left(\frac{r}{a}\right)^2} \int_0^1 \frac{x}{a} E_0 e^{-i\pi N_F \left(\frac{x}{a}\right)^2} J_0\left(\frac{2\pi N_F r}{a} \frac{x}{a}\right) d\left(\frac{x}{a}\right) \tag{4.16}$$

Figure 4.15 shows the transmission for the pyroelectric detector, based upon its dimensions of a 5 mm radius entry aperture, through a circular disk at a distance of 5 mm, with a radius of 2.5 mm. As one would expect, the aperture transmission only becomes significant at low frequencies, below that of the effective beam pipe cutoff as indicated in figure 4.15.

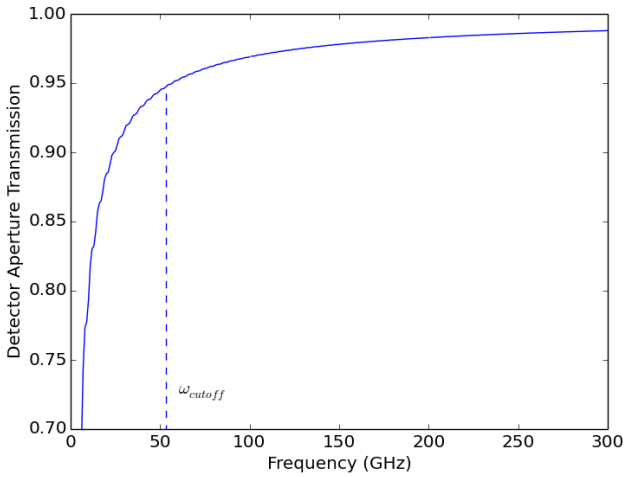

Figure 4.15: Theoretical intensity due to diffraction losses through a 5 mm radius circular aperture, measured over a 2.5 mm radius region in a plane at a distance of 5 mm from the aperture.

4.5.2 Schottky Barrier Diode Detectors

A Schottky barrier diode is formed by the direct contact of a metal with a semiconductor. To better understand the junction that is formed by the contact of these two materials, the energy bands are shown in figure 4.16 for the case where; (a) the two materials are separate from one another; and (b) where the materials are in contact [130]. In figure 4.16, the semiconductor is an n-type GaAs substrate, in which electrons are restricted to discrete energies in the valence and conduction bands, labelled as E_V and E_C respectively. Between these two bands is the Fermi level, E_F, a level where the probability function of electrons occupying this level at thermal equilibrium is equal to one half. In the metal, for electrons to move from this level to the vacuum potential, an energy is required given by the metal work function, Φ_m. In the semiconductor, the energy difference between this vacuum potential and the conduction band is given by the electron affinity, $q\chi$.

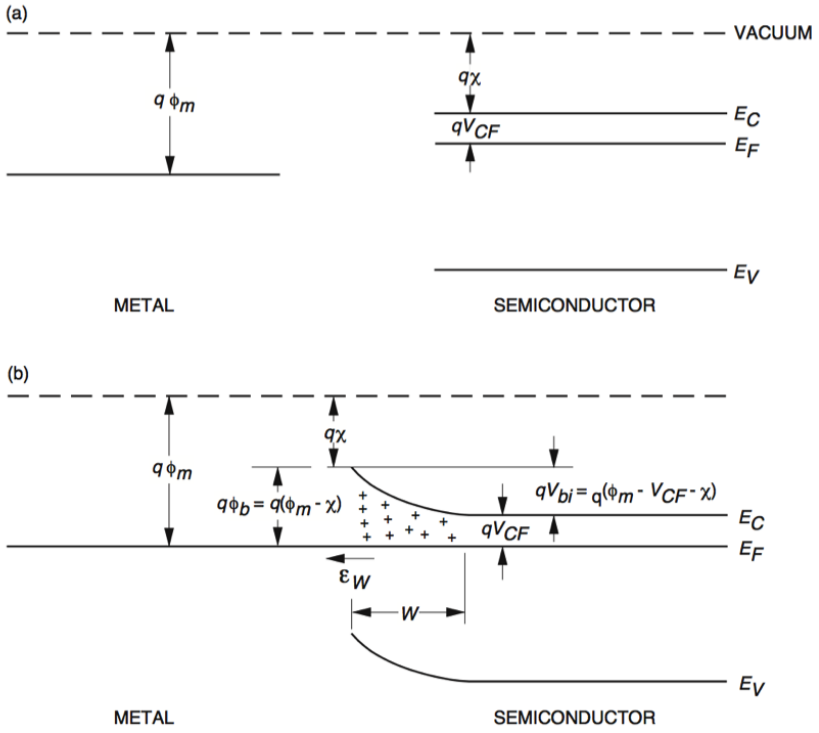

Figure 4.16: The energy band diagram of the metal-semiconductor junction in a Schottky barrier diode [130].

If, before contact, the Fermi level of the semiconductor is greater than that of the metal ($\chi + V_{CF} < \Phi_M$), then when the two materials are in contact, electrons will diffuse from the semiconductor to the metal, leaving an overall positive charge behind at the junction. The positive charge will exert a force on electrons trying to diffuse to the metal,

thus an equilibrium will be reached. It is this force that is responsible for the bending of the energy levels [130] as seen in figure 4.16. This bending occurs in the depletion region, with the amount of bending called the built in potential, V_{bi}. For electrons to cross from the semiconductor to the metal, they must overcome this potential V_{bi}, whereas for electrons to cross from the metal to the semiconductor they must overcome the larger potential Φ_B, known as the barrier potential.

When an electromagnetic wave is incident upon the diode, a current is generated from electrons crossing the depletion barrier into the metal through thermal activation. Whilst quantum tunnelling is possible, thermal effects are dominant as the process occurs at room temperature. The diode will produce an output voltage without the need for an external DC bias, with the voltage being proportional to the input radiation power.

To guide the radiation onto the diode in a standard detector, a standard gain horn antenna directs incident radiation into a rectangular waveguide, thus the detectors are polarisation sensitive. The use of a waveguide additionally limits the bandwidth of the detector due to the low frequency cutoff and reduced effectiveness at higher frequencies. The properties of the available standard Schottky Barrier Diode detectors are shown in table 4.2. The detector technology has been shown experimentally to have a response time of less than 1 ns FWHM [131], therefore bunch by bunch detection is possible given the bunch spacing of 2 ns.

Detector Model	**DXP-12**	**WR5.1ZBD**	**WR3.4ZBD**	**WR2.2ZBD**
Frequency Range (GHz)	60-90	140-220	220-330	325-500
Wavelength (mm)	3.33 - 5	2.1 - 1.5	1.4 - 0.9	0.9 - 0.6
Sensitivity (mV/mW)	700	2000	1500	1250
NEP (pW/$\sqrt{\text{Hz}}$)	2.0	2.7	2.7	2.7

Table 4.2: Specifications of four ultra-fast Schottky Barrier Diode detectors (quoted sensitivity is for termination into 1 MΩ).

4.5.2.1 Quasi-Optical Detector

Whilst the waveguide based detectors are suitable for simple instability detection experiments, the employment of multiple detectors in the interferometer is problematic. Recent developments have led to commercially available Schottky Barrier Diode detectors with a much larger bandwidth, as such a quasi-optical detector from Virginia Diodes [132] was

used, providing a responsivity around 100-250 V/W between 100 and 1000 GHz with a noise equivalent power of $\sim$ 20 pW/$\sqrt{\text{Hz}}$. The detector uses an antenna mounted on a 10 mm diameter silicon substrate lens, therefore focusing any incident radiation. The detector is particularly direction sensitive, therefore care must be taken when positioning and aligning the system.

4.5.3 Detector Summary

Figure 4.17 shows a summary of the fast response (Schottky Barrier diode) detectors that are available, with a normalised form factor for a 0.5mm long Gaussian bunch. Each box in the plot corresponds to a single detector, with the box width representing the detector bandwidth, and the box height representing the typical sensitivity. Note that the absence of the pyroelectric detector due to its large bandwidth and sensitivity, thus the plot is limited to the fast response detectors. The available detectors directly cover the majority of the spectrum except between 90 and 100 GHz, however, as the waveguide based detectors are sensitive above their stated bandwidth, and the quasi-optical detector has no waveguide and is therefore sensitive below its stated bandwidth, then some of the detectors should be responsive in this region.

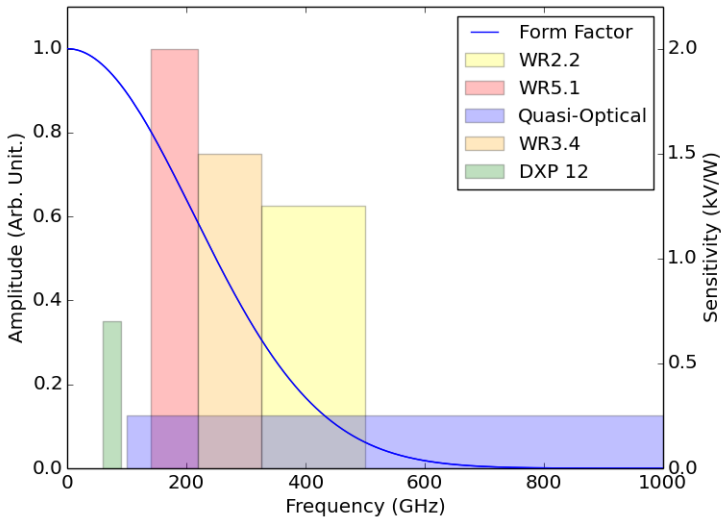

Figure 4.17: Box plots showing the bandwidth (box width) and typical sensitivity (box height) of available Schottky Barrier Diode detectors, with a normalised theoretical form factor for a 0.5 mm long Gaussian electron bunch.

4.6 Data Acquisition System

To control the experimental setup that is described in the previous sections, a hardware interface was required, a diagram of which is shown in figure 4.18. The hardware control interface additionally monitors other machine parameters from additional diagnostic equipment, as described in section 4.1.2. The data acquisition (DAQ) system in figure 4.18 is shown in two parts; the control instrumentation area where the majority of the hardware control and DAQ machines are located; and the storage ring tunnel where the experiment is installed with the remainder of the hardware controllers. The arrows in the diagram indicate the direction of communication between devices. The hardware controllers in the tunnel are limited to two SMC100PP controllers and an SMC100CC controller which control the two actuators and interferometer linear stage respectively. The controllers are in the storage ring tunnel due to the short cables from the stage and actuators. The SMC model of controllers have the ability to daisy-chain together, thus only a single connection with the network is needed. The primary controller is accessed via RS232, which is connected to an RS232 to ethernet hub. The chopper controller is additionally located in the tunnel, again due to the length of cable (from the optical chopper).

It should be noted that the streak camera, as discussed in section 4.1.2.1, is not

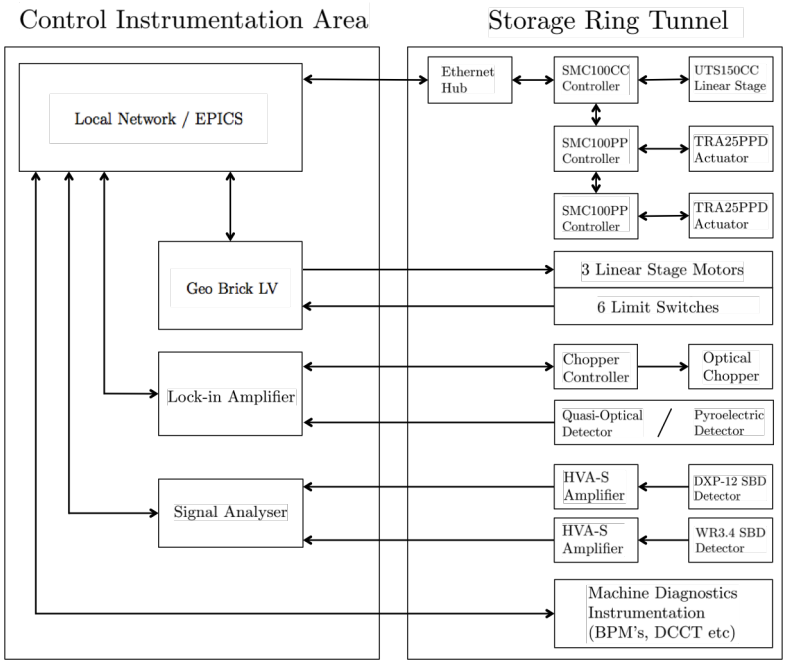

Figure 4.18: Data acquistion component diagram showing the separation of the hardware into two locations; the Control Instrumentation Area which houses the majority of the control interface hardware; and the storage ring tunnel.

included in the diagram in figure 4.18 as the camera is located in a separate optical diagnostics cabin outside of the storage ring. The camera is connected to a computer in the cabin, which is remotely accessed during experiments. The remaining control hardware interface devices are discussed in the following sections.

4.6.1 Detector Amplification

For the initial detection experiments, to boost the signal power, a single amplifier was available to increase the signal of the 60-90 GHz detector, as it had been used in successfully previous experiments at Diamond light source [41, 42]. The amplifier was a 40 dB HSA-X-1-40 amplifier from Femto. As signal amplification is desirable, for the application of this project, low noise amplifiers are preferential due to the low voltage signal from the detector. Custom made low-noise amplifiers, HVA-S from Femto were used, both providing a selectable 40 or 60 dB gain in a DC to 1 MHz bandwidth at with equivalent input noise voltage of 1.1 nV/$\sqrt{\text{Hz}}$. The detector sensitivity shown in table 4.2 is for a 1 MΩ input impedance, however the amplifier with a 1 MΩ impedance is not currently possible without increased noise.

4.6.2 Impedance matching

As discussed in the previous section (4.6.1), amplifiers were installed for the SBD detectors in the distribution measurement system. The input impedance of the amplifier was chosen to be 10 kΩ as opposed to the standard 50 Ω impedance in RF equipment as it provides a higher impedance without sacrificing the low-noise. By considering the diode as a voltage source with impedance R_j, feeding the amplifier's load resistance R_L (i.e. 10 kΩ), the sensitivity will be reduced according to equation 4.17 , where γ_1 is the reduced sensitivity value and γ_2 is the original sensitivity [133]. As a result, the 10 kΩ amplifier impedance reduces the sensitivity.

$$\gamma_1 = \gamma_2 \left(\frac{R_L}{R_j + R_L} \right) \tag{4.17}$$

An accurate junction resistance was not provided by the diode manufacturer, but it can instead be calculated using equation 4.18 where I is the current through the diode, I_s is the saturation current, V_b is the voltage across the Schottky barrier, η is the ideality factor, and V_t is the thermal voltage [133].

$$I = I_s \left[e^{\left(\frac{V_b}{\eta V_t}\right)} + 1 \right] \tag{4.18}$$

The voltage V_b can be written as $V_b = V_a - IR_s$, where V_a is an applied voltage and R_s is the series resistance. The junction resistance, R_j is obtained from equation 4.19.

$$R_j = \frac{dV_b}{dI} \tag{4.19}$$

In the case where I_s is small, the junction resistance reduces to $R_j = \frac{\eta V_t}{I}$. To calculate the junction resistance, the current-voltage characteristics for the detectors were measured and the resulting data was fitted to equation 4.18 to obtain the remaining parameters. Figure 4.19 shows the measured and plotted data for the 60-90 GHz SBD detector, along with the optimised parameters from the data fit. The characteristics of the other detectors are not shown, however the new sensitivity values for all the detectors are shown in table 4.3. The sensitivity for a 50 Ω load resistance were also calculated and shown to result in a decrease in sensitivity by an order of magnitude, as displayed in table 4.3.

Detector Model	Frequency (GHz)	1 MΩ Sensitivity (mV/mW)	10 kΩ Sensitivity (mV/mW)	50 Ω Sensitivity (mV/mW)
DXP-12	60-90	700	500	10
WR5.1ZBD	140-220	2000	1900	150
WR3.4ZBD	220-330	1500	1400	100
WR2.2ZBD	325-500	1250	1200	100
Quasi-Optical	100-1000	250	200	10

Table 4.3: Sensitivity values of the Schottky Barrier Diode detectors for different load impedances.

4.6.3 Lock-in Amplifier

The lock-in amplifier, located in the control instrumentation area, is a model 7280 from AMETEK. The amplifier operates up to 2 MHz, using a reference from either an external source or built-in oscillator, with variable signal voltage sensitivity from 10 nV up to 1 V for a reference frequency of $50 \leq f < 250$ kHz, and 100 nV up to 1 V for $0.25 \leq f \leq 2.0$ MHz. An on-board memory buffer is capable of storing up to 32,768 data point for selected modes of operation. The gain of the amplifier is variable up to 66 dB. As described in section 4.2.3, the modulation chopper was installed for use with the pyroelectric detector,

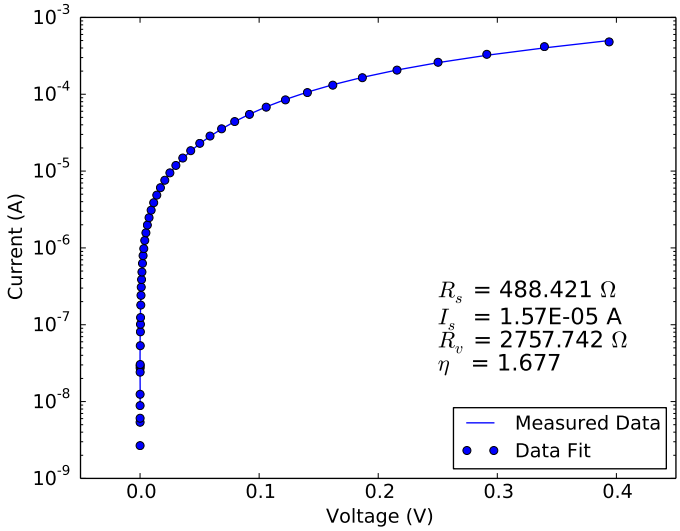

Figure 4.19: Current-voltage graph for the quasi-optical Schottky Barrier Diode detector.

which acted as the reference frequency. As remote communication with the lock-in is possible, and the lock-in amplifier can also communicate with the chopper control unit, it was possible to control the choppers rotational frequency. The optical chopper as described in section 4.2.3 is limited to below $\sim$ 40 Hz, so for the cases where the pyroelectric detector with a slow response time is used in measurements, the reference signal is taken from the chopper. For the quasi optical detectors which has a fast response time, the chopper was stopped and the lock-in switched to use its internal oscillator as the reference frequency, set to be the bunch revolution frequency. The experimental procedure for operating the lock-in amplifier is discussed in subsection 4.7.

4.6.4 Signal Analyser

An Agilent N9020A signal analyser in the control instrument area is utilised for recording the signal from the Schottky Barrier Diode detectors in the radiation distribution measurement system and the instability detection setup described at the beginning of section 4.2. The signal analyser is a 2 channel device capable of measuring signals up to 6 GHz with a noise floor of -166 dBm. The analyser is capable of measuring signals in both the time and frequency domains, which can be triggered by with an in-built trigger or external source. The analyser is accessed in the control room either by remote desktop or via SCPI commands.

4.7 Experimental Methodology

Three major types of scans were performed during experimental operation; a 2D/3D scan by the spatial distribution measurement system, and two types of interferometer scan, referred to as 'slow' and 'fast'. As one may deduce, the scans differ primarily in operational time; early operation of the interferometer required potentially significant time (up to approximately 45 minutes) to complete a single scan. The scan length, however, depended on the number of detector signal measurements per mirror position, and the mirror position resolution. Scans over such a long period are undesirable due to the limited experimental time. As such, a second operational procedure was developed that reduced the interferometer scan time down to approximately 10 seconds. The procedure for operating these three types of scans is as follows:

2D/3D Scan The three stages were moved into initial positions and incrementally moved as desired in the transverse axes, with multiple readings taken from the detectors attached to the stages. Once finished, any increment in longitudinal position is applied, and the scan in the transverse plane is repeated.

Slow interferometer scan The actuators and the spatial distribution measurement system are moved into their appropriate positions such that the incident radiation enters the interferometer. The lock-in amplifier is initialised and set to record 20 samples at each interferometer mirror position. The start and end absolute positions and step size of the interferometer stage are set, and consequently moved into its initial position. The mirror is then moved incrementally, and the signal recorded, with average and standard deviation of the samples being returned.

Fast interferometer scan Similar to the slow scan, the non-interferometer components are set in position. The lock-in is then initialised, however, in this case, the number of points recorded is set to 800, and the sampling time set to every 20 ms. The velocity at which the stage moves in then altered to 5mm/s, thus the scan will be 80 mm long (around the point of zero path difference), but will be recorded in a constant sweep rather than incrementally. The lock-in then starts taking data (stored in a local buffer), and the mirror is moved. Upon completion, the data held in the buffer are then downloaded. The long integration period of the pyroelectric detector means this method can only be used for the quasi-optical detector.

Whilst the fast scan has the obvious advantage of speed, the drawback is that the signal at a given position will have an unknown error. As such, the scan is set to repeat 5 times, thus the total scan time for the fast scan is around 1 minute. The two speeds at which the interferometer can be operated both adversely affect either the frequency resolution or bandwidth. Whilst recording a high resolution interferometer scan over a long range is possible in the slow scan, the long duration renders the operation impractical. The slow operation is therefore more suited to short scans around the point of zero path difference at high resolution. Alternatively, the fast scan offers speed but at the expense of a limited number of data points, thus a long scan range will have high frequency resolution, but poor bandwidth. The stage in the movable interferometer arm has a total travel length of 150 mm, therefore the maximum path difference is 300 mm. The smallest frequency resolution is therefore $300 \times 10^{-3}/c = 1$ GHz. The highest resolvable frequency (temporarily ignoring detector frequency limits) is determined by the spatial resolution in the measured interferogram. For example, moving the interferometer mirror in 0.1 mm increments results in the smallest resolvable optical path difference of 0.2 mm, therefore the largest resolvable frequency is $0.2 \times 10^{-3}/c = 1.5$ THz. As such a spatial resolution corresponds to frequencies beyond the specified limit of the quasi optical detector (shown in table 4.3), the scan length and resolution can be chosen to optimise for the frequency resolution and bandwidth.

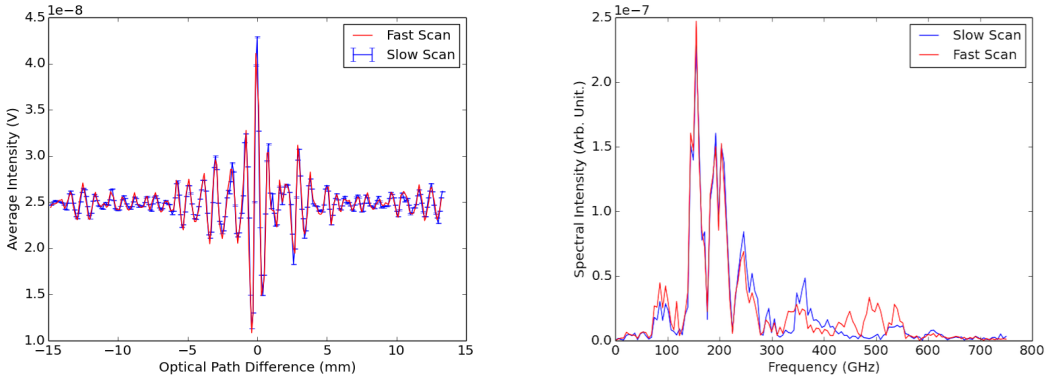

(a) Interferogram

(b) Resulting Spectra

Figure 4.20: Interferograms and corresponding spectra using both slow and fast interferometer scans from 100 bunches in low alpha optics.

4.7.1 Interferometer Speed Comparison

A comparison of the two types of interferometer scans are shown in figure 4.20, along with their corresponding spectra. Both scans were recorded using the quasi-optical detector in low alpha operation, with 100 bunches at 0.015 mA per bunch. The fast scan does not display errors as only one measurement was recorded at the same bunch current and fill pattern as the slow scan. The position ranges and DAQ were set such that both scans recorded the same number of points at a resolution of 0.1 mm, however only ± 15 mm around the point of zero path difference is shown here.

Whilst the interferograms appear visually similar, small variations lead to a noticeable difference in their spectra at high frequencies, for example the fast scan displays a significant signal around 500 GHz which is not present in the slow scan. The detector signal in the slow scan is the average of many samples at a given position and thus smoothes out the fluctuations, similar in effect to the pyroelectric detector. The fast scan, however, is more susceptible to a fluctuation as a result of the instability given the shorter time over which the signal is measured at a given position. Despite this, if the high frequency coherent emissions vary significantly from shot to shot, any recorded spectra will be a smoothed out representation of the emitted spectra as the present system is incapable of measuring a single shot both in terms of DAQ performance and operational speed of the interferometer. As such the fast scan operation of the interferometer is preferential as it is capable of measuring fluctuations in the large bursts from the instability's quasi-periodic regime.

4.8 Alignment

The alignment of the system comprised two methods. The first was to use a 633 nm optical laser along with a number of irises positioned in the system as to be in line with the other components. The position of the translation mirror after the recombination of the split beams (part 4 in figure 4.12) required the removal of the splitter, and the laser to be positioned in place of the fixed interferometer arm. Whilst the silicon splitter provides good efficiency for the radiation wavelengths in which we are interested (as discussed in 4.4.1), it is opaque to wavelengths of visible light. As the holder was fixed in place by only one of the holders rings, the second ring and consequently the splitter were removed, thus providing a clear path to the mirror which could then be aligned such that the angle of

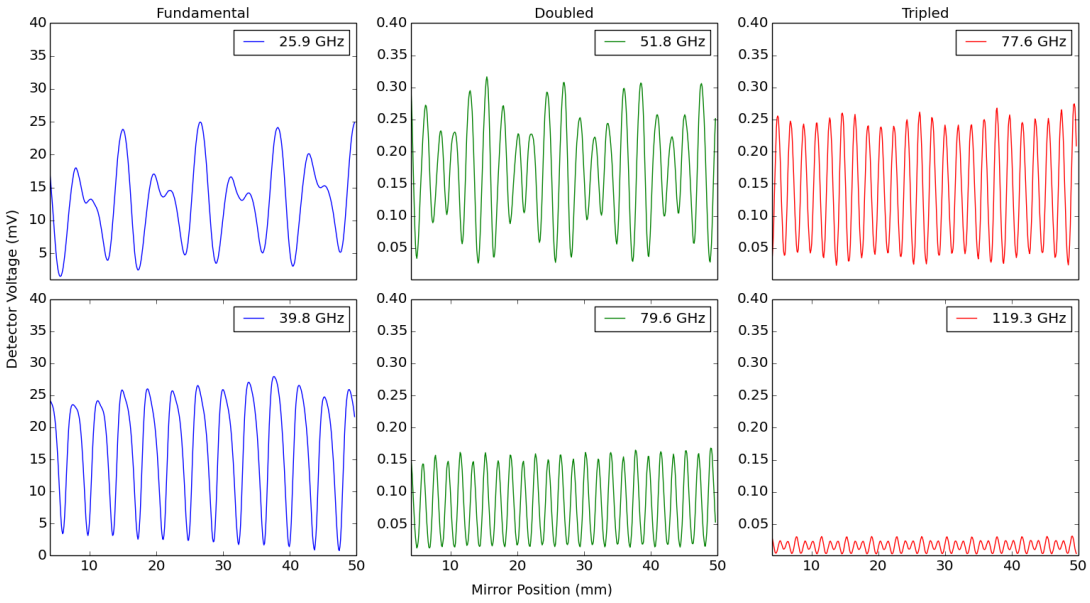

Figure 4.21: Alignment testing by recording interferograms using a Ka Band RF source with frequency multipliers.

incidence was 45°. The laser was then replaced with the fixed mirror, and subsequently placed at the viewport so as to represent the emitted synchrotron radiation. Prior to placing the splitter, the movable arm of the interferometer was additionally aligned so as to reflect the incident beam back along its path to the laser. As the splitter is polished and appears reflective to the naked eye, the splitter was used to reflect the laser, thus it was possible to align both the fixed arm of the interferometer and the angle of the beamsplitter holder.

A complication to the laser alignment was the inability to optimally position the detector due to its inability to detect visible wavelengths. Consequently, a custom built RF source owned by Royal Holloway was utilised. The RF source emits a variable power, variable frequency signal between 26.5 and 40 GHz from a rectangular waveguide. Two frequency multipliers from Millitech Inc. were additionally available (a doubler and a tripler, MUD-15 and MUT-10 respectively), along with a pyramidal standard gain horn antenna for each multiple of the fundamental bandwidth, each typically providing a 24 dBi gain. The rectangular waveguide emits a polarised signal, thus the RF source was positioned in front of the viewport so as to emit the same polarisation as one would expect from the emitted synchrotron radiation. The RF source was modulated at 20 Hz with the same signal provided (as the reference signal) to the lock-in amplifier to which the detector was connected.

For the detector position, the DAQ was set up to record the detector voltage continuously whilst the detector was manually moved until the position providing the highest voltage was found. Once achieved, scans using the interferometer were conducted to test both alignment and proof of principle of operation. Figure 4.21 shows the recorded interferograms for the lowest (top) and highest (bottom) frequencies from the fundamental (left), doubled (middle) and tripled (right) bands. Both the frequency doubler and tripler suffer from an approximate 20 dB conversion loss, as seen in the signals.

The resulting spectra, as calculated by the methodology described in section 4.7, are shown in figure 4.22. The results have been normalised such that the power integrated over the whole bandwidth of each spectra equals unity. Despite one expecting spectra being near monochromatic, the spectra from the lowest programmed frequency (left plot in figure 4.22) in the fundamental and doubled bands unusually shows other additional high power components. Most notable is that whilst the doubled frequency of 51.8 GHz is clearly present, a higher power component at $\sim$ 65 GHz is observed. As this does not appear to be the result of a doubling of a frequency in the fundamental bandwidth, it is thought to possibly be an artefact of the doubler itself, however the exact cause remains unknown. The signals at the highest programmed frequency, however, behave as expected albeit harmonics appearing in the spectra.

As mentioned in section 4.5.2.1, the specified frequency band over which the detector is sensitive is 100 to 1000 GHz, however the alignment scans here clearly show detection of signals at lower frequencies. As such, we are unsure of exactly how the detector responds

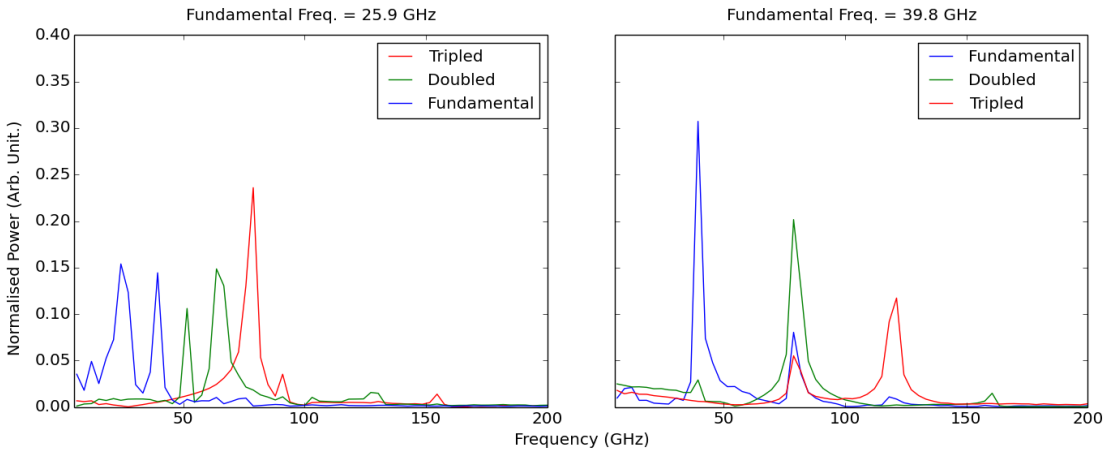

Figure 4.22: Resulting spectra from interferograms in figure 4.21 using a Ka Band RF source with frequency multipliers.

below its stated lower limit, but we should not be surprised by the presence of signals below 100 GHz in any experimental results.

4.9 Radiation Spatial Distribution Measurements

Now that the system has been described and alignment has shown the interferometer to operate successfully, to extract any spectra from the interferometer measurements, any overall systematic effects must be accounted for. A large effect on the spectrum is the optics of the system. If we assume that the emitted beam from the electron bunch is of a Gaussian form, propagating along the z-axis, then the width of the divergent beam as a function of distance, $\omega(z)$, for a constant wavelength λ is given by equation 4.20, where ω_0 is the beam waist and z_R is the Rayleigh Range, given by equation 4.21 [129].

$$\omega(z) = \omega_0 \sqrt{1 + \left(\frac{z}{z_R}\right)^2} \tag{4.20}$$

$$z_R = \frac{\pi \omega_0^2}{\lambda} \tag{4.21}$$

The half-angular divergence of the beam is given by

$$\theta \simeq \frac{\lambda}{\pi \omega_0}. \tag{4.22}$$

As such, a longer wavelength beam will be wider than a short wavelength beam for $z \neq 0$. As a detector in a stationary position may be located at some radial distance from the centre of the beam, the spectral density is shifted in favour of longer wavelength emissions, thus misrepresenting the power spectrum. With the detectors being attached to the translational stages, it is possible to spatially map the distribution of the emissions, and consequently calculate the location and size of the beam waist along with the unmeasured regions of the distribution. The stage system itself is located at an unknown distance z from the beam waist therefore we cannot immediately measure a distribution and fit it according to equation 4.20. For the case where $z \gg z_R$, the beam width increases linearly with distance, therefore measuring the beam width at multiple positions of known separation allows us to determine the half-angular divergence, and consequently the beam waist.

To accurately measure the spatial distribution, scans with both a large range and

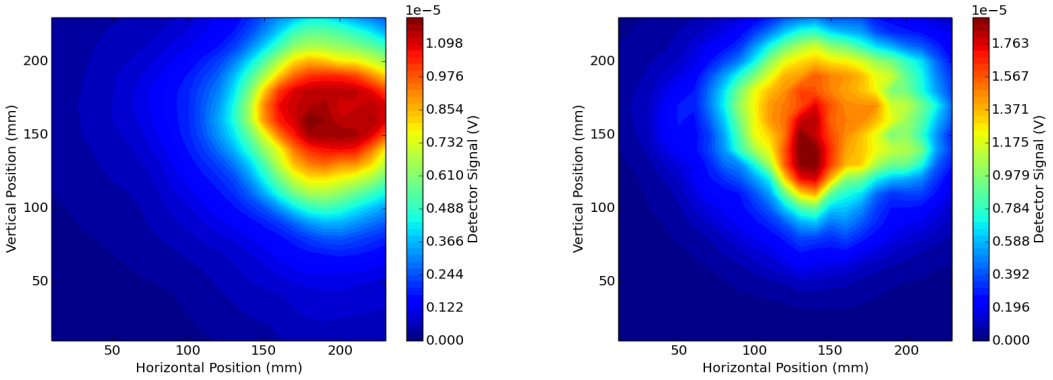

(a) DXP-12 (b) WR3.4

Figure 4.23: Spatial distribution of radiation from a 60-90 GHz (4.23(a)) and a 220-330 GHz (4.23(b)) detector.

high position resolution were performed using the 2D/3D scan as outlined in section 4.7. The amount of time necessary to achieve this during dedicated data-taking sessions is too long, however it was possible to partially measure the distribution from a low alpha user run where the beam is stored as a near constant current courtesy of bunch topup. The DAQ script recording the data paused temporarily during topup so as to not record any change in signal from the temporary increase in bunch motion. The reduction in momentum compaction factor from this lattice consequently reduces the instability's threshold current by a factor of ~ 60, therefore with the storage ring operating with a cavity voltage of 3.3 MV and a bunch current of 50 μA, this mode of operation will result in the bunches being in the instability's quasi-stable state. With the beam naturally emitting bursts of CSR, the spatial distribution measurements can be made parasitically. For the measurements the stages were moved incrementally in steps of 10 mm transversely over the whole available scanning range. The longitudinal stage was moved in steps of 20 mm. Figure 4.23 shows the measured distributions from the DXP-12 (60-90 GHz) and WR3.4 SBD (220-330 GHz) detectors at the same longitudinal position.

The horizontal profile was fitted to a Gaussian distribution plus offset using a least squares fit, as shown in figure 4.24 whereupon the width of the beam is found as a fit parameter. Whilst the DXP-12 detector clearly agrees well with a Gaussian fit, the measured distribution from the WR3.4ZBD does not. The experiments were conducted such that the horizontal profile was scanned for each vertical position, thus the form of the measured profile being similar for multiple vertical displacements suggests the unusual pattern is not a result of fluctuations in beam conditions, but rather a smearing out of

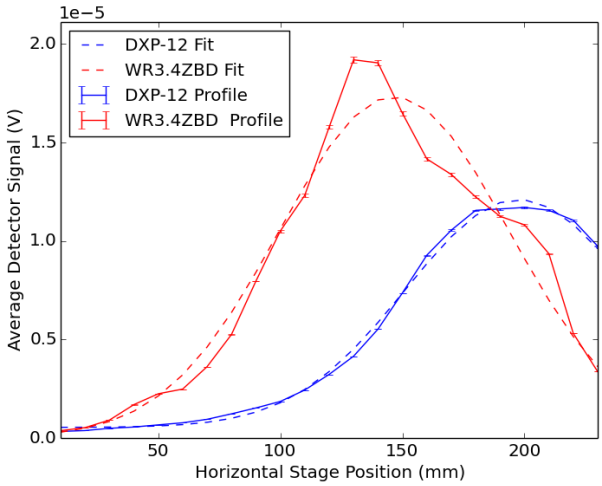

Figure 4.24: Example horizontal profile and Gaussian fit at the peak of the measured spatial distribution for two Schottky Barrier Diode detectors.

diffraction effects.

As the waist location is unknown and the detectors produce a signal from an incident polychromatic beam, we cannot fit the measured widths to equation 4.20, which is wavelength dependant. In addition, the beam waist sizes (also dependant on λ) are unknown. We can, however, calculate the angular divergence of the beam through simple geometry. The measured widths were fitted to a straight line, from which the total change in beam width $\Delta\omega$ over the longitudinal position range Δz was found. From this, the half-angular divergence is simply obtained as $\tan^{-1}(\Delta\omega/\Delta z)$. From the measured widths, the half-angular divergences for the 60-90 GHz and 220-330 GHz distributions were found to be $\theta_1 = 0.050 \pm 0.003$ rad and $\theta_2 = 0.047 \pm 0.002$ rad respectively.

Rewriting equation 4.22 as $\omega_0(\lambda) = \frac{\lambda}{\theta\pi}$, we can then use the angular divergence to calculate the beam waist size for a given wavelength. To calculate the beam distribution, we can use the equation for the intensity of the beam, as given in 4.23.

$$I(r, z, \lambda) = I_0 \left(\frac{\omega_0(\lambda)}{\omega(z, \lambda)} \right)^2 e^{\left(\frac{-2r^2}{\omega^2(z,\lambda)} \right)} \tag{4.23}$$

where $I_0 = I(0, 0, \lambda)$ is the intensity at the centre of the beam waist. As we measure the intensity over a finite bandwidth, we can write:

$$I(r, z) = \int_{\lambda_1}^{\lambda_2} I(r, z, \lambda) d\lambda \tag{4.24}$$

where λ_1 and λ_2 are the shortest and longest detectable wavelength respectively. By

calculating the intensity $I(r, z)$ over a given range of longitudinal and radial distances, we can then calculate the beam width as a function of longitudinal position by searching for the radial position corresponding to $I(0, z)/e^2$. As we have the measured widths at an unknown distance, we can match these to the calculated widths to obtain their longitudinal position. This process was applied to the horizontal distributions from both detectors. The calculated distribution in the 60-90 GHz range is shown in figure 4.25(a), with the corresponding beam widths and measured data for both detectors being shown in figure 4.25(b).

As expected, the 220-330 GHz detector has a smaller waist size than the 60-90 GHz detector. There is however a notable discrepancy in the distance from the waist position to the closest scan position, the 60-90 GHz being 1.76m and the 220-330 GHz being 1.88 m. The transfer line between the initial emission and the viewport acts as a waveguide with varying geometry throughout, therefore analysis of the waist position for a given frequency becomes extremely complicated. As such, the waist positions calculated here should be thought of as a virtual waist. A more accurate measurement could be accomplished by either additional scans over a larger range of longitudinal positions or using a narrower bandwidth detector such that the measured distribution is nearly monochromatic.

Prior to the installation of the interferometer system, the longitudinal stage was positioned much closer to the viewport window. Distribution scans were recorded from 200 high current bunches in low alpha operation, over a large range of longitudinal distances from the viewport. Example scans were recorded by the 60-90 GHz detector over a 500 mm separation distance, with example results shown in figure 4.26.

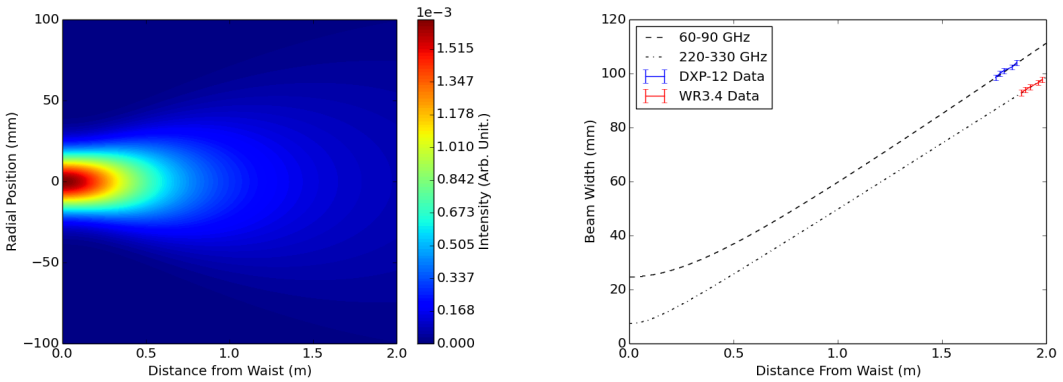

Figure 4.25: Horizontal radiation spatial distribution in the 60-90 GHz range (a) and corresponding beam widths plus measured sample widths from two Schottky Barrier Diode detectors (b).

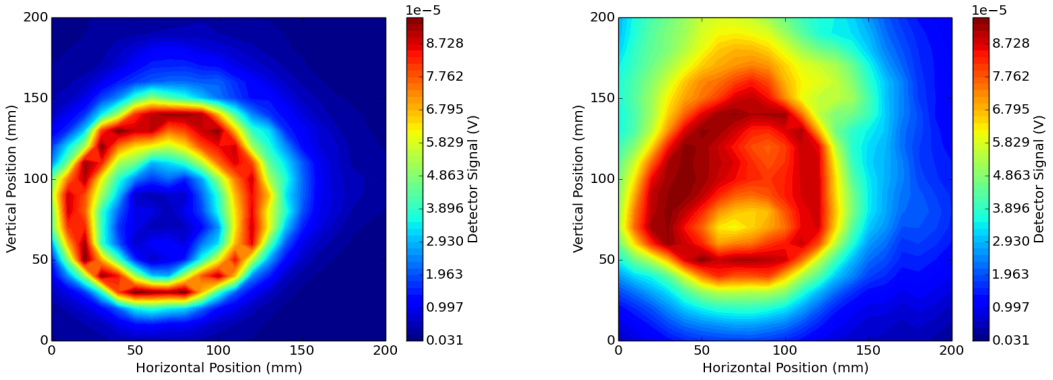

Figure 4.26: 2D scans of radiation distribution from the mm-wave port at Diamond light source for a close (a) and far (b) distance to the viewport.

Unusually, at the close longitudinal position, a ring-shaped pattern was observed with an apparent minima in the centre of the distribution. Moving the detector away by 500 mm, however, revealed the presence of signal inside of the measured ring distribution. Although the centre does not fully increase in magnitude above the voltage recorded from the ring, it exhibits a closer resemblance to the distributions in figure 4.23. Given the high current and the proximity of the scan in figure 4.26(a) to the viewport, it is believed that the detector is saturating. Moving the detector further away allows for the distribution to diverge and the power density to decrease to detectable levels. The necessary inclusion of the actuator controlled mirror with the interferometer installation requires the movement of the stage system away from the viewport, therefore reducing the potential to saturate the detectors. The long path length through the interferometer prevents detector saturation of either the pyroelectric or quasi-optical detectors.

Whilst the plotted radiation spatial distribution allows us to normalise any signals to detector position, as it is the measure of the integrated spectrum over the detector bandwidth, the power spectrum is still effectively unknown. The detectors' inability to distinguish wavelengths from a polychromatic beam means spectroscopic techniques must be applied to measure higher resolution spectral information.

4.9.1 System Optics

With the known spatial distribution of the beam, the effect of the beam divergence on the measurable spectrum must be considered. Following the geometry as described in section 4.9, the power of an incident beam of wavelength λ measured within a circle in radius r

at a longitudinal position z can be written as [129]

$$P(r, z, \lambda) = P_0(\lambda) \left[1 - e^{\left(-\frac{2r^2}{\omega(z,\lambda)^2}\right)}\right], \tag{4.25}$$

where $P_0(\lambda)$ is the total power in a disk of infinite radius at $z = 0$. The initial power can be calculated in terms of beam waist $\omega_0(\lambda)$ and on-axis intensity $I_0(\lambda)$ from equation 4.23 as

$$P_0 = \frac{1}{2}\pi I_0 \omega_0^2. \tag{4.26}$$

The emitted coherent power spectrum from equation 2.19 can be used as our initial power $P_0(\lambda)$, however the variation of waist size and intensity with wavelength is unknown. The spatial distribution measurements in section 4.9 have provided a half-angular divergence ($\theta(\omega)$) in two bandwidths, from which the corresponding waists are calculated using equation 4.22. As the two measured angles are close and agree within error, by assuming θ is approximately constant for long wavelengths, we can estimate $\omega_0(\lambda)$ as directly proportional to wavelength.

The known waist size allows us to calculate the beam width at any position of z, and consequently the power distribution, $P(r, z, \lambda)$. The measurements presented in section 4.9 have additionally shown that the beam widths at a longitudinal position of around ~ 1.8

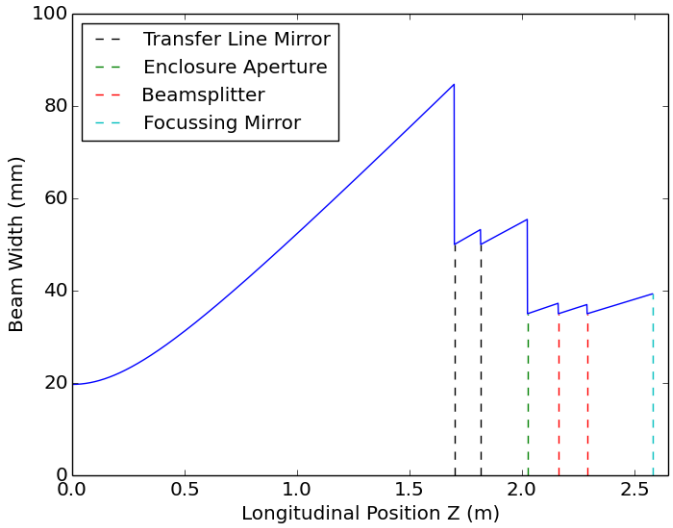

Figure 4.27: Width of a 3 mm wavelength Gaussian beam propagating from beam waist to focussing mirror in the interferometer.

metres are larger than the mirrors in the transfer line, interferometer enclosure entry aperture and the silicon beamsplitter, all off which are located further along the direction of propagation whereupon the beam is wider still. As the beam continues to propagate and diverge, a fraction of the beam is lost at each of the aforementioned locations. An illustration of this divergence effect is shown in figure 4.27 where the width of a beam of 3 mm wavelength is shown over its propagation from beam waist to the focussing mirror. It should be noted at this point that this is a simplified model. Following the first clipping of the beam by the mirror, the beam no longer remains Gaussian. As subsequent clips of the beam become very difficult to model, the beam was treated as if it continued to propagate as a Gaussian beam to simply demonstrate the loss in power at longer wavelengths, the author acknowledges that the final spectrum at the detector will be different to that calculated here.

To calculate this effect, we assume the mirrors and beamsplitter act as infinitely thin apertures positioned sequentially along a single axis. As such, the effect from the beamsplitter must be included twice to incorporate losses at both the splitting and recombining stages. Where the beam propagates through an aperture of radius a such that $\frac{\omega(z,\lambda)}{a} = F_\omega$, it is assumed that the beam diverges at the same rate, but continues propagating at this fractional width $\frac{\omega(z,\lambda)}{F_\omega}$. The divergence of the beam within the interferometer is sufficiently small to not be appreciably affected by the interferometer arms' flat mirrors, which have a larger radius than the beamsplitter, therefore they are ignored. It is also assumed that the movable arm of the interferometer is at the point of zero path difference.

As the beam size at a given longitudinal position is wider for longer wavelengths, a greater fraction of the spectral power is lost compared to the shorter wavelengths, consequently affecting the measurable power spectrum. The fraction of power transmitted through an aperture can be obtained using equation 4.25, however the input power P_0 must be modified after each aperture to incorporate every loss along the path of propagation. The spectral power transmitted through each sequential aperture is shown in figure 4.28, where it can be clearly seen that the divergence significantly affects the power spectrum.

The fits to the measured distributions in section 4.9 result in a varying distance to the beam waist. Taking this variation as an error in the distance between the beam waist and the first mirror in the transfer line, after passing through all the effective apertures the spectral power integrated up to 750 GHz is 3.02 $\pm$ 0.09 % of the original emitted

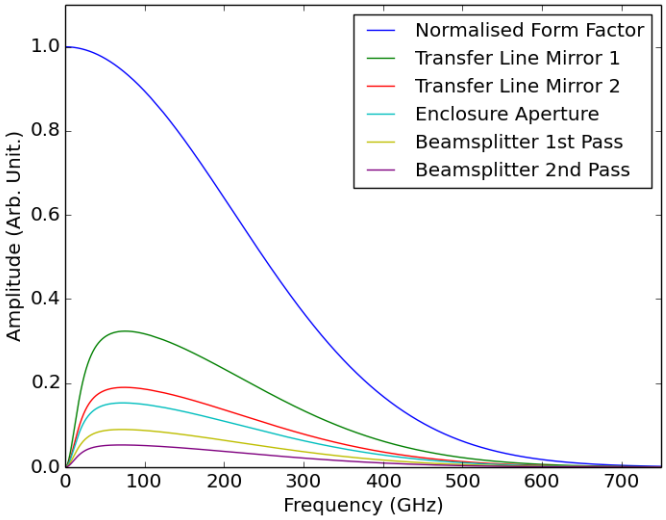

Figure 4.28: Spectral power transmitted through sequential apertures representing components in the transfer line and interferometer.

spectrum integrated across the same bandwidth.

After propagation through the final effective aperture, the beam is focused onto the detector by the parabolic mirror. This can be modelled as a thin lens with focal length f, sat at a distance Z_0 from the initial beam waist of radius ω_0, which focuses the beam to form an image at distance Z_1 with a beam waist of radius ω_1, as shown in figure 4.29.

If we assume the incident beam has a spherical wavefront, the radius of curvature, given by equation 4.27, must be equal for both the incident and reflected beams at the lens.

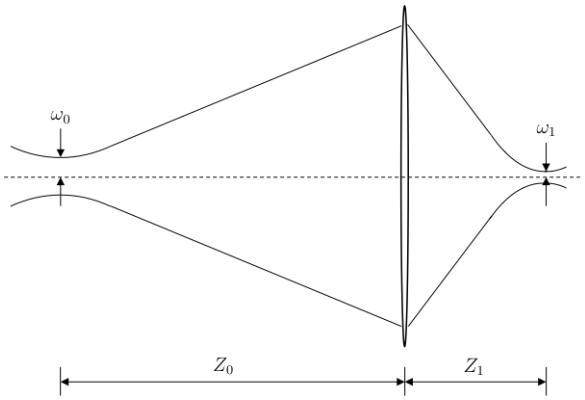

Figure 4.29: Diagram of paraxial Gaussian beams focused by a thin lens.

$$R_N(z,\lambda) = z\left[1+\left(\frac{\pi\omega_N^2}{\lambda z}\right)^2\right] \tag{4.27}$$

From the thin lens equation, we can write

$$\frac{1}{f} = \frac{1}{z_0\left[1+\left(\frac{\pi\omega_0^2}{\lambda z_0}\right)^2\right]} + \frac{1}{z_1\left[1+\left(\frac{\pi\omega_1^2}{\lambda z_1}\right)^2\right]}. \tag{4.28}$$

Rearranging equation 4.28, we can calculate the waist size and longitudinal position of the focused beam. As the virtual waist varies in position depending on wavelength, the focused waist position z_1 will also vary with wavelength. Longer wavelengths will once again have a waist larger than that of short wavelengths, therefore when calculating the power in a disk of radius equal to that of the detector lens (5 mm), we observe further power losses in the longer wavelengths as shown in figure 4.30.

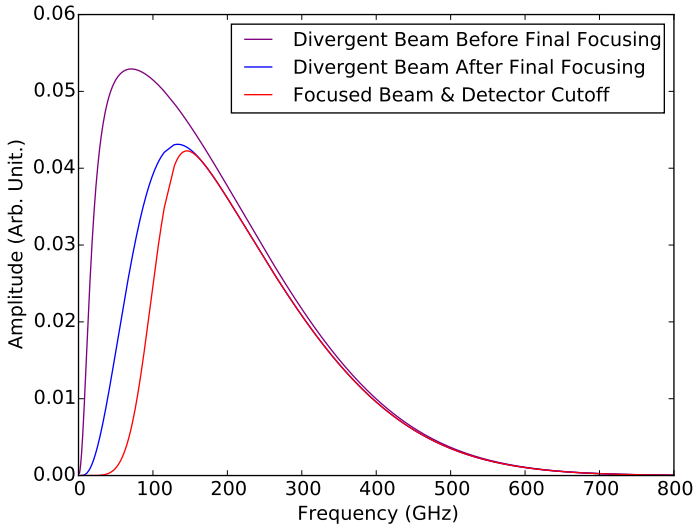

Figure 4.30: Spectral power of the beam focused by a thin lens, measured in a 5 mm radius disk in the focal plane with detector low frequency cutoff effect.

In addition to the divergence effect, we must also include a function that approximates the low frequency cutoff of the detector. The detector is sensitive below its stated 100 GHz limit, as evidenced by the detected signal whilst aligning the interferometer in section 4.8, however, without knowing the exact response curve of the detector, we assume that the sensitivity decreases significantly below its quoted lower limit. To approximate the detector cutoff, we apply an analytical function initially proposed in [128] for a detector with circular aperture. The function is given in equation 4.29, where ω_{cut} is the

characteristic cutoff frequency.

$$f(\omega) = 1 - e^{-\left(\frac{\omega}{\omega_{cut}}\right)^4} \tag{4.29}$$

Although the cutoff in [128] is diffraction based, we propose to apply the same function for the quasi-optical detector sensitivity, however it is accepted that this is only an arbitrary estimate until the quasi-optical detector can be fully characterised. The final power spectrum is shown in red in figure 4.30. The spectral power of this final curve integrated up to 750 GHz is 0.82 ± 0.08 % of the emitted spectrum integrated over the same spectral range. Integrating the bunch spectrum in figure 2.5 between 0 and 750 GHz gives a total emitted power in that bandwidth of $\sim$ 0.25 mW, therefore the maximum power we can expect to detect is 2.05 ± 0.20 μW s^{-1} rad^{-1}, which is well above the noise floor of the detector.

4.10 Summary

This chapter has described the experimental setup at Diamond Light Source for the purpose of investigating the microbunching instability. An overview of the Diamond storage ring has been given, including its operational parameters for three modes; the standard mode most commonly available to users, and two low alpha modes. The transfer line from the dedicated mm-wave viewport was described, as well as the system for spatially measuring the distribution of radiation. The components of the Michelson Interferometer were explained, including the various detectors used, and the corresponding data acquisition system used in the experiments. Where possible, the optical properties of system and its components were analysed regarding their effect on any incident spectrum.

Chapter 5

Observations of the Microbunching Instability at Diamond Light Source

This chapter discusses the measurements of the coherent synchrotron radiation and microbunching instability at Diamond Light Source using the setups as described in chapter 4. It describes the initial results from experiments to detect the microbunching instability, as well as an analysis into the current threshold of the instability's onset, after which, results from the interferometric system are described along with the corresponding spectrum.

5.1 Instability Detection

The initial measurements in the investigation into the microbunching instability were simple detection experiments; primarily to verify the presence of the instability, but also to learn the machine conditions necessary to create and drive the instability to better understand its behaviour. These measurements were made at the shared diagnostic viewport, the setup for which is described at the beginning of section 4.2. For these experiments, the storage ring was set with a single bunch fill pattern to ensure measurements were made of the same bunch, but also to avoid any potential bunch-bunch wakefield interactions.

To show that these detectors have a fast response and are capable of measuring signal on a turn-by-turn basis, a signal from the 60-90 GHz (DXP-12) Schottky Barrier Diode (SBD) detector was recorded every 125 ps for 1 ms from a high current bunch. To record a sufficiently high resolution measurement, rather than recording with the signal analyser, the 60-90 GHz detector was briefly connected to a 13 GHz bandwidth oscilloscope from

Agilent. An interpolated 4 ns example of a single shot is shown in figure 5.1. Though physically limited by the temporal resolution of the signal, the interpolation is necessary to provide a more accurate representation of the detector response time. Taking the response time of the detector as the FWHM of the signal, then by searching either side for $V_{peak}/2$ and calculating the time difference between these two points yields an FWHM time of $\sim$ 360 ps. Given our resolution, the detector response time is therefore 375 ps. The $<$ 1 ns response time as quoted in section 4.5.2 is therefore experimentally confirmed. To calculate a more accurate response time would require a higher sampling rate which is currently beyond the capabilities of the current DAQ system.

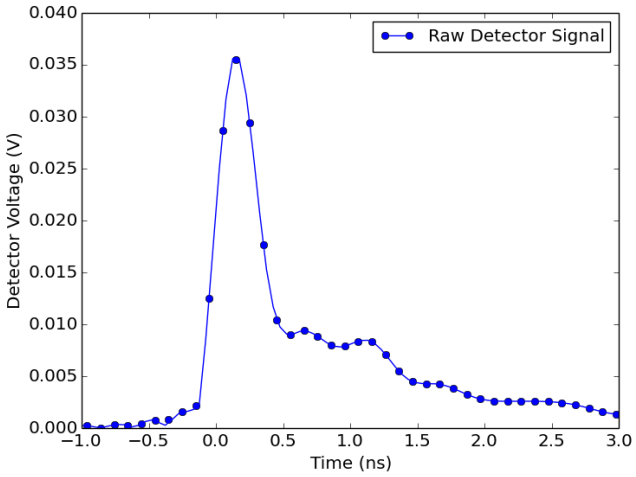

Figure 5.1: A typical signal from the DXP-12 detector from a single bunch.

The whole 1 ms time sample is shown in figure 5.2. As one can see, there are large fluctuations in the detector signal over the $\sim$ 500 revolutions during which the data was acquired, the observed behaviour agreeing with previous experiments at Diamond [41], as well as previous literature on some of the first observations of the instability, such as [50] which describes the bursts as being quasi-periodical, with the periodicity varying with current. The bunched beam theory in section 2.3.2 describes the instability growing and then damping due to an increase in bunch length over a couple of synchrotron periods. Whilst we cannot infer the bunch length from the data here, from Diamond's synchrotron frequency in standard optics as given in table 4.1, two synchrotron periods would be approximate 0.8 ms, meaning the measurement matches the theoretical behaviour.

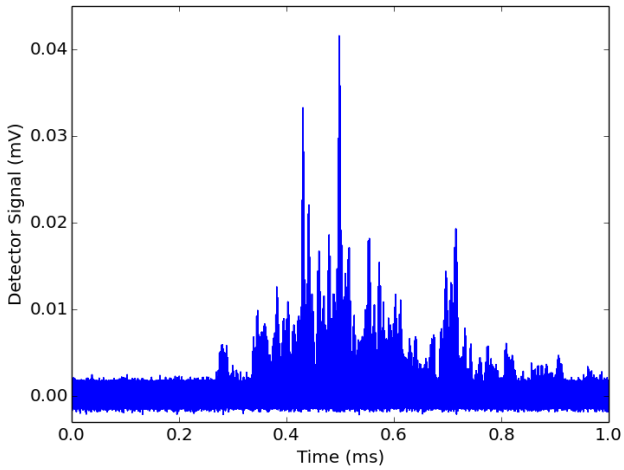

Figure 5.2: A 1 ms example of signal acquired from the DXP-12 detector from a single bursting bunch.

5.1.1 Beam Modulation Frequency Spectrum

Whilst this signal for a constant bunch current shows an irregular pattern which can be attributed to the presence of the microbunching instability, it does not reveal information regarding the instability threshold or detail about any sub-structure in the bunch's longitudinal charge distribution. Moreover, the signal evolution demonstrates that the longitudinal bunch structure evolves quite rapidly such that different fractions of the bunch emit radiation coherently at any given time. As such, a further investigation was conducted whereupon the signal was recorded using the original spectrum analyser over a bunch current range so the instability's threshold current and evolutionary behaviour could be observed. The large amount of data that would be acquired by sampling every 125 ps is highly impractical given the aim of the project, therefore the sampling was limited to every 25 μs for 0.5 seconds. This was repeated every few seconds for several minutes whilst the beam current decayed.

Despite the investigation focusing on the instability's threshold current, the operational constraints of the machine to inject small numbers of electrons to provide a small current increase proved troublesome, notably that a charge injection causes additional motion within the bunch, resulting in a distortion to the measured signal. This would be problematic due to the difficulty in distinguishing the added injection signal from bursts as a result of the instability. Whilst this motion would eventually damp out, it would still take time after every injection to reach the point of instability dominated signal. Consequently,

a bunch was injected at a high current of approximately 5 mA and signal recorded as the bunch decayed. Due to the long decay half-life of the bunch (usually around 2 hours), horizontal collimators were used to scrape the beam and artificially decrease the decay half life to approximately 15 minutes, providing a current resolution of approximately 5 μA. To keep the decay rate quasi-linear, several alterations were made to the collimators position throughout the experiment. The theory described in chapter 2 shows that for the models, the threshold of the instability depends (amongst other machine parameters) on the RF cavity voltage. Therefore these experiments additionally investigated variations in the RF voltage.

Applying a Fast Fourier Transform (FFT) to a signal such as that in figure 5.2, one may derive a bunch modulation frequency spectrum. Figure 5.3 show the beam modulation frequency spectrum versus bunch current obtained from the 60 - 90 GHz SBD detector, for a 3.5 MV RF voltage. As the detected signal is from a single bunch, the corresponding spectra are modulated to the revolution frequency of 533 kHz. This also provides the benefit that the detectors will not noticeably suffer from 1/f noise, which the Schottky diodes do produce, however, given that the noise equivalent power is given in

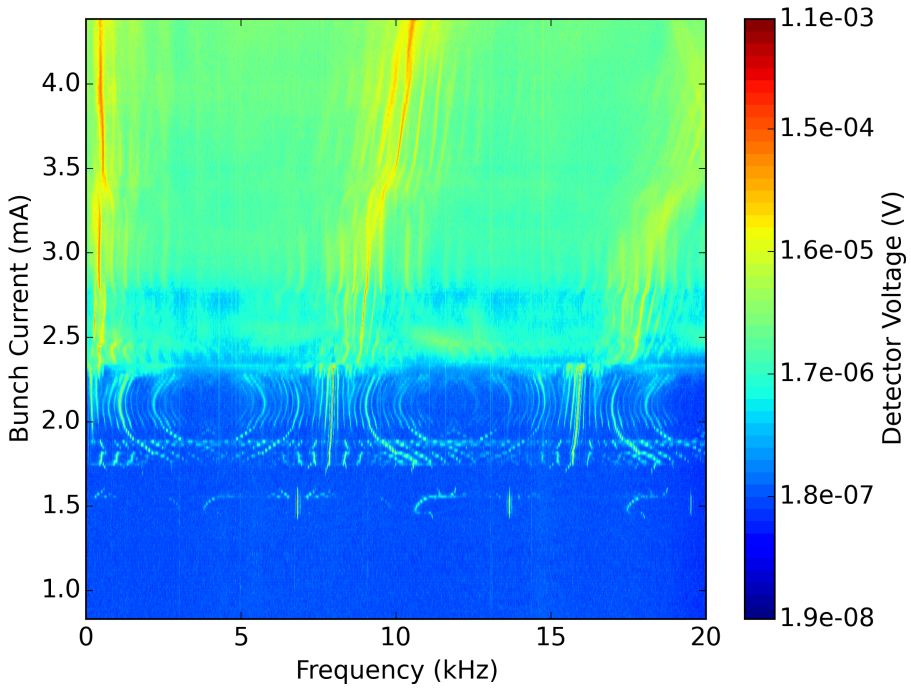

Figure 5.3: Example modulation spectrum from an amplified 60-90 GHz Schottky Barrier Diode detector as a function of bunch current for a 3.5 MV RF voltage, with 0 kHz corresponding to the bunch revolution frequency.

its data sheet at 1 kHz, at the revolution frequency, the data should not be noticeably affected. The x-axis on the displayed spectrum in figure 5.3 are therefore adjusted such that 0 kHz correspond to the revolution frequency. Note that the signal at the revolution frequency is not shown due to its large amplitude relative to the remainder of the modulation spectrum. The current range over which the data were recorded varies due to the decay lifetime and limited buffer size of the signal analyser; the low-current point at which the experiments were stopped were selected such that the instability no longer appeared below threshold, whilst maintaining the interesting high current features in the memory buffer. The threshold current in all the measurements was taken to be where the sidebands around the revolution frequency first appear.

The onset of the instability manifests as sidebands around the revolution frequency, and with further current increases, these sidebands drift to higher frequencies whereupon they begin to develop sidebands themselves. Further increases in current leads to a sudden jump, where the average detector signal increases, in some cases by an order of magnitude. Greater spectral detail is shown for six current values and their time domain signals in figure 5.4. There are significant differences in signal, notably in its amplitude and periodicity. Whilst at threshold there is an overall signal increase with no discernible pattern, the signal becomes quasi-periodic as the current increases and the sidebands appear. A further current increase leads to sharp time domain peaks occurring, exhibiting similar behaviour on a similar timescale to that displayed in figure 5.2. Despite a small difference in burst length and periodicity which can be attributed to the difference in bunch current, these type of bursts appear in regular intervals. The bursting eventually appears to be emitted chaotically, as seen in the bottom right image (at 4.210 mA). The observed behaviour is consistent with previous literature as outlined in section 1.4.

In addition to the measurements at 3.5 MV, the same procedure was repeated for RF voltages of 2.0, 2.5, and 3.0 MV, shown in figure 5.5. Whilst most of the observed the effects are present for all 4 measurements, the bunch current at which these features occur differs with RF voltage. The increase in RF voltage leads to these features becoming increasingly prominent; in particular the sidebands that appear after threshold appear to ‘drift’, causing the circular effect. Also apparent are sudden discontinuities; regions where increasing current causes the coherent bursts to subside. An example of this in figure 5.3 is where the coherent emissions begin at 1.42 mA, however very little is observed between 1.6 and 1.75 mA.

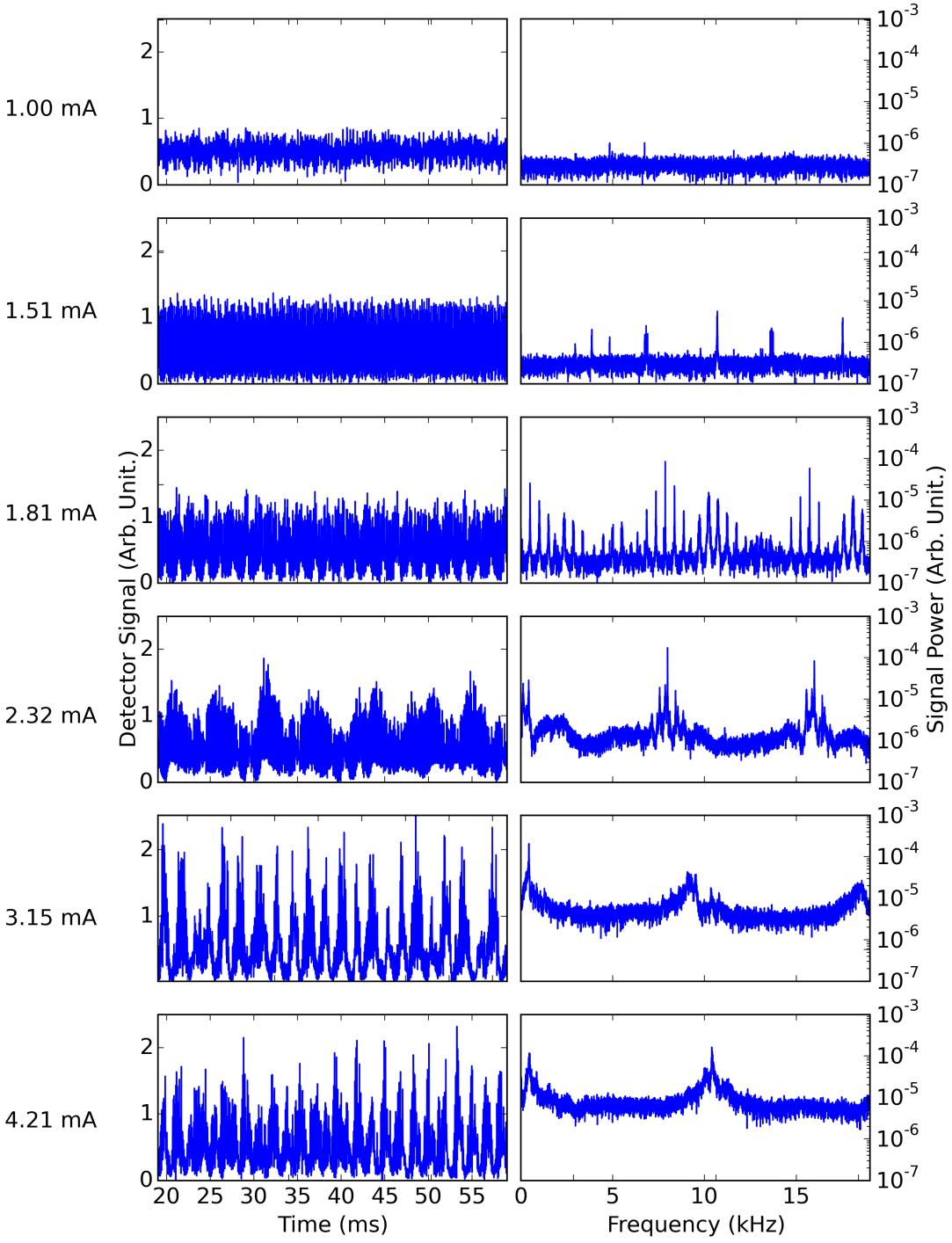

Figure 5.4: Slices of figure 5.3 in the frequency and time domains showing the onset and evolution of the instability for an RF voltage of 3.5 MV.

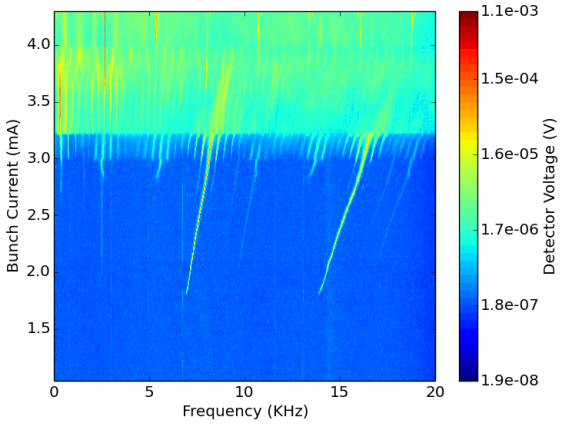

(a) 2.0 MV

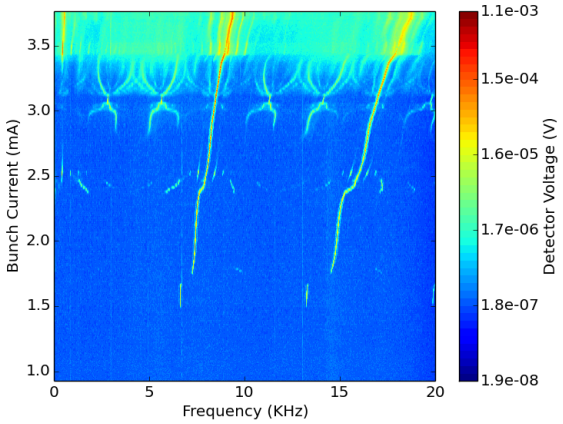

(b) 2.5 MV

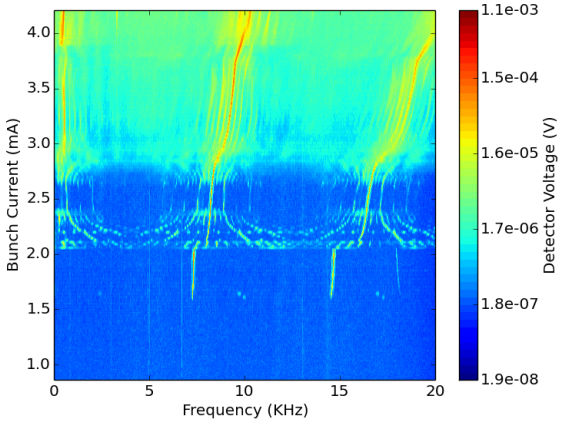

(c) 3.0 MV

Figure 5.5: Example modulation spectra from an amplified 60-90 GHz Schottky Barrier Diode detector as a function of bunch current for different RF voltages, with 0 kHz corresponding to the bunch revolution frequency.

As one may recall, a second SBD detector was additionally installed at the same location, operating in the higher frequency range of 220-330 GHz (WR3.4ZBD). The modulation spectrum from this detector is shown in figure 5.6 along with the spectrum at a bunch current of 4.38 mA. As the detector was unamplified, the resulting spectrum is substantially weaker, as is evident by the mean signal being over two orders of magnitude smaller than the equivalent bunch current signal from the first detector. The signal is observed up to 2 kHz, but only above 2.5 mA where the instability has reached the chaotic regime. The lack of signal at lower currents is believed to be due to a lack of amplification.

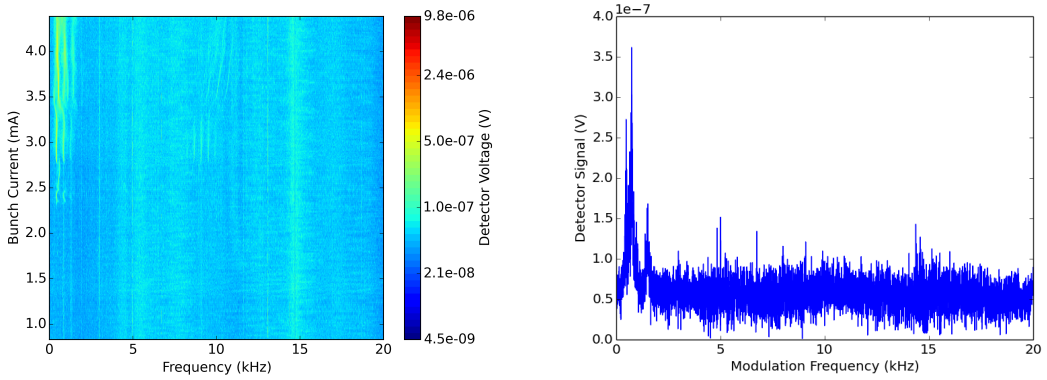

(a) (b)

Figure 5.6: Modulation spectrum from an unamplified 220-330 GHz Schottky Barrier Diode detector, with 0 kHz corresponding to the bunch revolution frequency, from a single bursting bunch for: (a) increasing bunch current, and (b), a single current of 4.38 mA.

5.1.2 Long Term and Short Term Reproducibility

Following a gap of a few months between experimentation time, repeats of the experiments recording the modulation spectrum were conducted for varying RF voltage. This was primarily to gather further data on the instability threshold but also to investigate the long and short term reproducibility of the phenomenon, and to test if the initial method of scraping the beam to reduce the current, which we know would act as an impedance, had been a significant contributor to the instability observations. Once again, only one amplifier was available, so the results shown in figure 5.7 are from the 60-90 GHz detector. The instability threshold's dependence on RF voltage was once again investigated. The signal is modulated to the revolution frequency, thus the x-axis is shifted as before. The long acquisition time necessary to achieve the same current resolution as the previous experiments became problematic. As such, the experiments varying RF voltage were

conducted for a single bunch injected at low current, after which the current was increased incrementally in steps of approximately 50 μA, after which sufficient time was allowed to allow the injection motion to damp. After the measurements were recorded at high current, the beam was dumped and re-injected at low current. The first two measurements of the repeat test at 3.5 MV followed the same procedure of injecting incrementally, however for direct comparison with the results shown in figure 5.3, following the second recording, the final measurement in figure 5.7 was recorded by collimating the beam, decreasing the decay half life.

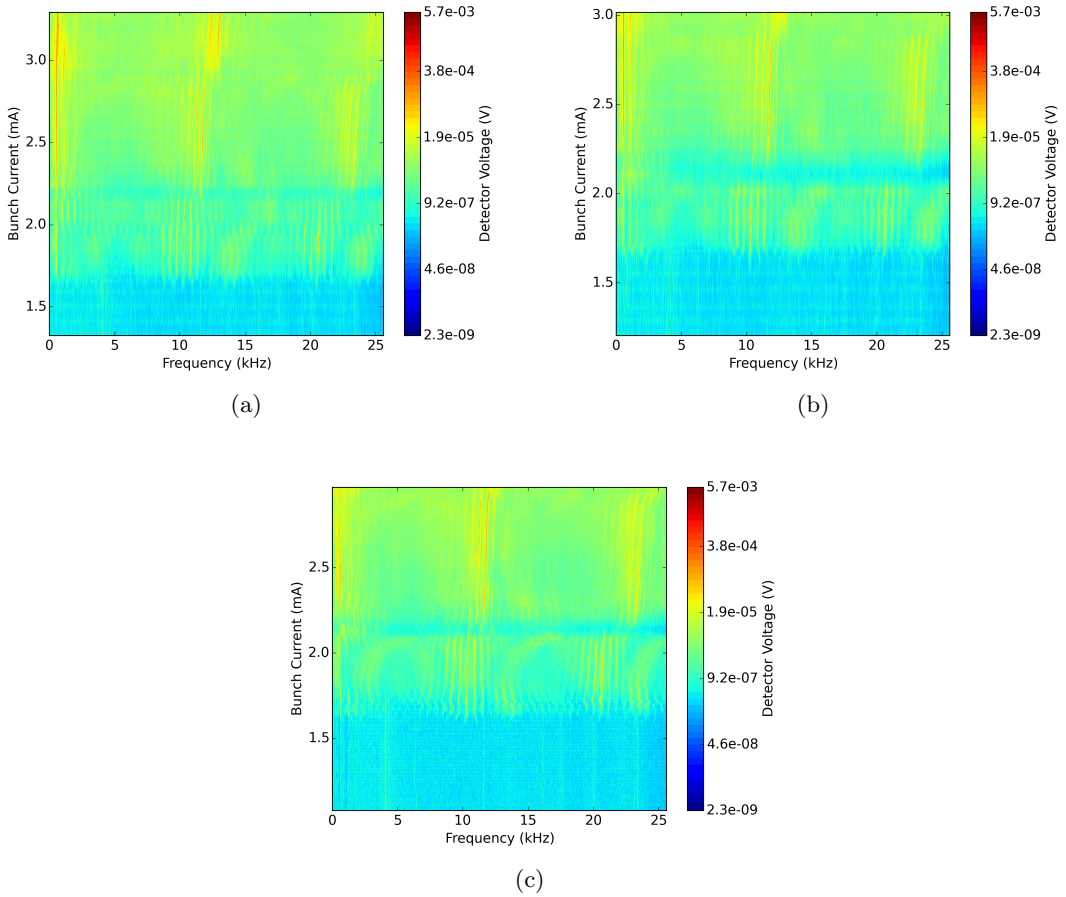

Figure 5.7: Repeated spectral scans, with 0 kHz corresponding to the bunch revolution frequency, for an RF voltages of 3.5 MV for current increments by injection (a) and (b), and current decrements by collimator scraping (c).

The three repeat measurements at 3.5 MV are shown in figure 5.7. The observed results are similar to that in figure 5.3, with sidebands around the modulation frequency present at low current, followed by the additional sidebands and later a jump to stronger bursting with an overall signal increase. As the current resolution is reduced by approx-

imately a factor of 10, the recorded spectra is consequently less detailed. Although not shown here, similar behaviour is exhibited in the measurements at lower RF voltage. The threshold current of these scans is discussed further in section 5.2. The dynamic range of the detector signal is additionally similar to that of the earlier detection experiments. The three separate measurements in figure 5.7 display good agreement with one another, displaying similar spectral features, and having near-identical thresholds. The similarities in the recorded modulation spectrum suggest that the bursting periodicity is a repeatable phenomenon provided machine conditions do not vary on the short term. Additionally, the use of the collimators to scrape the beam appears to have little effect on the instability's threshold current or evolutionary behaviour. As they do differ from the initial measurements, it suggests that the long term behaviour of the start up does depend on the initial settings and tuning of the machine at the start up.

5.1.3 Instability Investigation at a Dedicated Viewport

Following the relocation of the detectors to the dedicated mm-wave viewport, an additional set of modulation spectrum scans were measured. The measurements were once again from a single bunch, recorded with the SBD detectors, however both detectors were amplified throughout these tests. The 3D stage system to which the detectors were attached was positioned such that equal signal amplitude was observed in both detectors. An example modulation spectrum from both detectors at a 3.0 MV RF voltage is shown in figure 5.8.

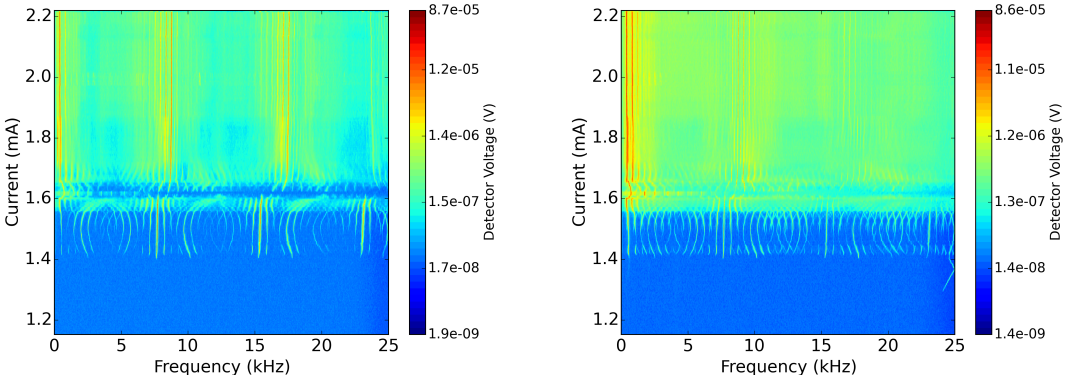

Figure 5.8: Example modulation spectra as a function of current, with 0 kHz corresponding to the bunch revolution frequency, for a single bunch with 3.0 MV RF voltage, measured by detectors in frequency bands of 60-90 GHz (a), and 220-330 GHz (b).

The signal from the two detectors display some agreement with one another particularly the threshold current, however there are differences, most notably immediately after the onset of the instability. The sidebands which form the circular effect appear more prominent in the 220-330 GHz detector in this quasi-periodic regime. As the two detectors are very similar in construction and performance, the observed differences in signal in figure 5.8 are unlikely to be a result of the detector, therefore the results can be attributed to a variation in the spectrum emitted from the bunch.

5.1.4 Bunch Current Dependence

Despite the clear differences, all three sets of measurements exhibit similar behaviour, indicating that the instability is a potentially repeatable phenomenon. The highly similar spectra shown in figure 5.7 additionally suggests that it is reproducible over a short time period, and thus is an effect of the machine conditions. Using the data collected thus far, it is possible to show instability is proportionality to bunch current. Formula 2.14 shows that the coherent part of the emitted spectrum is proportional to N^2, however, this is assumed to be for a non-bursting bunch.

The signal at revolution frequency was taken from the first set of modulation spectra from the 60-90 GHz detector, for four different RF voltages. For this test of dependence, the initial measurements from section 5.1.1 were used as they provided the highest current resolution. Below the instability threshold for each voltage, the signal was fitted to the formula $y = Ax^B + C$ using a least square fit. The four signals with their fits are shown in figure 5.9. The author acknowledges that these 4 signals do not display an error, this arises from only having one measurement of these modulation spectra at a given RF voltage for these machine conditions, with variations in machine conditions between the recording of each data set meaning they cannot be used together. The numerical result along with the reduced χ^2 of each fit is shown in table 5.1.

The mean of the power scaling parameter B from all 4 fits means that the data scales as $y = Ax^{1.96\pm0.09} + C$, confirming that the coherent signal is proportional to N^2 as expected. The difference in the scaling coefficient A can be explained by the RF voltage difference between the experiments. A higher RF voltage will squeeze the bunch and reduce its length, which consequently broadens the form factor of the coherent radiation to shorter wavelengths, thus changing the proportionality of the coherent radiation intensity.

Above threshold, it is clear that the signals do not follow the N^2 dependence; the

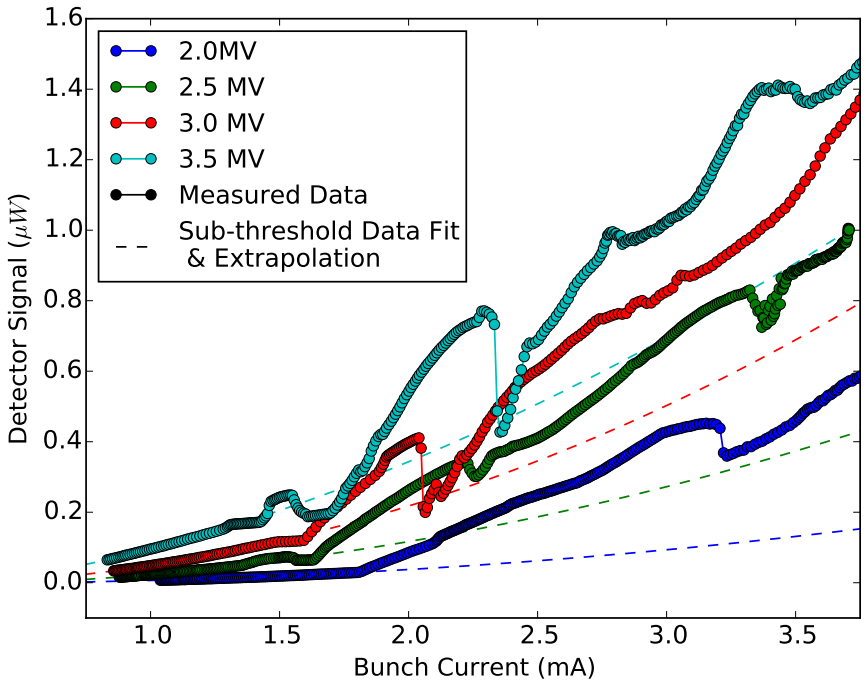

Figure 5.9: Single bunch current dependence of the signal from a 60-90 GHz Schottky Barrier diode detector, from below the instability threshold current to the chaotic bursting regime.

bursts emitted as a result of the microbunching instability demonstrate a higher energy loss by the beam. The fit was not applied to the data above threshold as the large variation in signal would (impractically) result in a large fit error. Whilst the dominant effect is dense microbunching which is seen as the large increase in signal above coherence, some regions exhibit a decrease in intensity such that the average signal falls below the coherent signal. This occurs due to bunch lengthening, moving the bunch away from the instability condition into an equilibrium distribution. In general, however, the intensity surpasses the simple coherent signal, with the chaotic nature of the signal at high current demonstrating that the microstructure of the bunch evolves chaotically.

RV Voltage	**A**	**B**	**C**	χ^2
2.0 MV	8.9e-3 ± 0.2e-3	2.15 ± 0.03	2.5e-3 ± 0.2e-3	0.2054
2.5 MV	31.8e-3 ± 0.7e-3	1.96 ± 0.04	8.6e-3 ± 0.7e-3	0.5146
3.0 MV	55.2e-3 ± 0.4e-3	2.02 ± 0.01	6.8e-3± 0.4e-3	0.0418
3.5 MV	112.3e-3 ± 4.9e-3	1.68 ± 0.06	17.2e-3± 4.8e-3	0.1234

Table 5.1: Fit parameters to the sub-threshold signal at revolution frequency for 4 different RF voltages.

5.2 Microbunching Instability Threshold

As the RF voltage has had a clear effect on the data thus far, we must also compare the instability threshold from the recorded beam modulation spectra. As discussed in section 2.3, the theory of the microbunching instability has produced formulae applicable for predicting its threshold current. The prediction depends on the bunch length, σ_z and unfortunately the bunch length measurement from the streak camera was unavailable at the time of the experiment, however they can instead be calculated. Results from a previous experiment at Diamond showed that the bunch length can be approximated by equation 5.1 for standard optics [82]. The equation was obtained from a fit to bunch length measurements for increasing current up to 2 mA at 2.5 MV RF voltage.

$$\sigma_z(ps) = 12.90 + 8.05\ {I_{bunch}}^{0.81} \tag{5.1}$$

As the above formula is for a specific RF voltage, and the bunch length is known to be proportional to $1/\sqrt{V_{rf}}$, the above equation can be rescaled appropriately for any RF voltage by multiplying by the factor $\frac{\sqrt{2.5\times10^6}}{\sqrt{V_{rf}}}$. From this, we can calculate the bunch lengths for a given current.

The instability threshold results are shown in figure 5.10 for the three sets of data, the first being the initial instability detection experiments in section 5.1.1 (triangle marker), the second being the repeat measurements in section 5.1.2 (circle marker), and the third being the measurements from the dedicated viewport in section 5.1.3 (square marker). The bunch length error arises from the error in measured cavity voltage. The threshold current error is from the current resolution in the individual experiments. The large errors in the second set are a result of the larger current resolution, with the 3.5 MV RF threshold current in this set is taken to be the average of the 3 repeated tests shown in figure 5.7. Despite the theory suggesting that the coasting beam model should be applied, the bunched beam method was found to be closer. The predictions are shown in figure 5.10 where the solid lines correspond to the free space prediction and the dashed lines correspond to the parallel plates prediction. The coasting beam predictions are not shown as they are at significantly higher current.

As the thresholds for a given RF voltage match the trend as predicted by the theory, the measured threshold means that the instability is occurring for different bunch lengths. One would also expect the threshold current to be consistent for a given RF volt-

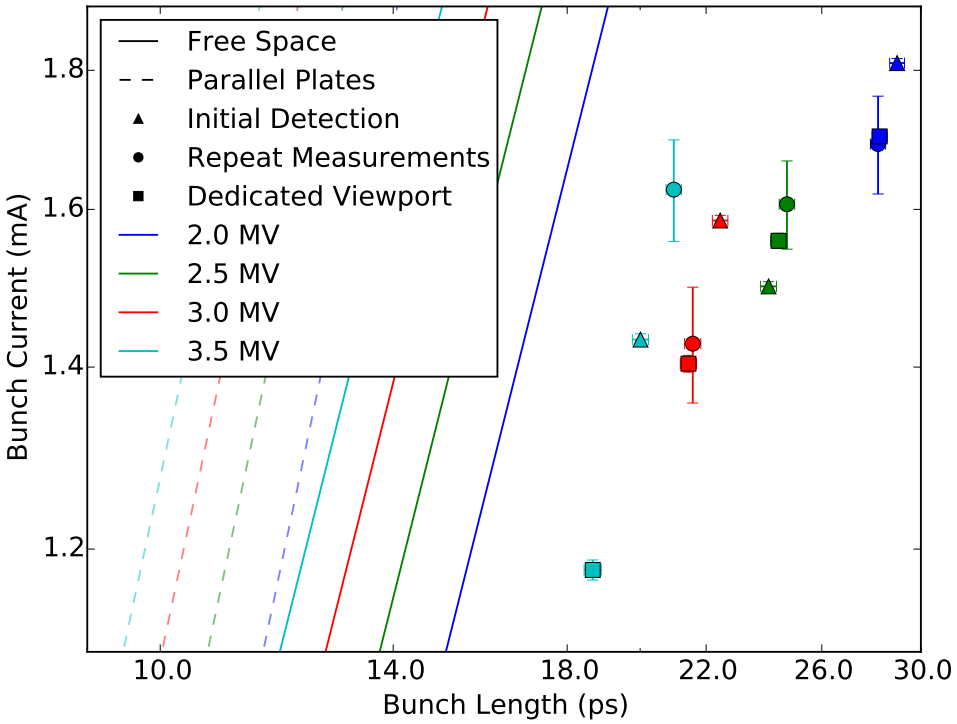

Figure 5.10: Single bunch microbunching instability measured threshold current from three sets of measurements (denoted by marker) for 4 RF voltages (denoted by colour), with comparison to theoretical predictions (solid/dashed line).

age, however this does not occur. Given that the threshold current prediction is directly proportional to V_{rf}, despite the decrease in bunch length with increasing RF voltage, it is expected that an increase in RF voltage should decrease the current threshold. This behaviour, however, is only observed in the new viewport measurements (square marker), with the other sets showing no discernible trend. As at least one scheduled machine shutdown period occurred between each set of measurements, machine conditions such as tune and chromaticity will have varied following each startup, suggesting that not only is the instability very susceptible to the initial machine conditions, but that the instability is affected by the transverse parameters which have changed.

Whilst the displayed results are closer to the free space model than the parallel plates for a bunched beam, neither predictions are accurate. The inconsistencies in the observed data suggest that the instability is very machine specific, and that both models are insufficient at present. As the wakefield interactions in the theoretical models are confined only to the longitudinal axis, a more detailed theory can be developed by incorporating transverse effects. Beyond the parallel plates, the shielding suppression can be extended

to cover the geometry of the whole beam pipe, however its asymmetrical shape in the bending magnets means the calculations are far from trivial. Additional effects which can be incorporated into the model include RF non-linearities, beam loading in the RF cavities, space charge interactions, and the inclusion of other instabilities as outlined in [39]. The inclusion of these effects would require a significant computational investigation and further experimental data to provide a broader source of comparison.

If we compare the spectrum from an 18 ps long non-bursting bunch at 1.7 mA to the frequency bands of the two detectors used, then we see that the coherent spectrum does not reach the lower frequency detector, as shown in figure 5.11. As a source of comparison, a typical bunch from low alpha, short pulse mode at 34.2 μA is also shown. These current values were chosen to be around the threshold current (depending on the RF voltage) for their respective modes. Only when the bunch is as short as around 3 ps does the higher frequency detector begin to see a coherent signal.

In the previous section, the bunches where the instability was observed were all longer than 18 ps and thus have and even narrower coherent spectrum, therefore the signal that we observe must be as a result of the instability causing a significant change

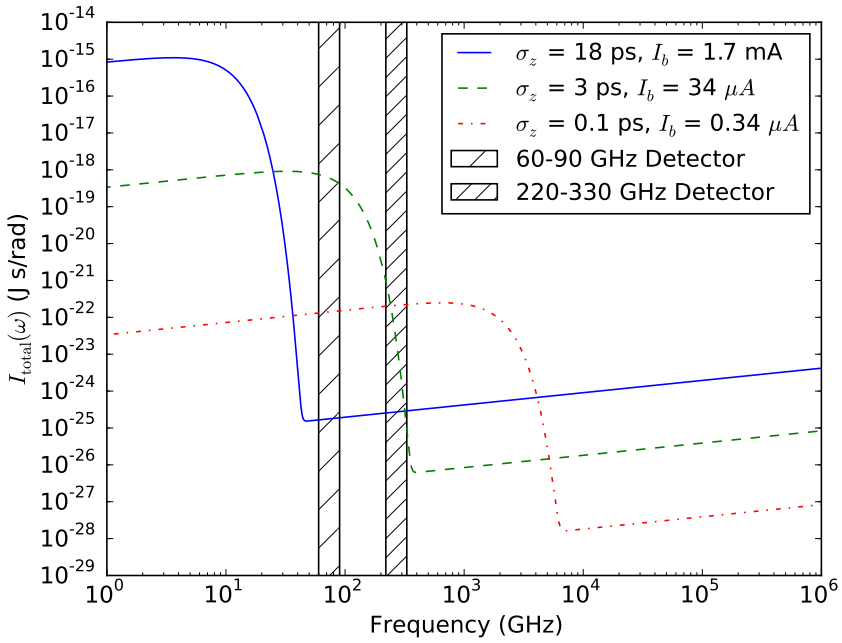

Figure 5.11: Typical spectra from a Gaussian bunch for a 18 ps (5.4 mm) long bunch at 1.7 mA, a 3 ps (0.9 mm) long bunch at 34.2 μA, and a representation of a micro bunch as a 0.1 ps (0.03 mm) bunch at 0.34 μA, with the frequency bands of two Schottky Barrier Diode detectors.

in the bunch form factor. Also shown in figure 5.11 is a short bunch of small charge as a representation of a microbunch. The instability produces many of these microbunches within its charge distribution, which will vary in size and amplitude over time. Each of these microbunches will emit a coherent spectrum, therefore many microbunches will produce coherent components which constructively interfere with one another, leading to an increase in the spectral power at shorter wavelengths than normally coherently emitted by a non-bursting bunch.

The data here thus far yields limited information regarding the instability's threshold current and evolution, however it has shown that a coherent signal exists in the 60-90 GHz and 220-330 GHz bands from an unstable bunch. It is possible that emissions with frequencies between that of the two detectors also exist, and potentially higher than the 330 GHz limit of the second detector. A significant change in spectra from a variation in beam conditions may provide an indication to the cause of the instability or aid in providing an avenue for further theoretical investigation, therefore subsequent research in this thesis focuses on the extent of these coherent emissions and observations of any spectral variations, particularly with bunch current.

5.3 Sub-Threshold Interferometer Scans

So far, the results have shown that the bunch emits bursts of coherent radiation above the threshold of the microbunching instability. Whilst it is known that this signal is dominant and exceeds the coherent emission far beyond threshold from a single bunch in standard operation, the signal from a non-bursting bunch must be taken into account in interferometric measurements. As such, scans were conducted during standard operation with a 300 mA beam in 900 bunches for both the pyroelectric and quasi-optical detector.

Scans for a 1.5 mA, non-bursting single bunch were also recorded with the quasi-optical detectors. The detector signal for these multi-bunch non-bursting tests was recorded over a large scan range, thus having high resolution but in a modest bandwidth, as explained in section 4.7. The scans were all taken using the slow method of interferometer operation. For the case such as the scans from standard operation where multiple bunches are measured, the recorded interferometric signals are normalised to the number of populated buckets. The scans shown in figure 5.12 are the average of 5 scans recorded at the same bunch current.

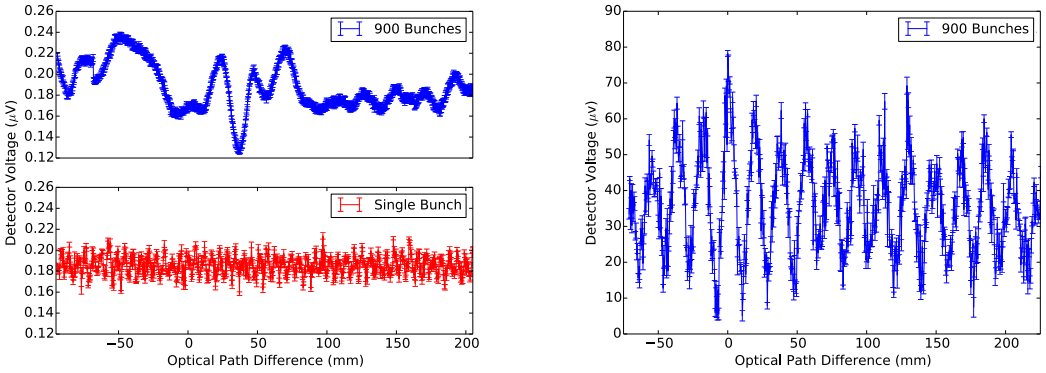

(a) Quasi-optical (b) Pyroelectric

Figure 5.12: Signal recorded using a Michelson interferometer from two detectors for standard optics.

The data recorded from the 300 mA beam from both detectors usually displays a large variation in signal throughout the entire scan range, notably in the pyroelectric signal which exhibits near monochromatic interference at a half wavelength of 9.4 mm. Similar behaviour is observed in the quasi-optical measurement though for multiple wavelengths, as shown in the resulting spectrum in figure 5.13.

As the interference is observed over the whole scan range, it cannot be a bunch emission; the coherent emissions should be localised around the point of zero optical path difference. In addition, equation 2.34 suggests a beam-pipe cutoff of approximately

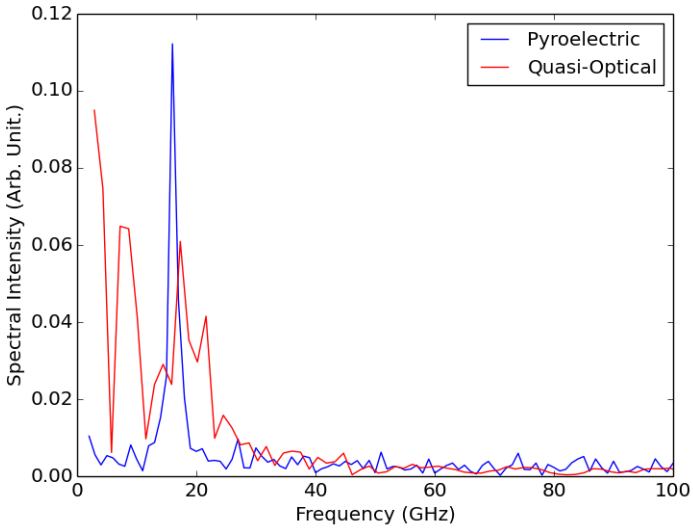

Figure 5.13: Spectrum measured by two detectors for a 300 mA beam in 900 bunches during standard operation.

5.5 mm, a significantly shorter wavelength than the observed signal in the pyroelectric measurement. The single bunch scan does not exhibit this behaviour, however, it notably does not display any interference at all. At this bunch current, the bunch will be sufficiently long to produce a similar spectrum to that shown in figure 5.11. The frequencies where coherence is seen is below the detectors' stated frequency range and also in contradiction to the beam pipe cutoff frequency, therefore we should theoretically not be observing anything but the incoherent radiation, which will only produce a DC signal in the interferogram.

The incoherent radiation, however, is several orders of magnitude lower in intensity than the coherent spectrum, whereas the detectors have recorded a signal of 0.18 μV on average which is well above both of their respective noise floors, therefore it must be detecting some incident beam. As previously suggested, the shielding cutoff from the parallel plates model may be insufficient in defining a lower frequency limit, therefore it is possible that coherent radiation is being observed.

Given the path difference range over which the effects are seen, a contribution to this may be interference from standing waves in the system. Polychromatic waves could interfere resulting in a modulated signal like that observed by the pyroelectric detector, with the detector response explaining the differences between the two detectors. Despite the absence of the signal variation in the single bunch measurements it is possible it may exhibit interference with an amplitude which is indistinguishable from the noise of the scan.

Further experimental investigation is necessary to exactly clarify the cause of these results. Altering the setup to reduce the interference effect is problematic, however given the repeatability of the scans it is possible to treat this pattern as background noise. As shown later, the intensity of the noise is more than an order of magnitude smaller which fits within our measurement uncertainty.

5.4 Coherent Interferometric Measurements and Spectra

The results displayed in section 5.1 show that two stationary detectors have observed the presence of bursts of coherent radiation between 60-90 GHz and 220-330 GHz, however the spectral content in these bands cannot be inferred from the measured data. The purpose of the Michelson interferometer is to measure the radiation emitted from a relativistic electron bunch in the magnetic field of a dipole. The recorded interferograms can then

be used to calculate the spectral content of the emissions, a necessary step in determining the bunch's form factor as outlined in section 3.1. As the interferometer has mechanical components which introduces an operational time, at this stage of the investigation into the microbunching instability, only the envelope of the form factor can be measured, as any emissions over a fast time scale will be smeared out by the integration time of the data acquisition. Difficulties were encountered in attributing spectral artefacts to specific systematic effects, as will become clear throughout this section.

This results presented in this section will discuss the recorded interferograms and their corresponding spectra from both the quasi-optical and pyroelectric detectors, for both standard and low alpha operation. During the experiments, the interferometer was scanned to within ± 15 mm around the point of zero optical path difference unless stated otherwise. Consequently, the frequency resolution is 10 GHz.

5.4.1 Spectral Measurements from Two Detectors

Figure 5.14 shows example interferograms obtained from the quasi-optical detector (5.14(a)) and the pyroelectric detector (5.14(b)). Measurements were made over for a number of beam currents, and for a number of RF voltages in the case of the quasi-optical tests. The examples shown here were recorded for standard beam optics with a single bunch at an RF voltage of 2.5 MV, with data normalised to detector sensitivity and bunch current squared. The results shown in this subsection were all conducted using the slow scan, with the interferogram's intensity being the average of the 20 samples recorded at a given position and the errors being the standard deviation of those samples.

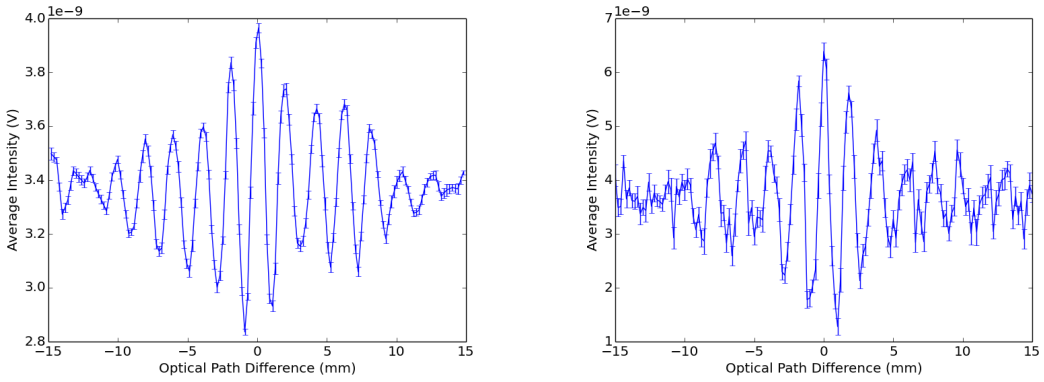

(a) Quasi-optical

(b) Pyroelectric

Figure 5.14: Interferograms measured from a single bunch in standard optics, from the quasi-optical and pyroelectric detectors.

The interferograms both have clearly defined peaks around the point of zero path difference and both have a central body which is asymmetric. Difficulties were encountered in measuring any interference with the pyroelectric detector for low current, through a combination of minor misalignment and higher detector noise, hence signals were only observed for high current where the bunch is bursting in the chaotic regime. The larger bandwidth of the pyrodetector allows the detection of emissions beyond that of the quasi-optical, and the bunch being unstable in this regime result in the irregular emissions of high frequency coherent bursts, leading to fluctuations in the detector signal.

The higher noise in the pyroelectric detector spectrum can be attributed to the fluctuations at the interferogram edges; the long time period over which the signal is measured leads to a potentially larger signal variation which appears as a rapidly varying signal, which in turn is interpreted as a high frequency in the Fourier transform.

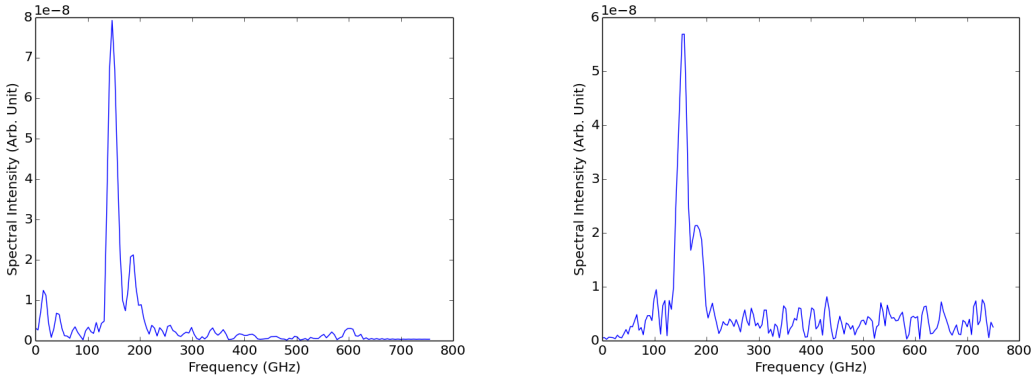

(a) Quasi-optical (b) Pyroelectric

Figure 5.15: Resulting spectrum from interferograms shown in figure 5.14

The mean signal is similar from both detectors, however the slight difference can be explained by the detector sensitivity. Post experimental analysis normalises to the sensitivity quoted in the specifications from the detector manufacturers, however this value is assumed to be irrespective of detected wavelength which is physically unlikely given the broad bandwidth of the detectors. The corresponding spectra from the interferograms are shown in figure 5.15. The majority of the spectral power is localised to between $\sim$ 130 and $\sim$ 200 GHz, with the signal from both detectors displaying the same form. The absence of signal below 130 GHz can be attributed to the optical systematic effect of the natural divergence of the emitted beam and detector low frequency cutoff as outlined in section 4.9.1. The absence of signal above 200 GHz is characteristic of a long bunch length, in

keeping with the expected behaviour of a bunch in a standard optics lattice.

In addition to the interferograms from standard optics, scans were also conducted in low alpha optics with a beam of 200 bunches at 50 μA per bunch. Figure 5.16 shows the recorded interferograms from both the pyroelectric and quasi-optical detectors using the slow scan. The scans were conducted at high resolution therefore their ranges were limited to $\pm$ 8 mm around the point of zero path difference. The pyroelectric measurement displays a very high degree of symmetry over the whole scan range, however the quasi-optical measurement, whilst displaying a similar form to the pyroelectric interferogram, does not appear symmetrical. This is believed to be the result of a minor mirror misalignment, as a small linear decrease in average signal with mirror position was seen even after normalising for the decrease in beam current over the duration of the scan.

As a result of the asymmetry, the corresponding spectra shown in figure 5.16 are notably different. Despite the high resolution interferograms yielding spectra up to $\sim$ 3 THz, no signal is observed above 1 THz. Whilst both spectra exhibit dips in power, in the case of the pyroelectric detector, some of the dips can be attributed to the beamsplitter used in the experiment. As mentioned in section 4.4.1, early measurements with the pyroelectric detector were conducted using a 160 μm thick splitter, the efficiency of which is shown with the spectra in figure 5.17(b). Whilst the splitter is the cause of the absence of signal at $\sim$ 275, there is coincidentally strong atmospheric absorption at this frequency as well as a splitter dip (atmospheric absorption taken to be through 1 metre of air). Unfortunately neither of these effects can be removed as the efficiency of the splitter at these frequencies $\sim$ 0, and the absorption is sufficient to attenuate the spectrum down

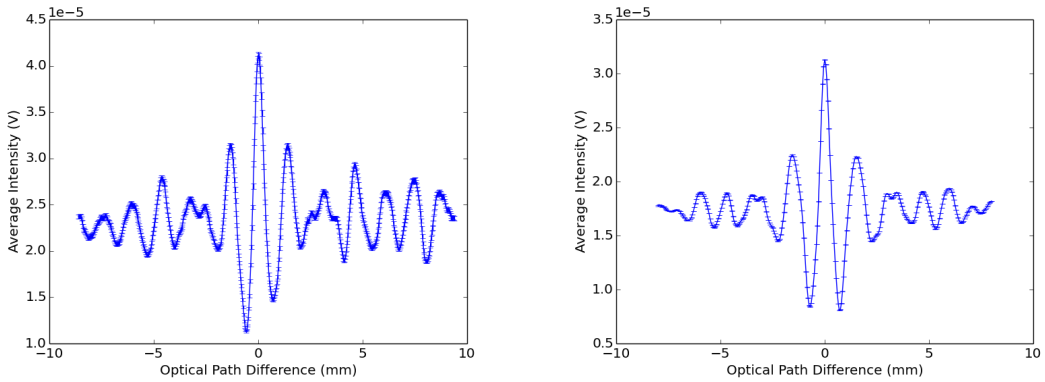

(a) Quasi-optical (b) Pyroelectric

Figure 5.16: Interferograms measured from 200 bunches in low-alpha optics, from the quasi-optical and pyroelectric detectors.

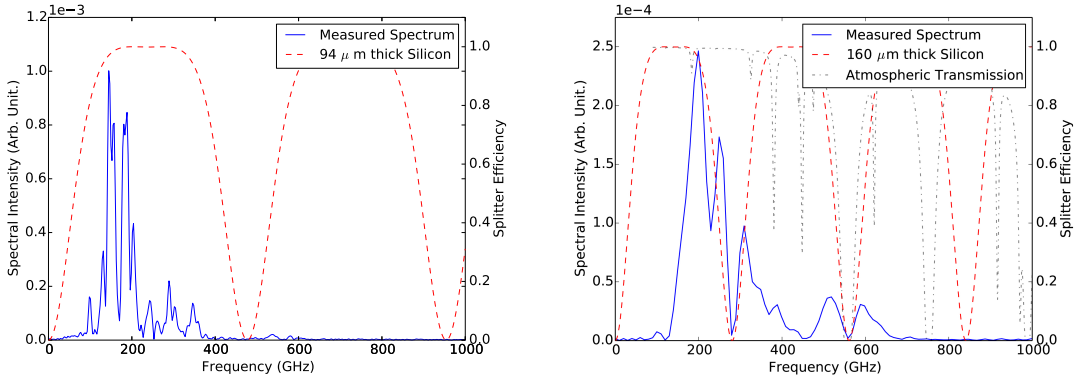

(a) Quasi-optical (b) Pyroelectric

Figure 5.17: Resulting spectrum from interferograms shown in figure 5.16 with silicon beamsplitter efficiency and atmospheric absorption.

to noise, therefore the true spectrum is not known. The thinner splitter used during the quasi-optical experiments displays a dip which appears to fall in a quiet region of the spectrum, thus the results are not adversely affected.

It should be noted that the spectra from low alpha operation display signal to a greater extent than those from standard optics operation shown in figure 5.15. This is expected from the shorter bunch length that naturally occurs from a lattice with a reduced momentum compaction factor. Whilst it may appear that the pyroelectric spectrum is broader than the quasi-optical signal, the magnitudes of the two signals are slightly different. By plotting them on a log scale as shown in figure 5.18, they are indeed comparable. The dip at 550 GHz is once again present courtesy of the atmospheric absorption.

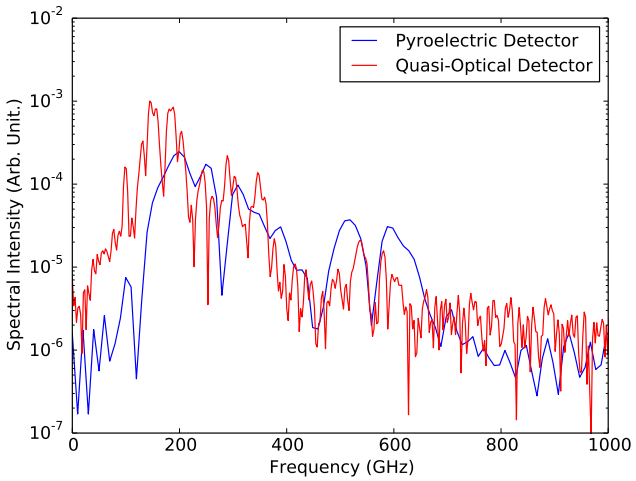

Figure 5.18: Comparison of spectra from the pyroelectric and quasi-optical detectors.

The absence of spectral power below $\sim$ 130 GHz is once again observed in both measurements, further evidencing the optical systematic effect. The remaining difference between the two signals can be attributed to the non-flat detector sensitivity. The quasi-optical detector is thought to be more sensitive to lower frequency signals, hence why the signal from the quasi-optical detector is of higher magnitude. At higher frequencies where the pyroelectric detector becomes more sensitive, the two signals are of similar magnitude, with the detectors frequency response explaining the differences in signal.

In the quasi-optical spectrum, there is limited evidence that the spectral power appears to vary periodically. Despite efforts to match the window based periodicity to the data by fitting varying the window thickness, the results showed the two effects never fully matched. A more accurate measurement of the window thickness would be beneficial in this process as the window spectra periodicity can vary significantly. Additionally, the effect of a slight curvature on the window should be investigated. The finite size of the beam means that if a curvature exists, different parts of the beam would refract due to a small non-zero angle of incidence that varies with beam position, thus further affecting the spectrum.

Whilst the pyroelectric detector has recorded a highly symmetric interferogram (and consequently smooth spectrum), the detector's slow response time results in the signal measured at any single point in the interferogram being the average of the 200 bunches over several thousand turns, effectively smearing the signal. The detector has been effective by revealing the extent of the coherent emissions, however given the nature of the instability, the quasi-optical detector with its fast response time is more suited to observing rapid changes in spectra with changing beam conditions. As such, the quasi-optical detector was used throughout subsequent experiments.

5.4.2 Spectral Scan Variation with Bunch Current

We have shown in figure 5.4 that the periodicity of the bursts changes with increasing bunch current, eventually reaching the point of chaotically emitted bursts, therefore by increasing the bunch current and thus the bursting periodicity, any high frequency fluctuations may be observed and any resulting changes in emitted spectrum may be measured. As such, experiments were conducted measuring the interference from the bunch over bunch current range. It became clear during the experimental investigation described in the previous subsection that the time required to acquire one interferogram with the slow

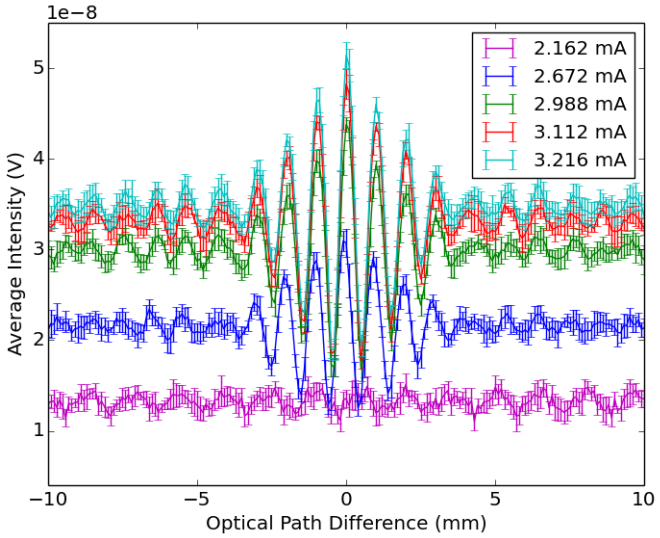

Figure 5.19: Interferometer scans for increasing bunch current from a single bunch in standard optics.

scan was impractical, hence the creation of the fast scan type which was used to acquire the results presented here.

Figure 5.19 shows the recorded interferograms from a single bunch of increasing current in standard optics at 3.5 MV RF voltage, with the corresponding spectra shown in 5.20. As these scans were recorded using the fast scan, the interferogram intensity is the average of the 5 recorded scans at a given position, with the error being the standard deviation of the 5 scans. Unfortunately the lowest bunch current from which signal could be observed was 2.6 mA due to a combination of the sensitivity of the lock-in amplifier (see section 4.6.3) given the lock-in reference frequency of 533 kHz, and the optical effects identified in section 4.9.1. Shown as an example of a lower current scan in figure 5.19 is the signal from a 2.1 mA bunch, however as no identifiable interference was observed and the signal is essentially noise, therefore the resulting spectrum from this measurement is not shown. Other than average signal amplitude, the interferograms show little variation with increasing bunch current, as evidenced by the spectra in figure 5.20. The spectra are similar to the examples shown in figure 5.15, indicating a long bunch length, however the presence of a small signal around 300 GHz indicates the bunch is non-Gaussian.

Interferometric scans were also recorded under low alpha optics. Figure 5.21 shows the average of 10 interferograms recorded from 100 bunches ranging from 5 to 80 μA per bunch. The wobble seen in figure 5.21 is due to a slight time delay when operating

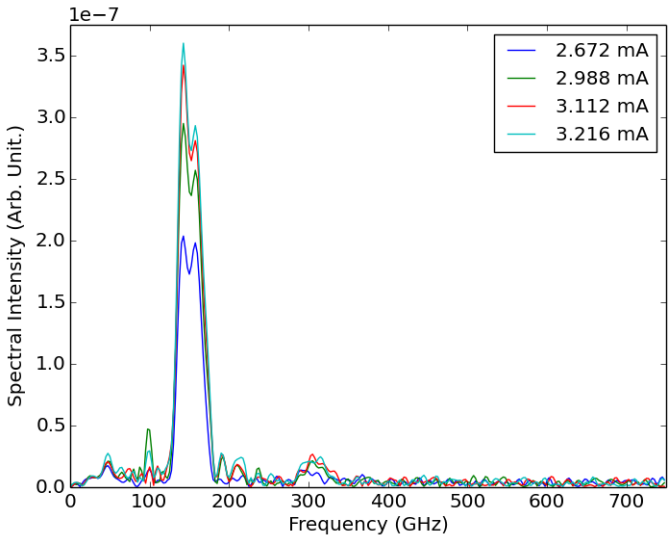

Figure 5.20: Resulting spectra from interferograms shown in figure 5.19 from a single bunch in standard optics.

the interferometer. The representation of the interferograms is as a function of position, whereas they are actually recorded as a function of time by sampling at a fixed rate. A minor variation in the delay time at the beginning will mean recording of a few samples from a static position, after which the interferogram is then recorded. A peak matching technique was applied following the removal of the static position samples, however the time difference is smaller than the resolution of the interferograms, therefore the appearance of the shift here can be attributed to graphical interpolation in the plot. Despite this effect, the sampling rate is still sufficient to measure high frequencies, therefore the relative position of the interferogram should not significantly impact their spectra. There appears to be little variation in the interferograms except for amplitude, however it is notoriously difficult to read information from the time domain interferogram signal.

The corresponding spectra are shown in figure 5.22. The spectra notably do not exhibit the wobble seen in figure 5.21, further evidencing that the wobble is a graphical interpolation effect. The most interesting feature regarding the form factor is the band between 400-600 GHz which varies with current. Furthermore, a discontinuity can be seen just after 30 μA per bunch where the high frequency component jumps. Using the bunch length in table 4.1, the threshold current from equation 2.43 was calculated to be 31 μA. The agrees with the threshold as previously calculated for low alpha mode [54, 134], however the bunch lengths as measured in section 4.1.2.2 and [102] are shown

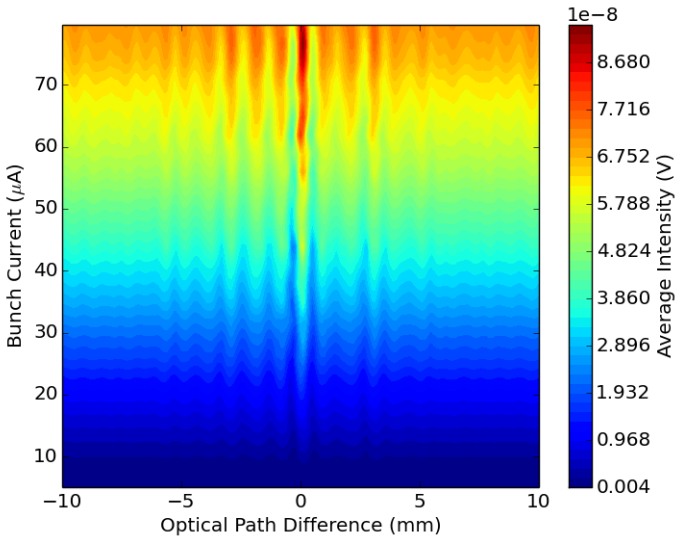

Figure 5.21: Interferometer scans for increasing bunch current from 100 bunches in low alpha optics.

to be longer which would increase the threshold current. Given the discrepancies already seen between the theory and measurements in section 5.2, and the bunch current step size in the experiments, it is possible that the discontinuity here is the microbunching instability threshold, however further measurements would be needed to accurately verify this.

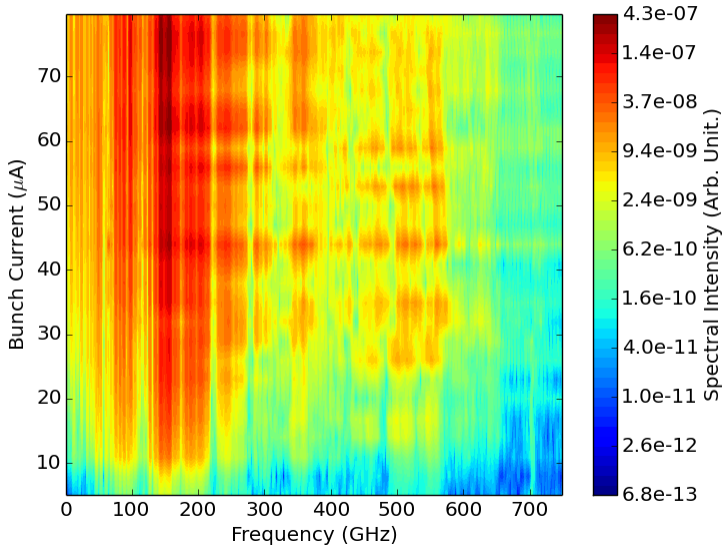

Figure 5.22: Resulting spectra from interferograms shown in figure 5.21 from a 100 bunches in low alpha optics.

The consistency of the unsmooth spectra with increasing current at lower frequencies suggests that it is not an artefact of the bunch but it is systematic. The two largest contributors to this are believed to be optical effects, namely aperture diffraction and spherical aberration from the focusing mirror, and the detector response. Given the size of the apertures relative to the wavelengths, the contribution from diffraction at this stage is thought to be negligible in comparison to any potential detector effects or aberrations from the mirror. The variation in detector response with frequency remains an unknown as no source(s) are readily available to which the detectors can be calibrated over their entire bandwidth. As such, the spectral variation cannot be fully accounted for until the detector can be characterised.

A comparison to the theoretical spectrum produced from section 4.9.1 is shown in figure 5.23 for two scaled example spectra for high and low bunch currents (79 μA and 5 μA respectively). The high frequency components for the low bunch current scans are an artificial amplification of noise from the signal scaling. Whilst the theoretical spectrum matches the envelope of the observed spectra, the measurements display an obvious variation in spectral power that is clearly not the smooth function normally expected of a typical form factor, particularly for long wavelengths. The decrease in intensity to $\sim$ 300 GHz after which the power increases suggests that the overall envelope of the form factor is that of a sum of two Gaussians, which matches the observations from the streak camera

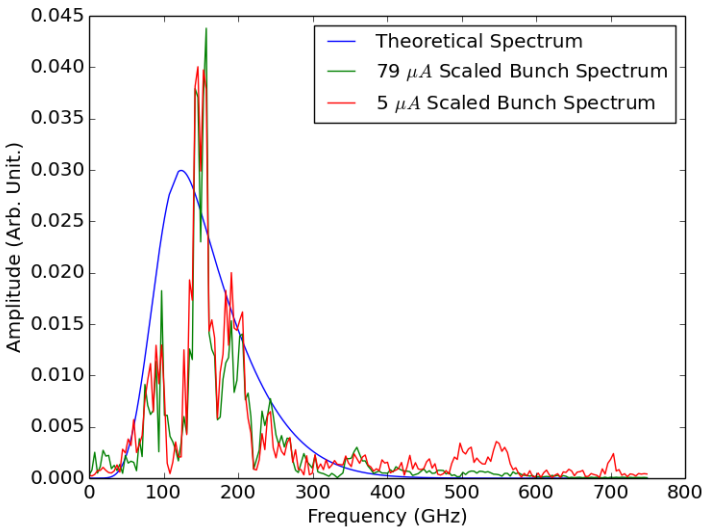

Figure 5.23: Theoretical spectrum from beam divergence and clipping, and low frequency detector cutoff, with the scaled measured average spectrum from a low current (5 μA) and high current (79 μA) bunch from low alpha optics with 100 bunches.

shown in section 4.1.2.2. The overwhelming fluctuation in the measured spectral power, however, means that this is only a preliminary estimate at this stage.

The variation in the amplitude vs bunch current is shown in figure 5.24, along with the amplitude from another scan set taken with 200 bunches. Given the similarity to the 100 bunch scans, the 200 bunch interferogram and spectral data are not shown as they cover a smaller bunch current range. The amplitude of the 100 bunch scans were taken as the average amplitude at the point of zero path difference from the 10 scans at each bunch current, with the error being the standard deviation of the 10 amplitudes.

The 100 bunches scans do not display the large variation in signal power seen in the standard optics results in figure 5.9, therefore the results here were fitted to the function $y = Ax^B + C$ as before, but for the whole current range. The result of the fits yielded $y = (7.79 \times 10^{-12} \pm 1.03 \times 10^{-12})\ x^{2.09 \pm 0.03}$. The C offset from the fit was $1.74 \times 10^{-12} \pm 0.19 \times 10^{-12}$. Additionally shown is the $y = Ax^2 + C$ line using the same A coefficient and offset C. The signal appears to be in keeping with the N^2 dependence until $\sim 40\ \mu A$, whereupon the signal becomes larger. This is close to the discontinuity seen in the spectra in figure 5.22, thus suggesting the instability threshold is in this region, however a more precise determination of the threshold requires a higher current resolution.

Despite the 100 bunch and 200 bunch data showing good agreement with one another, their amplitude scaling with current is only slightly above the N^2 line and does not fluctuate as largely as the equivalent standard optics result. As the instability theory can-

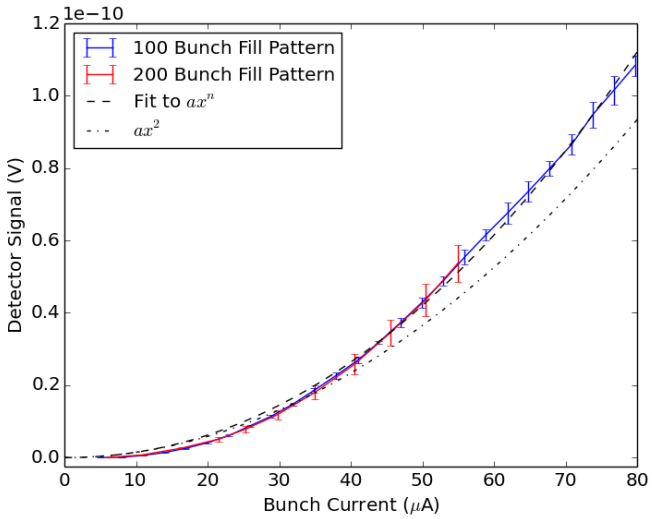

Figure 5.24: Bunch current dependence of the signal from a quasi-optical detector for two multi-bunch fill patterns in low-alpha optics.

not yet predict the bunch currents where the instability either undergoes a discontinuity or changes bursting regime, we may conclude that the data here were recorded from below threshold into the quasi-periodic region as the large variation from the chaotic bursting is not seen. This is further evidenced by the data in [134] which investigates the instability threshold, indicating that the bunch currents here only correspond to the quasi-periodic regime.

5.5 Summary

In this chapter, we have shown that the microbunching instability has been observed at Diamond Light Source in both standard optics and low alpha optics operation, with changes in its behaviour in the standard operation experiments seen with increasing bunch current and RF voltage. Beyond the instability threshold, the relationship between the detected power and bunch current was shown to fluctuate around the N^2 proportionality normally expected of coherent radiation, with higher current bunches above the proportionality regardless of RF voltage. The threshold current for the instability in standard optics appeared to agree qualitatively with the bunched beam theory, however there were quantitative differences between the predictions and the measured data. Modifications and extensions to the theory that could be investigated were proposed.

The interferometer scans revealed that the predicted optics matched the envelope of the measured spectra, but systematic effects have resulted in an unsmooth spectrum, particularly at longer wavelengths. This large variation in spectral power with frequency is attributed to a combination of optical effects and unknown detector response, however the bunch form factor was still identified to be the sum of two Gaussians as further evidenced by streak camera measurements. At this stage, the Kramers-Kronig technique cannot be applied to the data here owing to the unresolved spectral variations.

Chapter 6

Conclusion

This chapter summarises the work presented in this thesis, outlines the conclusions from the results presented, as well as proposing modifications to the experimental setup and possible future experiments.

6.1 Summary and Conclusions

To investigate the microbunching instability at Diamond Light Source, its property of CSR bursts with wavelengths comparable to that of the bunch length and shorter, required the development of longitudinal diagnostic apparatus new to Diamond. Initial experiments employed ultra-fast Schottky Barrier Diode detectors to detect the coherent radiation bursts arising as a result of the instability, and to investigate the threshold current and machine conditions necessary to trigger it. They successfully detected the instability and showed that bursts of radiation are emitted above a current threshold with the bursting behaviour recorded for increasing bunch current. The theory of the instability's threshold consists of two complimentary models with their applicability differing according to the bunch length. The theory showed that the bunched beam model was more accurate, however whilst the results here show this to be qualitatively true, the theory does not numerically match the measured thresholds, with inconsistencies seen between experiments.

Experimentally, below the threshold current, the power was measured to be proportional to the number of electrons squared as expected by coherent radiation, however the onset of the instability revealed the signal varied in proportionality with increasing bunch current, with the power from high current bunches being well above N^2. Being modulated to the bunch revolution frequency, the detected signal revealed the presence of significant

internal motion and structural changes with increasing bunch current. Additional tests confirmed the repeatability of the phenomenon in the short term, however the results changed over the long term after shutdown periods, suggesting the startup and tuning of the machine affects the onset of the instability.

The aim thereafter was to quantify the bunch structure through measurements of coherent emissions. To achieve this, a dedicated mm-wave diagnostics viewport was installed at Diamond, providing the necessary CSR from bunches inside a dipole bending magnet without the incoherent high energy photons that are usually desired by beam line users. A system was installed to provide the capability of spatially mapping the coherent radiation, which was subsequently performed yielding information on the size and natural divergence of the beam in two frequency bands, using two ultra-fast Schottky Barrier Diode detectors.

To measure the spectra using the chosen technique of Fourier transform spectroscopy, a Michelson interferometer was designed, constructed and implemented. Knowing the theoretical coherent spectrum from a bunch, the interferometer components were carefully selected so as to minimise their individual effect on the measured signal. Following the characterisation of the radiation beam and interferometer, the theoretical effective spectrum at the detector was calculated and shown to be heavily affected at long wavelengths by the natural divergence. Two detectors were used, a pyroelectric detector which provided a large bandwidth but slow response time, and a quasi-optical Schottky barrier diode detector which offered a fast response in a modest bandwidth. The interferometric measurements revealed that the theoretical spectrum matched the overall envelope of the corresponding measured spectra, however it did not account for significant power variation, particularly at longer wavelengths. Identified as a systematic effect, the spectra is believed to be affected by optical effects (despite efforts to minimise these by compacting the interferometer), but more significantly by the unknown detector response with frequency.

Despite this unexpected variation in power with frequency, the spectrum appeared to display a form factor of the sum of two or more Gaussians, with streak camera measurements providing further evidence for this. With increasing current, evidence of large scale changes in the form factor are observed, however until the quasi-optical detector can be fully characterised, any smaller changes cannot be identified and the measured spectra are not suitable for use in the reconstruction technique.

6.2 Future Work

In section 5.2, possible modifications to the existing theory were suggested such as the extension of the shielding suppression to cover the geometry of the beam pipe, the inclusion of transverse dynamics, space charge effects etc. Running simulations for increasing bunch current may also provide further information regarding the instability's behaviour beyond threshold where it enters the quasi-periodic regime and further still into the chaotic region.

Given that the microbunching instability's primary consequence is the emission of bursts of coherent radiation, the spectra recorded by the detector in its presently uncalibrated state cannot be used for reconstructing the longitudinal charge distribution. The system ultimately suffers from the unknown response of the detector with frequency. The detector can be characterised by purchasing commercial sources which are available and cover the whole detectable range of the quasi-optical detector [135]. Another method to characterise the detectors which should become available in the future, is the use of a THz laser currently being developed in the physics department at Royal Holloway, which should offer beams with frequencies up to 2 THz.

For the current setup, the possibility was explored to install a parabolic mirror in the transfer line to parallelise the radiation incident upon the interferometer. It was decided that producing a custom designed mirror would be more beneficial, however, the spatial distribution measurements were required first to provide the parameters necessary in the mirror design. The installation of this focusing mirror in the transfer line would be advantageous, particularly benefiting the longer wavelengths which suffer from the natural divergence, and the overall signal to noise ratio should increase especially in the single bunch cases. Care must be taken as results have already shown that detector saturation is possible when only measuring the power from a fraction of the beam's size, an effect which would only be amplified when increasing the power density with the inclusion of a focusing mirror. This, in conjunction with technical delays, meant the mirror could not be manufactured on time, however future installation should be considered.

Other possibilities for improving the setup would be a precise measurement of the fused silica window thickness. Its thickness can dramatically alter the spectrum as it introduces a periodic power variation with frequency as seen in section 4.2.2. The difficulties of removing such a component from a system under vacuum means the glass must be measured in situ.

The ultimate goal of the project was to measure the bunch form factor for a single shot. The interferometer was created to measure the envelope of the form factor, with a spectrometer to be later installed, using the interferometer results as a source of comparison. Difficulties in attributing spectral observations to specific systematic effects in the spectra measured with the interferometer meant insufficient time was available for this later stage.

The current setup is unsuitable for single shot measurements as the interferometer suffers from a long operational time, resulting in the spectra being smoothed out over several million turns. A single shot system can constructed by modifying the device into a spectrometer, employing the multiple detectors to avoid any moving parts. The detectors outlined in section 4.5.2 only operate in their stated bandwidth courtesy of a waveguide, the efficiencies of which are known including the well defined lower frequency cutoff. Beyond this, the detectors do not have the ability to distinguish the frequency of the incident radiation, therefore any measured power spectrum cannot have a resolution lower than the detector bandwidth. As such, resolving high frequency signals from bursts using these detectors will not be possible and the possibility of installing other detectors should be considered.

Appendix A

Single Electron Spectrum

This appendix chapter shows the derivation of the spectrum from a single electron undergoing a centripetal acceleration which can be found in a number of textbooks. Unless otherwise referenced, the derivation described was obtained from [22].

The rate of energy transfer per unit area of an electromagnetic field is given by the Poynting vector:

$$\vec{S} = \vec{E} \times \frac{\vec{B}}{\mu_0}. \tag{A.1}$$

The Lienard-Wiechert potentials of a moving electric charge relate the electric and magnetic fields by

$$\vec{B} = \frac{1}{c}\vec{n} \times \vec{E}, \tag{A.2}$$

where $\vec{n}$ is a unit vector along the line between the point of emission to the point of observation [22]. Substituting this into equation A.1, and using the relation $\epsilon_0\mu_0 = 1/c^2$ we get

$$\vec{S} = \epsilon_0 c \left[\vec{E} \times (\vec{n} \times \vec{E})\right] = \epsilon_0 c \left[\vec{n}E^2 - (\vec{n} \cdot \vec{E})\vec{E}\right]. \tag{A.3}$$

As the Poynting vector is dependant only on the electric field, we can use the retarded Lienard-Wiechert electrical potential defined as

$$\vec{E}(\vec{r},t)= \frac{q}{4\pi\epsilon_0 c}\frac{1}{\left[1-\vec{n}\cdot\vec{v}/c\right]^3}\left(\left[\frac{(1-v^2/c^2)(\vec{n}-\vec{v}/c)}{|\vec{r}-\vec{r'}|^2}\right] + \frac{1}{c}\left[\frac{\vec{n}\times\left[(\vec{n}-\vec{v}/c)\times\dot{\vec{v}}/c\right]}{|\vec{r}-\vec{r'}|}\right]\right). \tag{A.4}$$

The electric potential is split into two terms, the first being velocity based, the second being acceleration based. As the velocity term falls off proportional to R^{-2} (where $R = |\vec{r}-\vec{r'}|$), then it is negligible in the far field, leaving just the acceleration term. Therefore $\vec{n}\cdot\vec{E}=0$, so equation A.3 can be simplified to

$$\vec{S} = \epsilon_0 c|\vec{E}|^2\vec{n}. \tag{A.5}$$

As the Poynting vector is the rate of energy transfer per unit area, then using the relation $dA = r^2 d\Omega$ from spherical polar co-ordinates, we can write

$$\frac{dU}{dt} = \vec{n}\cdot\vec{S}dA = \epsilon_0 c|r\vec{E}|^2\vec{n}\cdot\vec{n}d\Omega = \epsilon_0 c|r\vec{E}|^2 d\Omega. \tag{A.6}$$

Before we can substitute in our electric field from A.4, we must take into account that some quantities in the electric field equation must be calculated at the retarded time, $t' = t - \frac{1}{c}|\vec{r}-\vec{r'}|$. As the vector $\vec{r}$ is constant, and the rate of change of the resultant vector $|\vec{r}-\vec{r'}|$ is equal to the velocity component in the direction of that resultant vector, then $\frac{\delta}{\delta t}|\vec{r}-\vec{r'}| = -\left[\vec{n}\cdot\vec{v}\right]$, which is negative due to the radiation propagating at velocity $\vec{v}$ towards the observer, thus decreasing $|\vec{r}-\vec{r'}|$. The energy can therefore be calculated by inclusion of a corrective factor:

$$\int\frac{dU}{dt}dt = \int\epsilon_0 c|r\vec{E}|^2\frac{dt}{dt'}dt' = \epsilon_0 c\int|r\vec{E}|^2\left(1-\frac{(\vec{n}\cdot\vec{v})}{c}\right)dt'. \tag{A.7}$$

We can now insert the second term in equation A.4 as our electric field into A.6, but including the corrective factor from A.7, we get

$$\frac{d^2U}{dtd\Omega} = \epsilon_0 c r^2 \left(1 - \frac{(\vec{n}\cdot\vec{v})}{c}\right)\left[\frac{q}{4\pi\epsilon_0 c}\left(\frac{\vec{n}\times\left[(\vec{n}-\vec{v}/c)\times\dot{\vec{v}}/c\right]}{|\vec{r}-\vec{r}'|\left(1-\frac{(\vec{n}\cdot\vec{v})}{c}\right)^3}\right)\right]^2$$
$$= \frac{q^2}{(4\pi)^2\epsilon_0 c}\frac{\left[\vec{n}\times\left([\vec{n}-\vec{v}/c]\times\dot{\vec{v}}/c\right)\right]^2}{\left(1-\frac{(\vec{n}\cdot\vec{v})}{c}.\right)^5} \tag{A.8}$$

It is more useful to express this rate of power per unit area in the frequency domain, which can be obtained by a Fourier transform. A thorough derivation of the Fourier transform can be found in [22], however for the purposes of this thesis, only the calculated equations are necessary. The resulting expression for the frequency spectrum is

$$\frac{d^2I}{d\omega d\Omega} = \frac{q^2}{(4\pi)^3\epsilon_0 c}\frac{3\gamma^2}{4}\left(\frac{\omega}{\omega_c}\right)^2\left(1+\gamma^2\psi^2\right)^2$$
$$\times\left[K_{2/3}^2(\xi) + \frac{\gamma^2\psi^2}{1+\gamma^2\psi^2}K_{1/3}^2(\xi)\right], \tag{A.9}$$

where ω_c is the critical frequency as defined in equation 2.22, ψ is the vertical angle between the observer and the plane of propagation of the synchrotron radiation, $\xi = \frac{1}{2}\frac{\omega}{\omega_c}\left(1+\gamma^2\psi^2\right)^{3/2}$, and K_n is the modified Bessel function. As the solid angle is $d\Omega = d\theta d\psi$, we can integrate over all vertical angles ,ϕ, to give us the spectrum per unit frequency, per angle in the horizontal plane:

$$\int \frac{d^2I}{d\omega d\Omega}d\psi = \int \frac{d^3I}{d\omega d\theta d\psi}d\psi = \frac{d^2I}{d\omega d\theta}. \tag{A.10}$$

The result of this integral, from [22] is

$$\frac{d^2I}{d\omega d\theta} = \left(\frac{q^2}{4\pi\epsilon_0 c}\right)\frac{\sqrt{3}\gamma}{4\pi}\left(\frac{\omega}{\omega_c}\right) \times \left(\left[K_{2/3}\left(\frac{\omega}{\omega_c}\right) + \int_{\omega/\omega_c}^{\infty} K_{5/3}(y)dy\right] + \left[-K_{2/3}\left(\frac{\omega}{\omega_c}\right) + \int_{\omega/\omega_c}^{\infty} K_{5/3}(y)dy\right]\right). \quad \text{(A.11)}$$

The two terms in equation A.11 refer to the horizontally and vertically polarised radiation respectively. In the case where the polarisation is unimportant, we can sum over both states to give

$$\frac{d^2I}{d\omega d\theta} = \left(\frac{q^2}{4\pi\epsilon_0 c}\right)\frac{\sqrt{3}\gamma}{2\pi}\left(\frac{\omega}{\omega_c}\right)\int_{\omega/\omega_c}^{\infty} K_{5/3}(y)dy. \quad \text{(A.12)}$$

Further to equation A.9, we can convert it from energy per unit frequency bandwidth to the number of photons in a fractional bandwidth ($\Delta\omega/\omega$) by dividing by the photon energy, $\hbar\omega$, and multiplying by the number of electrons per second, given by dividing the beam current, I, by the electron charge, e. The resulting equation (converting from solid angle into horizontal and vertical angles, and using the definition of the fine structure constant, α, from equation 2.5) in units of photons/(s mrad^2) is given as:

$$\frac{d^2N}{d\theta d\psi} = \frac{\alpha}{\pi^2}\frac{3\gamma^2}{4}\frac{I}{e}\frac{\Delta\omega}{\omega}\left(\frac{\omega}{\omega_c}\right)^2\left(1+\gamma^2\psi^2\right)^2 \times \left[K_{2/3}^2(\xi) + \frac{\gamma^2\psi^2}{1+\gamma^2\psi^2}K_{1/3}^2(\xi)\right]. \quad \text{(A.13)}$$

Appendix B

Useful Formulae

The electron energy loss through synchrotron radiation emission in dipole magnetic fields per revolution of a storage ring is given by

$$U_0 = \frac{4\pi}{3}\frac{r_0}{(mc^2)^3}\frac{E^4}{\rho} = V_{RF}sin(\phi_s), \tag{B.1}$$

where r_0 is the classical electron radius, E is the electron's energy, ρ is the dipole bending radius, V_{RF} is the peak RF voltage, and ϕ_S is the RF synchronous phase.

The synchrotron tune ν is given by:

$$\nu = \frac{f_s}{f_{rev}} = \sqrt{\frac{\eta f_{RF}}{2\pi f_{rev}}\left(\frac{eV_{RF}}{E_0}\right)cos(\phi_s)}, \tag{B.2}$$

where f_{rev} is the bunch revolution frequency, f_{RF} is the RF frequency, V_{RF} is the RF voltage, E_0 is the particle rest energy, ϕ_s is the synchronous phase, and η is the slip factor definded as

$$\eta = \alpha - \frac{1}{\gamma^2}, \tag{B.3}$$

where α is the momentum compaction factor and γ is the ratio of the particle's energy to its rest mass. For Diamond Light Source, which operates at a beam energy of 3 GeV, $\alpha \gg \frac{1}{\gamma^2}$ therefore we can approximate $\eta \approx \alpha$.

The zero current bunch length is given by

$$\sigma_z = \frac{c\alpha}{2\pi f_s}\sigma_E, \tag{B.4}$$

where σ_E is the energy spread.

The following formulae are the radiation integrals which govern the particle beams properties when modified by the emission of synchrotron radiation [24]:

$$I_{1x} = \oint \frac{D_x}{\rho} ds \tag{B.5}$$

$$I_2 = \oint \frac{1}{\rho^2} ds \tag{B.6}$$

$$I_3 = \oint \frac{1}{\rho^3} ds \tag{B.7}$$

$$I_{4x} = \oint \frac{D_x}{\rho} \left(\frac{1}{\rho^2} - 2k \right) ds \tag{B.8}$$

$$I_{5x} = \oint \frac{H_x}{\rho^3} ds = \oint \frac{1}{\beta_x} \left(D_x^2 + \left(\beta_x D'_x - \frac{1}{2} \beta' D_x \right)^2 \right) ds, \tag{B.9}$$

where D_x is the horizontal dispersion, ρ is the dipole bending radius, $k = \frac{\partial B_y}{\partial x} / (B\rho)$ is the quadrupole field strength, and $'$ denotes the spatial derivative [52], [136]. From these, we get the damping partition numbers:

$$J_x = 1 - \frac{I_4 x}{I_2} \tag{B.10}$$

$$J_y = 1 - \frac{I_4 y}{I_2} \tag{B.11}$$

$$J_\epsilon = 2 - \frac{I_{4x} + I_{4y}}{I_2}. \tag{B.12}$$

The emittance can also be expressed as

$$\epsilon = \frac{55}{32\sqrt{3}} \frac{\hbar \gamma^2}{m_e c} \frac{I_5}{I_2 - I_4}. \tag{B.13}$$

Appendix C

Microbunching Instability Threshold Derivation

For the case of a coasting beam, the expression for the instability threshold was derived in [79] as follows. The equilibrium distribution is obtained from the Haissinski equation, which is given as

$$I(z) = Kexp\left[-\frac{z^2}{2\sigma_z^2} - \frac{1}{2\pi V_{RF} f_{RF} \sigma_z^2}\int_0^\infty S(z')I(z-z')dz'\right], \tag{C.1}$$

where $S(z)$ is a step response function given as

$$S(z) = \frac{2\pi\rho}{e}\int_{-\infty}^{z} W(z')dz', \tag{C.2}$$

where $W(z)$ is the wakefield. For the case of the CSR wakefield in free space, this can be approximated by

$$s(z) = \begin{cases} -Z_0\left(\frac{\rho}{3c}\right)^{\frac{1}{3}} z^{\frac{1}{3}} & \text{z} > 0 \\ 0 & \text{z} \leq 0, \end{cases}$$

where $Z_0 = 376.7\Omega$ is the free space impedance [51]. For this case, the Haissinski distribution can be written in a dimensionless form:

$$y(x) = Kexp\left[-\frac{x^2}{2} \pm \int_0^\infty \frac{y(x-x')}{x^{\frac{1}{3}}}dx'\right], \tag{C.3}$$

where

$$x \equiv \frac{z}{\sigma_z}, \tag{C.4}$$

$$y(x) \equiv \frac{Z_0 c}{2\pi f_{RF} V_{RF} \sigma_z} \left(\frac{\rho}{3\sigma_z}\right)^{\frac{1}{3}} I(z). \tag{C.5}$$

The $\pm$ is required to account for the sign of the momentum compaction factor, α. By integrating the above expression and knowing that the integral of $I(z)$ is equal to the total charge in a bunch of length σ_z, we can write

$$F = \int_{-\infty}^{\infty} y(x)dx = \frac{Z_0 c}{2\pi f_{RF} V_{RF} \sigma_z} \left(\frac{\rho}{3\sigma_z}\right)^{\frac{1}{3}} \frac{Nec}{\sigma_z}. \tag{C.6}$$

Knowing the bunch current is given by $I_b = Nef_{rev}$, and rearranging equation C.6, at the threshold bunch current we get

$$\sigma_0^{\frac{7}{3}} = \frac{c^2 Z_0}{2\pi F 3^{1/3}} \frac{I_b^{th} \rho^{1/3}}{V f_{RF} f_{rev}}. \tag{C.7}$$

For the bunched beam theory, the expression is initially derived in [71]. Beginning with the expression for the scaled current from equation 2.40, by inserting the definition of I_n from equation 2.41 and rearranging we get

$$\alpha \sigma_E^2 = \frac{I_b \rho^{\frac{1}{3}}}{\gamma \xi I_A \sigma_z^{\frac{1}{3}}}. \tag{C.8}$$

From the formulae for synchrotron frequency and bunch length from equation B.2 and equation B.4 respectively, we can write

$$\begin{aligned} \sigma_z^2 &= \left(\frac{c\alpha\sigma_E}{2\pi f_s}\right)^2 \\ &= \frac{(c\alpha\sigma_E)^2 \, 2\pi f_{rev} E_0}{(2\pi)^2 \, e f_{rev}^2 \alpha f_{RF} V_{RF} \cos(\phi_s)} \\ &= \frac{\alpha c^2 \sigma_E^2 E_0}{2\pi e f_{rev} f_{RF} V_{RF} \cos(\phi_s)}. \end{aligned} \tag{C.9}$$

Inserting the expression for $\alpha\sigma_E^2$ from equation C.8, and using $E_0 = \gamma mc^2$ we find that

$$\sigma_z^2 = \frac{c^2 I_b \rho^{\frac{1}{3}} m c^2}{\xi I_A \sigma_z^{\frac{1}{3}} 2\pi e f_{rev} f_{RF} V_{RF} \cos(\phi_s)}. \tag{C.10}$$

From the definition of I_A from equation 2.30, and using $Z_0 = \frac{1}{\epsilon_0 c}$, we can rearrange and finally write

$$\sigma^{\frac{7}{3}} = \frac{c Z_0}{8\pi^2 \xi} \frac{\rho^{\frac{1}{3}} I_b}{f_{rev} f_{RF} V_{RF} \cos(\phi_s)}. \tag{C.11}$$

Bibliography

[1] J. Cockcroft and E. Walton, Proc. Roy. Soc. Series A **136**, 619 (1932).

[2] R. J. van de Graaff, Phys. Rev. **38**, 1919 (1931).

[3] The ATLAS Collaboration, Phys. Lett. B **716**, 1 (2012).

[4] The CMS Collaboration, Phys. Lett. B **716**, 30 (2012).

[5] The International Linear Collider: Technical Design Report, `http://www.linearcollider.org/ILC/Publications/Technical-Design-Report`, 2013.

[6] M. Aicheler *et al.*, A Multi-TeV linear collider based on CLIC technology: CLIC Conceptual Design Report, `http://project-clic-cdr.web.cern.ch/project-clic-cdr/CDR_Volume1.pdf`, 2012, CERN-2012-007.

[7] E. McMillen, Phys. Rev. **68**, 143 (1945).

[8] V. Veksler, J. Phys. (U.S.S.R) **9**, 153 (1945).

[9] F. Goward and D. Barnes, Nature **158**, 413 (1946).

[10] M. Oliphant *et al.*, Proc. Phys. Soc. **59**, 666 (1947).

[11] M. Blewitt, Rev. Sci. Instru, **24**, 725 (1953).

[12] A. Robinson, X-ray Data Booklet, Section 2.2: History of Synchrotron Radiation, `http://xdb.lbl.gov/Section2/Sec_2-2.html`.

[13] E. Wilson and A. Sessler, *Engines of Discovery* (World Scientific, 2007).

[14] S. Lee, *Accelerator Physics*, 2 ed. (World Scientific, 2004).

[15] K. Wille, *The Physics of Particle Accelerators* (Oxford University Press, 2001).

[16] B. Nash, Physics of the electron beam source: beam size, shape and lifetime and the relationship to the xray radiation properties., Talk, `http://www.esrf.eu/files/live/sites/www/files/Instrumentation/friday-lectures-slides/Talk_B.Nash.pdf`.

[17] H. Winick, Proc. PAC97 (1997), FBC003.

[18] Diamond Light Source, `http://www.diamond.ac.uk`.

[19] A. Baldwin *et al.*, Proc. EPAC 2006 (2006), THPLS128.

[20] E. C. Longhi *et al.*, J. Phys. Conf. Ser. **425** (2013).

[21] J. C. Schouten and E. C. M. Rial, Proc. IPAC 2011 (2011), THPC179.

[22] P. J. Duke, *Synchrotron Radiation* (John Wiley & Sons, 2000).

[23] A. Wolski, Storage Ring Design, Lecture at Joint US-CERN-Japan-Russia School on Particle Accelerators: Synchrotron Radiation and Free Electron Lasers, 2011.

[24] A. Chao and M. Tigner, *Handbook of Accelerator Physics and Engineering*, 3 ed. (World Scientific, 1999).

[25] S. Leemann *et al.*, Phys. Rev. ST Accel. Beams **12** (2009).

[26] History of X-rays and Synchrotrons, `http://www.lightsources.org`.

[27] P. Elleaume, Insertion Devices Part V: Undulators for Free Electron Lasers, Lecture at CASL Synchrotron Radiation and Free-Electron Lasers, Brunnen, 2003.

[28] Free-electron laser FLASH, `http://flash.desy.de`.

[29] P. Emma *et al.*, Nat. Photon **4**, 641 647 (2010).

[30] J. Clarke, CLARA: A new particle accelerator test facility for the UK, Seminar on 25th Feb 2015 at Royal Holloway, University of London.

[31] J. Rosenzweig, Fifth Generation Light Sources: X-ray FELs Based on New Accelerator and Undulators, Workshop on Advanced X-Ray FEL Development, DESY, 2014.

[32] J. Harrison, A. Joshi, J. Lake, R. Candler, and P. Musumeci, Phys. Rev. ST Accel. Beams **15** (2012).

[33] E. Esarey, C. Schroeder, and W. Leemans, Rev. Mod. Phys. **81**, 1229 (2009).

[34] R. England *et al.*, Rev. Mod. Phys. **86**, 1337 (2014).

[35] C. Christou *et al.*, Proc. IPAC 10 (2010), WEPEA066.

[36] R. Walker, Proc. APAC 2007 (2007), TUYMA03.

[37] I. Martin *et al.*, Proc. IPAC 13 (2013), MOPEA071.

[38] R. Walker *et al.*, Proc. IPAC 14 (2014), MOPRO103.

[39] R. Bartolini *et al.*, Proc. EPAC08 (2008), TUPP020.

[40] M. Abbott, G. Rehm, and I. Uzun, Proc. IBIC2013 (2013), WEPC10.

[41] G. Rehm, A. Morgan, R. Bartolini, I. Martin, and P. Karataev, Proc. DIPAC 09 (2009), TUPD32.

[42] R. Bartolini, G. Rehm, and P. Karataev, Proc. PAC09 (2009), FR5RFP074.

[43] A. Hight-Walker *et al.*, Proc. SPIE Int. Opt. Eng. **3153** (1997).

[44] M. Bergher, Nucl. Instr. Meth. Phys. Res. A **395**, 259 (1997).

[45] B. Podobedov, G. Carr, S. Kramer, and J. Murphy, Proc. PAC 2001 (2001), TPPH109.

[46] G. Carr *et al.*, NIM, Sec. A **463**, 387 (2001).

[47] A. Andersson, M. Johnson, and B. Nelander, Opt. Eng. **39**, 3099 (2000).

[48] M. Ako-Bakr, J. Feikes, K. Holldack, and G. Wüstefeld, Phys, Rev. Lett. **88**, 254801 (2002).

[49] A. Mochihashi, M. Hosaka, M. Katoh, M. Shimada, and S. Kimura, Proc. EPAC 06 (2006), THPLS042.

[50] J. Byrd *et al.*, Phys. Rev. Lett. **89**, 224801 (2002).

[51] ICFA Beam Dynamics Newsletter, No. 35, 2004.

[52] I. Martin, G. Rehm, C. Thomas, and R. Bartolini, Phys. Rev. ST Accel. Beams **14**, 040705 (2011).

[53] I. Martin *et al.*, Proc. PAC 09 (2009), THPE037.

[54] I. Martin *et al.*, Proc. IPAC 13 (2013), MOPEA070.

[55] M. Geitz, Proc. DIPAC 1999 (1999), IT07 (Invited Talk).

[56] J. Byrd, Ultrafast Instrumentation for Accelerators, Lecture at Joint US-CERN-Japan-Russia School on Particle Accelerators: Synchrotron Radiation and Free Electron Lasers, 2011.

[57] P. Emma, J. Frisch, and P. Krejcik, SLAC Technical Note: LCLS-TN-00-12 (2000).

[58] M. Rohrs *et al.*, Phys. Rev. ST Accel. Beam. **12** (2009).

[59] Y. Ding *et al.*, Proc. LINAC2014 (2014), THIOB03.

[60] Y. Okayasu *et al.*, Proc. DIPAC2011 (2011), TUPD68.

[61] H. Tomizawa, H. Hanaki, and T. Ishikawa, Proc. FEL 2007 (2007), WEPPH053.

[62] V. Ginzburg, Physica Scripta **T2/1**, 182 (1982).

[63] M. Castellano *et al.*, Phys. Rev E **63** (2001).

[64] M. Ako-Bakr *et al.*, Phys, Rev. Lett. **90** (2003).

[65] P. Karataev, Lecture entitled "Role of Electromagnetic Radiation in Charged Particle Bunch Length Diagnostics", DITANET Beam Diagnostics School, Royal Holloway, University of London, Egham, UK (2009).

[66] C. Settakorn, *Generation and Use of Coherent Transition Radiation from Short Electron Bunches*, PhD thesis, SLAC National Accelerator Laboratory, USA, 2001.

[67] J. Nodvick and D. Saxon, Physical Review **89** (1954).

[68] I. Gradshteyn and I. Ryzhik, *Table of integrals, series and products*, 7 ed. (Academic Press, 2007).

[69] G. Stupakov, Proc. PAC 03 (2003), TOAA002.

[70] M. Venturini *et al.*, Phys. Rev. ST Accel. Beams **8**, 014202 (2005).

[71] Y. Cai, Proc. IPAC 11 (2011), FRXAA01.

[72] M. Venturini and R. Warnock, Phys. Rev. Lett. **89** (2002).

[73] S. Heifets and G. Stupakov, Proc. PAC 2001 (2001), TPPH081.

[74] Y. Derbenev, J. Rossbach, and E. Saldin, TESLA FEL-Report **5** (1995).

[75] J. Murphy, S. Krinsky, and R. Gluckstern, Part. Accel. **57** (1995).

[76] M. Boas, *Mathematical Methods in the Physical Sciences* (World Scientific, 2005).

[77] R. Bartolini *et al.*, Proc. IPAC 11 (2011), THPC068.

[78] M. Sannibale *et al.*, Phys. Rev. Lett. **93**, 094801 (2004).

[79] K. Bane, S. Krinsky, and J. Murphy, Micro Bunches Workshop AIP Conference Proceedings 367 , 191 (1995).

[80] K. Bane, Y. Cai, and G. Stupakov, Phys. Rev. ST Accel. Beams **13**, 104402 (2010).

[81] G. Wüstefeld, J. Feikes, M. Hatrott, and M. Ries, Proc. IPAC 10 (2010), WEPEA015.

[82] Private Communication with Guenther Rehm (Diamond Light Source).

[83] L. Frohlich, Bunch length measurements using a martin-puplett interferometer at the vuv-fel, Master's thesis, Uni. Hamburg, 2005.

[84] R. Lai and A. Sievers, Phys. Rev. E **5**, 3342 (1994).

[85] R. Lai, U. Happek, and A. Sievers, Phys. Rev. E **5**, 4294 (1994).

[86] M. Micheler *et al.*, J. Phys. Conf. Ser. **236** (2010).

[87] O. Grimm and P. Schmuser, TESLA FEL 2006-03 (2006).

[88] K. Lekomtsev, *Investigation of Coherent Diffraction Radiation from a dual target system at CTF3 and its application for longitudinal bunch profile diagnostics*, PhD thesis, Royal Holloway, University of London, UK, 2012.

[89] M. Heron, Progress Report on the Diamond Light Source to the EPICS Meeting, DLS, June 03, Presentation, 2003, Diamond Light Source, Oxfordshire, UK.

[90] C. Thomas and G. Rehm, Proc. EPAC 06 , 1112 (2006), TUPCH047.

[91] M. Jensen *et al.*, Proc. EPAC 08 , 2037 (2006), WEPC025.

[92] H. Owen, J. Jones, and S. Smith, Proc. EPAC 02 , 751 (2002), TUPLE003.

[93] V. Suller, Proc. EPAC 02 , 757 (2002), TUPLE002.

[94] Private Communication with Ian Martin (Diamond Light Source).

[95] R. Bartolini, Accelerator Physics Studies for Generating Short Radiation Pulses at Diamond Light Source, Presentation, 2005, ICFA Mini-Workshop on Frontiers of Short Bunches in Storage Rings, INFN-LNF, Italy.

[96] C. Thomas and G. Rehm, Proc. DIPAC 05 , 93 (2005), POM026.

[97] C. Thomas and G. Rehm, Proc. EPAC 08 , 1254 (2008), TUPC086.

[98] M. Abbott, G. Rehm, and I. Uzun, Proc. ICALEPCS 2009 , 694 (2009), THP011.

[99] M. Jensen *et al.*, Proc. SRF2009 , 228 (2009), TUPPO019.

[100] C. Thomas *et al.*, Nucl. Instr. Meth. Phys. Res. A **566**, 762 (2006).

[101] C. Thomas, I. Martin, and G. Rehm, Proc. DIPAC 09 , 260 (2009), TUPB41.

[102] I. Martin *et al.*, Proc. IPAC 10 (2010), THPE037.

[103] Torr Scientific Ltd, Product catalogue, `http://torrscientific.co.uk/catalogue`, 2015.

[104] D. James and J. Ring, Journal De Physique Colloques **28**, 150 (1967).

[105] E. Palik, *Handbook of Optical Constants of Solids* (Academic Press, 1998).

[106] R. Kitamura, L. Pilon, and M. Jonasz, Applied Optics **46**, 8118 (2007).

[107] T. Parker, J. Ford, and W. Chambers, Infrared Physics **18**, 215 (1978).

[108] G. Zhao, M. Mors, T. Wenckebach, and P. Planken., J. Opt. Soc. Am B **19** (2002).

[109] LG Motion Ltd., Linear Dovetail Slide Assemblies, `http://www.lg-motion.co.uk/wp-content/uploads/2013/03/DovetailCatalogue-LGV.pdf`.

[110] Bosch Rexroth, Strut profiles, http://www.boschrexroth.com/en/xc/products/product-groups/assembly-technology/basic-mechanic-elements/strut-profiles/index.

[111] E. A. Chambers, ECCOSORB VHP-NRL, http://www.ecanechoicchambers.com/TB/EB-100-VHP-NRL.pdf, 2010.

[112] B.-K. Chung and H.-T. Chuah, Progress in Electromagnetics Research **43**, 273 (2003).

[113] E. Kuester and C. Holloway, IEEE Transactions on Electromagnetic Compatibility **34**, 300 (1994).

[114] P. Joseph, *A UTD Scattering Analysis of Pyramidal Absrober for Design of Compact Range Chambers*, PhD thesis, Ohio State University, USA, 1988.

[115] A. Khajehpour and S. Mirtaheri, Progress in Electromagnetics Research Letters **3**, 123 (2008).

[116] P. Dixon, Theory and Application of RF/Microwave Absorbers, http://www.ecnmag.com/sites/ecnmag.com/files/legacyfiles/ECN/Absorbers_White_Paper.pdf.

[117] A. R. V. Hippel, *Dielectric Material and Applications* (Artech House Publishers, 1995).

[118] A. Ray, A. Hibberd, J. Travis, and P. Kathirgamanathan, Material Letters **28**, 475 (1996).

[119] C. Homes, G. Carr, R. Lobo, J. LaVeigne, and D. Tanner, Applied Optics **46**, 7884 (2007).

[120] D. Smith and E. Loewenstein, Applied Optics **14**, 1335 (1975).

[121] C. Randall and R. Rawcliffe, Applied Optics **6**, 1889 (1967).

[122] Y. Jin, G. Kim, and S. Jeon, Journal of the Korean Physical Society **49**, 513 (2006).

[123] P. Cunningham *et al.*, Journal of Applied Physics **109** (2011).

[124] M. Micheler, *Development of Longitudinal Diagnostics for Electron Beams based in Coherent Diffraction Radiation*, PhD thesis, Royal Holloway, University of London, 2011.

[125] Newport Corp., UTS Series User Manual, `http://assets.newport.com/webDocuments-EN/images/UTS_User_Manual.pdf`.

[126] C. Corsi and F. Sizov, *THz and Security Applications* (Springer, 2013).

[127] Gentec EO, THZ-I-BNC THz Detector, `http://gentec-eo.com/Content/downloads/specifications-sheet/THZ-IIBNC_2012_V2.0.pdf`, 2012.

[128] P. Evtushenko *et al.*, AIP Conf. Proc. **868**, 193 (2006).

[129] A. Siegman, *Lasers* (University Science Books, 1986).

[130] G. Ponchak, Metal-Semiconductor Junctions, `http://parts.jpl.nasa.gov/mmic/3-II.PDF`, California Institute of Technology.

[131] A. Aryshev *et al.*, Nuc. Instrum. Meth. Phys. R. A **580** (2007).

[132] Virginia Diodes Inc., Detectors, `http://vadiodes.com/index.php/en/products/detectors`.

[133] A. Cowley and H. Sorensen, IEEE Transaction on Microwave Theory and Techniques **MTT-14** (1966).

[134] I. Martin, C. Thomas, and R. Bartolini, Proc. IPAC 12 (2012), TUPPP031.

[135] I. Virginia Diodes, Thz starter kits, `http://vadiodes.com/index.php/en/modular-amplifier-multiplier-chains`.

[136] R. H. Helm *et al.*, Proc. PAC 73 (1973).